Development of p-type transparent semiconducting oxides for thin film transistor applications

Thesis submitted to

COCHIN UNIVERSITY OF SCIENCE AND TECHNOLOGY

in partial fulfillment of the requirements

for the award of the degree of

DOCTOR OF PHILOSOPHY

Sanal K C

Department of Physics
Cochin University of Science and Technology
Cochin - 682 022, Kerala, India

January 2014

Development of p-type transparent semiconducting oxides for thin film transistor applications

Ph.D. thesis in the field of Materials Science

Author:
Sanal K C
Nanophotonic and Optoelectronic Devices Laboratory
Department of Physics
Cochin University of Science and Technology
Cochin - 682 022, Kerala, India.
Email: sanalcusat@gmail.com

Supervisor:
Dr. M. K. Jayaraj
Professor
Nanophotonic and Optoelectronic Devices Laboratory
Department of Physics
Cochin University of Science and Technology
Cochin - 682 022, Kerala, India.
Email: mkj@cusat.ac.in

Back cover: Schematic diagram of p-channel $Cu_{1-x}B_xO_{2-\delta}$ TFT

January 2014

.

Dedicated to my friends and family

Dr. M. K. Jayaraj
Professor
Department of Physics
Cochin University of Science and Technology
Cochin 682 022, India.

27^{th} January 2014

Certificate

Certified that the work presented in this thesis entitled "Development of p-type transparent semiconducting oxides for thin film transistor applications "is based on the authentic record of research carried out by Sanal K C under my guidance in the Department of Physics, Cochin University of Science and Technology, Cochin 682 022 and has not been included in any other thesis submitted for the award of any degree.

Dr. M. K. Jayaraj
(Supervising Guide)

Phone : +91 484 2577404 extn 33 Fax: 91 484 2577595 Email: mkj@cusat.ac.in

Dr. M. K. Jayaraj
Professor
Department of Physics
Cochin University of Science and Technology
Cochin 682 022, India.

27^{th} January 2014

Certificate

This is to certify that all the relevant corrections and modifications suggested by the audience during the Pre-Synopsis seminar and recommendations by the Doctoral committee of the candidate have been incorporated in the thesis entitled "Development of p-type transparent semiconducting oxides for thin film transistor applications "submitted by Sanal K C.

Dr. M. K. Jayaraj
(Supervising Guide)

Phone : +91 484 2577404 extn 33 Fax: 91 484 2577595 Email: mkj@cusat.ac.in

Declaration

I hereby declare that the work presented in this thesis entitled "Development of p-type transparent semiconducting oxides for thin film transistor applications"is based on the original research work carried out by me under the supervision and guidance of Dr. M. K. Jayaraj, Professor, Department of Physics, Cochin University of Science and Technology, Cochin-682 022 and has not been included in any other thesis submitted previously for the award of any degree.

Sanal K C

Cochin-22
27^{th} January 2014

Acknowledgements

I take this opportunity to place on record my profound sense of indebtedness and deep appreciation to my supervising guide, Prof. M. K. Jayaraj for his personal encouragement, patronly behaviour, stimulating discussions and able guidance right from the beginning to date as a consequence of which the present study reached fruition. My gratitude to him knows no bounds.

I express my sincere thanks to Prof. B. Pradeep, Head, Department of Physics and all the former Heads of the Department - Prof. Godfrey Louis and Prof. M. R. Anantharaman - for permitting me to use the research facilities in the Department. I gratefully acknowledge the help and inspiration from S. Jayalekshmi teacher who has inspired me in both academic and personal development. I would like to thank Prof. M. Sabir and Prof. V. C. Kuriakose for their suggestions and friendly discussions. I also greatly acknowledge the help and inspiration from all the faculty members of the Department of Physics.

I express my special gratitude to Prof. T. Ramesh Babu for his personal care and attention.

With pleasure, I acknowledge Prof. M. R. Prathapchandra Kurup, Director, IUCND for his encouragement and valuable suggestions throughout the research carrier.

I extend my sincere thanks to Prof. N. Chandra Mohana Kumar,

former Registrar, CUSAT, Prof. K Sreekumar, former Director of IUCND for their moral support and valuable discussions during the research period.

I am grateful to Prof. K. P. Vijayakumar and Deepu for XPS measurements.

I am thankful to all the office and library staff of the Department of Physics for the help and cooperation.

I thank Department of Science Technology (DST) and Inter University Center for Nanomaterials and Devices (IUCND) for financially supporting me during this endeavor. I acknowledge the financial support of SPIE to attend the international conferences during my research work.

It is my pleasure to acknowledge the advice and love received from my senior researchers in the Optoelectronic Devices Laboratory - Aldrin chettan, Manojettan, Nisha chechi, Rahana chechi, Asha chechi, Joshy sir, Mini chechi, Ajimshettan, Anoopettan, Anila teacher and Vanaja Madam. I express my special gratitude to Sajiettan for the utmost love and care in the entire academic life at CUSAT. I greatly acknowledge the helping hands provided by - Aneesh, Reshmi chehci, in every patches of the research life. Its immense joy to work with - Satish bhai, Krishnaprasad, James Sir, Sasankan, Sreeja, Vikas, Hasna, Subha, Majeesh, Saritha chechi, Shijeesh, Vishnu, Anjana. I wish to express my sincere regards to Anooja and Anjala for the beautiful time in the lab.

I am especially grateful to my dear friends - Priyesh, Arun, Nijo

Varghese, Rajesh Mon, Subin Thomas and Tharanath for their patience, encouragement and moral support at each and every stage of my life.

I really enjoyed the wonderful company, support and constant encouragement of my friends - Bhavya and Rajesh C. S.

I value my friendship with Anlin Nazar, Vasudevan, Anshad, Sujit, Priyanka, Rameeja, Gokul, Kurias, Sruthi and Jijin whom I got acquainted with at OED.

I would like to thank all my colleagues at the department of Physics especially Sajan, Manoj, Tittu, Jubeesh, Sreejith, Santhosh, Vipin, Poornima, Navaneeth, Sudeep, Rijeesh, Vinod, Jishnu, Dinto MOn, Anand, Aravind, Hyson chettan, Sajeesh, Geetha, Krishna Sagar, Satheesh, Abhilash and all other friends in CUSAT for their great moral and financial support during my academic period. I express my sincere thanks to all my school mates and B.Sc friends .

Its my proud privilege to remember my family for their selfless support, motivation, encouragement, patience and tolerance throughout.

My time at CUSAT was made enjoyable in large part by the many comrades who have become a part of my life. I thank all the comrades for giving me a dynamic and unforgettable social life in CUSAT

Sanal. K. C

Contents

Preface

Thin film transistor (TFT) is a combination of thin films necessary to create the function of a transistor. It consists of a thin film of a semiconducting material which forms the conducting channel between metallic source and drain electrodes. There is a dielectric layer between the semiconducting material and gate electrode. The most important application of TFT is in liquid crystal displays (LCD) wherein TFTs are integrated to each of the sub pixels to modulate the amount of light reaching observers eyes. In addition to this, TFTs are widely used in medical imaging equipments, organic light emitting diode displays, flat panel displays, field emission displays, imagers, scanners and various types of sensors etc.

Presently, all these applications make use of n channel oxide TFTs. The enormous success of n type oxide semiconductors and its applications in the field of TFTs motivated the interest in p-type semiconductor-based TFTs. But still there is no report on p-type oxide TFTs with performance similar to that of n-type oxide TFTs. p-Type TFTs are generally limited by the low hole mobilities since the mobility of valance band derived carriers generally lower than the conduc-

tion band derived electrons. Achieving high performance p-type oxide TFTs will definitely promote a new era for electronics in rigid and flexible substrate away from silicon. Moreover it will shape the electronics of tomorrow by allowing the production of complementary metal oxide semiconductors, a key device to fuel the microelectronics revolution in the so called technologies of information and communication.

Scientists had been looking p-type material for the application of TFTs. The simple binary oxides like SnO have also been explored as a promising p-type semiconductor for TFT fabrication. In the present study a systematic synthesis of tin oxide thin films using RF magnetron sputtering was carried out. and of Recently much attention has been given to Cu based semiconductors (Cu_2O, $CuAlO_2$, $CuCrO_2$, $CuBO_2$ etc.). Recently, a few group reported p-type oxide semiconductor based TFTs using the CuO and Cu_2O as active channel materials. The maximum mobility obtained for Cu_2O channel TFT fabricated using high temperature PLD technique was 4.3 cm^2 V^{-1} s^{-1}. Sung et al fabricated TFT on p-type silicon substrate using post annealed CuO channel layer with field effect mobility 0.4 cm^2 V^{-1} s^{-1} and on off ratio 1.1 x 10^4. In the present study we have tried room temperature deposited CuO and Cu_2O channel layer for the fabrication of TFTs. Co-sputtering is an effective technique for a multicomponent film to control the film chemical composition in a systematic and easy way. We have used co sputtering technique to develop p type copper boron oxide and copper chromium oxide thin films. The optoelectronic properties of amorphous and transparent $Cu_{1-x}B_xO_{2-\delta}$ and $Cu_{1-x}Cr_xO_{2-\delta}$ films examined as a function of the chemical composition. The room temperature deposited copper chromium oxide channel layer was also employed for the fabrication TFTs.

Chapter 1 presents a brief description about the fundamentals of amorphous semiconductors, challenges in p-type oxide semiconductors and a brief review of oxide thin film transistors. The optical absorption and electronic transport in amorphous materials are discussed. This chapter also provide the basic working hypothesis of transparent amorphous oxide semiconductors and their electronic structure. The literature review on thin film transistors using transparent oxide semiconductor material channel is given in the last part of this chapter.

Chapter 2 describes in detail the thin film growth techniques and characterization tools employed in the present work. Thin film growth was accomplished using pulsed laser deposition (PLD) and co-sputtering techniques. In this chapter a brief description of the basic mechanism of RF magnetron sputtering is given. Thickness of the films was measured using stylus profilometer. Structural characterization was performed by glancing angle x-ray diffraction method and atomic force microscopy (AFM). Compositional analysis was carried out by x-ray photo electron spectroscopy (XPS). Band gap of the grown thin films were estimated by optical transmittance studies using a UV-Vis-NIR spectrophotometer. The electrical characterisation of the films were carried out at room temperature by a Hall effect measurement system. The basic operation and specifications of all these characterisation tools are described in this chapter. A detailed description about TFTs is given towards the end of this chapter. This section includes thin film transistor structures, the basic device operation, modes of operation, dielectrics, amorphous oxide channels, TFT characterisation etc.

Chapter 3 deals with the room temperature deposition and characterization of tin oxide thin films using RF magnetron sputtering. p-

Type and n-type tin oxide thin films were deposited by RF magnetron sputtering at different oxygen partial pressure. Structural, optical and electrical properties of these films were studied as a function of oxygen partial pressure and annealing temperature. Amorphous structure of as deposited SnO_x films and polycrystalline tetragonal structure of annealed SnO films were confirmed by GXRD. Surface morphology of synthesized samples was characterised by atomic force microscopy. Atomic percentage of the SnO thin film according to the intensity of the XPS peak was about 48.85% and 51.15% for tin and oxygen respectively. Band gap of as deposited SnO_x thin films was varying from 1.6 eV to 3.2 eV as the oxygen partial pressure varies from 3-30% which indicates the oxidization of metallic phase tin to SnO and SnO_2. Type of the charge carrier and conductivity of the tin oxide thin films were varied with oxygen partial pressure. Transparent pn hetero junction fabricated in the structure glass/ITO/n-ZnO/p-SnO show rectifying behaviour.

Chapter 4 describes the deposition of copper oxide thin films using RF magnetron sputtering. This chapter is divided in to three sections viz., the systematic synthesis of copper oxide thin films using Rf magnetron sputtering by varying oxygen partial pressure to grow thin films with pure Cu_2O and CuO phase at room temperature, fabrication of transparent flexible pn hetero junction in the structure PET/ITO/n-ZnO/p-CuO/Au, fabrication of room temperature deposited transparent p-type CuO and Cu_2O thin film transistors. p-Type copper oxide thin films were deposited by RF magnetron sputtering at different oxygen partial pressure. Structural, optical and electrical properties of these films were studied as a function of oxygen partial pressure. Transparent flexible pn hetero junction fabricated in the structure

PET/ITO/n-ZnO/p-CuO show rectifying behaviour. Transparent p-type TFTs with CuO channel layer were fabricated at room temperature. The bottom gate structured p-channel CuO TFTs exhibited an on-off ratio of 10^4 and the field-effect mobility of 0.01 cm^2 V^{-1} s^{-1}. Cu_2O layer was also employed for the fabrication of TFT in which field effect mobility obtained was 1.34 cm^2 V^{-1} s^{-1} and on-off ratio 10^4.

Chapter 6 is divided into two sections. First section deals with the growth and characterisation of stable p-type copper boron oxide thin films at room temperature by RF magnetron co-sputtering and the fabrication of a pn hetero junction using p-type $Cu_{1-x}B_xO_{2-\delta}$ and n-type silicon. The second section deals with the development of p-type $Cu_{1-x}Cr_xO_{2-\delta}$ thin films at room temperature by RF magnetron sputtering and fabrication of TFTs using $Cu_{1-x}Cr_xO_{2-\delta}$ as a channel layer. Transparent p-type amorphous $Cu_{1-x}B_xO_{2-\delta}$ thin films were grown on the glass substrate by RF magnetron co- sputtering of copper and boron at room temperature in an oxygen atmosphere. Structural, optical and electrical properties of these films were studied as a function of boron content in the film. Amorphous structure of as deposited films was confirmed by GXRD. Compositional analysis was carried out by XPS measurement and surface morphology of synthesized samples was characterised by atomic force microscopy. Band gap of as deposited $Cu_{1-x}B_xO_{2-\delta}$ thin films varies from 1.8 eV to 3.2 eV as boron content increases in the film. Positive Hall coefficient obtained for all the film confirms the p-type conductivity in $Cu_{1-x}B_xO_{2-\delta}$. pn Hetero junction fabricated in the structure n-Si/p-$Cu_{1-x}B_xO_{2-\delta}$/Au show rectifying behaviour. Transparent p-type amorphous $Cu_{1-x}Cr_xO_{2-\delta}$ thin films were grown on the glass substrate by RF magnetron co-sputtering

at room temperature. Structural, optical and electrical properties of these films were studied as a function of chromium content in the film. Amorphous structure of as deposited films was confirmed by GXRD. Compositional analysis was carried out by XPS measurement and surface morphology of synthesized samples was characterised by atomic force microscopy. Positive Hall coefficient obtained for all the film confirms the p-type conductivity in $Cu_{1-x}Cr_xO_{2-\delta}$. The Bottom gate structured TFTs fabricated using p-type $Cu_{1-x}Cr_xO_{2-\delta}$ operated in enhancement mode with an on-off ratio of 10^4 and field effect mobility 0.3 cm^2 V^{-1} s^{-1}.

Chapter 6 summarizes the major contributions of the present investigations and recommends the scope for future works.

Part of the work presented in the thesis has been published in various journals

Journal papers

1. Growth and characterisation of tin oxide thin films and fabrication of transparent p-SnO/n-ZnO pn hetero junction **K. C. Sanal**, M. K. Jayaraj Material Science and Engineering B 13352 (2013) 16.

2. Room temperature deposited transparent p-channel CuO thin film transistors **K. C. Sanal**, and M. K. Jayaraj, Journal of Applied Surface Science (Accepted, 2014).

3. Development of p-type amorphous $Cu_{1-x}B_xO_{2-\delta}$ thin films and fabrication of pn hetero junction **K. C. Sanal**, and M. K. Jayaraj

(under review-Mater. Sci. Eng. B).

4. Fabrication of room temperature deposited p-channel copper oxide thin film transistors **K. C. Sanal**, M. K. Jayaraj (under review- Royal Soci. Chem).

5. Development of p-Type Amorphous $Cu_{1-x}Cr_xO_{2-\delta}$ thin films and fabrication of thin film transistors, **K. C. Sanal**, and M. K. Jayaraj (under review-Royal Soci. Chem).

Conference papers

1. Growth and characterisation of p-type amorphous $CuCrO_x$ thin films by RF mangetron co-sputtering, **K. C. Sanal** and M. K. Jayaraj, National seminar on emerging trends in growth and characterization of single crystals and nanomaterials, 2013 march, SH college chalakudy.

2. Growth of p-type Amorphous Transparent Oxide Thin Films by Co-sputtering. **K. C. Sanal** and M. K Jayaraj, ICMATT-2013, Singapore.

3. Growth of transparent conducting copper boron oxide thin films and fabrication of pn hetero junction. **K. C. Sanal** and M. K. Jayaraj, National conference on Nanotechnology and Renewable energy (NSNRE-2013) October, K. E college, Mannanam, Kottayam.

4. Room temperature deposited copper chromium oxide thin film transistors, **K. C. Sanal** and M. K. Jayaraj, National conference on nanotechnology and renewable energy (NSNRE-2013) October, K. E college, Mannanam, Kottayam.

5. Growth of copper chrmium oxide thin films and fabrication of thin film transistors **K. C. Sanal** and M.K.Jayaraj, IUMRS, ICA 2013, Dec 16-20.

Other publication to which author has contributed

Journal papers

1. Growth of silver nanoparticles in SiO_2 matrix by co-sputtering technique, **K. C. Sanal**, R. Sreeja, K.Anlin Lazar and M.K.Jayaraj, Nanophotonicmaterials, Proc. of SPIE 7393 (2009) 73930J-1.

2. Growth of ITO thin films on polyimide substrate by bias sputtering M. Nisha, K. A. Vanaja, **K.C. Sanal**, K. J. Saji, P. M. Aneesh and M. K. Jayaraj, Materials Science in Semiconductor Processing 13 (2010) 6469.

3. Growth of IGZO thin films and fabrication of transparent thin film transistors by RF magnetron sputtering. **K. C. Sanal**, Majeesh and M. K. Jayaraj, Proc. SPIE 8818, Nanostructured Thin Films VI, 881814 (2013).

Conference papers

1. Growth of silver nanoparticles in SiO_2 matrix by co-sputtering technique, **K. C. Sanal**, R. Sreeja, K. Anlin Lazar and M. K. Jayaraj, SPIE Optics and Photonics 2009, San Diego, USA.

2. Electrical Conductivity Measurement of a Single ZnO Nanorod, L. S. Vikas, M. K. Jayaraj, P. P. Subha, J. Puigdollers, T. Trifonov, S. Galindo, C. Voz, Aldrin Antony, **K. C. sanal**, ICMATT 2013, Singapore.

Chapter 1

Introduction

1.1 Introduction to transparent conducting oxides

Semiconductor physics has developed significantly in the field of research and industry in the past few decades due to it's numerous practical applications. One of the relevant fields of current interest in material science is the fundamental aspects and applications of semiconducting transparent thin films. Transparent conductors show the properties of transparency and conductivity simultaneously. As far as the band structure is concerned, the combination of the these two properties in the same material is contradictory. Generally a transparent material is an insulator having completely filled valence and empty conduction bands. Metallic conductivity come out when the Fermi level lies within a band with a large density of states to provide high carrier concentration. Effective transparent conductors must necessarily represent a compromise between a better transmission within

the visible spectral range and a controlled but useful electrical conductivity [1–6]. Generally oxides like In_2O_3, SnO_2, ZnO, CdO etc, show such a combination. These materials without any doping are insulators with optical band gap of about 3 eV. To become a transparent conductor, these materials must be degenerately doped to lift the Fermi level up into the conduction band. Degenerate doping provides high mobility of extra carriers and low optical absorption. The increase in conductivity involves an increase in either carrier concentration or mobility. Increase in carrier concentration will enhance the absorption in the visible region while increase in mobility has no reverse effect on optical properties. Therefore the focus of research for new transparent conducting oxide (TCO) materials is on developing materials with higher carrier mobilities.

1.2 General properties of transparent conducting oxides

1.2.1 Transparency and conductivity

Optical transparency and electrical conductivity are antonyms to each other which can be easily proved using the Maxwell's equations of electromagnetic theory as described below [7]. For electromagnetic (em) waves moving through an uncharged semiconducting medium, the solution to Maxwell's equation gives the real and imaginary parts of the refractive index as

$$n^2 = \frac{\epsilon}{2}[(1 + [\frac{2\sigma}{\nu}]^2)^{\frac{1}{2}} + 1] \tag{1.1}$$

$$k^2 = \frac{\epsilon}{2}[(1 + [\frac{2\sigma}{\nu}]^2)^{\frac{1}{2}} - 1] \tag{1.2}$$

where n is the refractive index of the medium, k is the extinction coefficient, ϵ is the dielectric constant, σ is the conductivity of the medium and ν is the frequency of the electromagnetic radiation. For an insulator, where $\sigma \to 0$ then n $\to \epsilon^{\frac{1}{2}}$ and k $\to 0$. This indicates that an insulator is transparent to electromagnetic waves. For a perfect conductor, the solution of the Maxwell's equation for the reflected and transmitted component of the electric field vector are E_R = - E_I and $E_T = 0$. Hence the wave totally gets back with 180^o phase difference. In other words, a good conductor doesn't transmit the radiations incident on it, while a good insulator is transparent to the electromagnetic radiations.

Drude's theory for free electrons in metals can explain the optical absorption of transparent conducting oxides in the IR range [8–10]. The interaction of free electrons with an em field, may lead to polarization of the field within the material, which affects the relative permittivity ϵ. Equation for the motion of an electron in an electric field, can be written as,

$$m[\frac{d}{dt} + \frac{1}{\tau}]\delta v(t) = F \tag{1.3}$$

where τ is the relaxation time.

The force on an electron in an alternating field is given by

$$F = -eEe^{-i\omega t} \tag{1.4}$$

Let us assume a solution to equation 1.4 in the form δv = δ ve$^{-i\omega t}$ Then equation 1.3 becomes,

$$m[i\omega + \frac{1}{\tau}]\delta v = -eE \tag{1.5}$$

$$\delta v = -\frac{\frac{e\tau}{m}}{1 - i\omega\tau} \tag{1.6}$$

the current density is

$$j = nq\delta v = \frac{ne^2\tau}{m(1 - i\omega\tau)}E \tag{1.7}$$

where n is the electron concentration and q is the charge on the electron.

The electrical conductivity is

$$\sigma(\omega) = \frac{ne^2\tau}{m(1 - i\omega\tau)} = \sigma_0\frac{(1 + i\omega\tau)}{1 + (\omega\tau)^2} \tag{1.8}$$

Here, $\sigma_0 = \mathrm{ne}^2\tau/\ \mathrm{m}$ is the dc conductivity. At high frequencies, $\omega\tau \gg 1$, we can write

$$\sigma(\omega) = \sigma_0[\frac{1}{(\omega\tau)^2 + \frac{i}{\omega\tau}}] = \frac{ne^2}{m\omega^2\tau} + i\frac{ne^2}{m\omega} \tag{1.9}$$

The imaginary term is dominant in the above equation and is independent of τ. Thus we can express the result as a complex dielectric constant rather expressing it as a complex conductivity.

The dielectric constant

$$\epsilon = (1 + 4\pi p/E) \tag{1.10}$$

where

$$P = \frac{ne^2/m}{\omega^2 + i\frac{\omega}{\tau}} \tag{1.11}$$

Then

$$\epsilon(\omega) = \frac{1 - 4\pi n \frac{e^2}{m}}{\omega^2 + i\frac{\omega}{\tau}} \tag{1.12}$$

ϵ (ω) is the dielectric constant of a free electron gas

For $\tau \to \propto$ the dielectric constant is positive and real if $\omega^2 > 4\pi$ ne^2/m. Electromagnetic wave cannot pass through a medium with negative dielectric constant because then wave vector is imaginary and the wave decays exponentially. Waves hit on such a medium get totally reflected. We can denote the cut off frequency as

$$\omega_p = (4\pi e^2/m)^{\frac{1}{2}} \tag{1.13}$$

which is known as the plasma frequency. The material is transparent to the em radiation with a frequency greater than the plasma frequency. The optical properties of a transparent conducting film have strong dependence on deposition parameters, micro structure and impurity levels. TCOs are transparent in the visible and NIR range and they reflect IR radiations, hence it can act as a selective transmitting layer. The transmission spectrum of a TCO is shown in figure 1.1, λ_{gap} is the corresponding wavelength of the band gap and λ_p is the plasma wavelength.

The transmission spectrum (figure 1.1) shows that for wavelength greater than plasma wavelength λ_p the TCO reflects radiation and for shorter wavelengths up to λ_{gap} TCO is transparent. At frequencies higher than the plasma frequency, the electrons cannot respond to the varying electric field of the incident radiation, and the material act as a transparent dielectric. Most of the TCOs possess plasma frequency in near- infrared region of the electromagnetic spectrum, thereby making

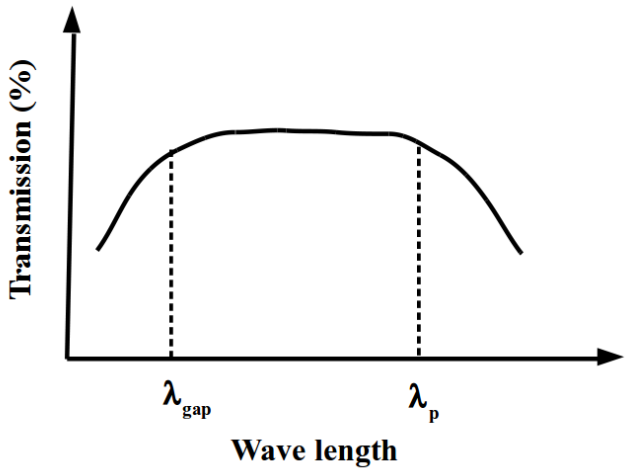

Figure 1.1: Transmission spectrum of TCO

them highly transparent in the visible region. The plasma frequency is linearly proportional to the square root of the conduction-electron concentration. The maximum attainable electron concentration and the plasma frequency of TCOs usually varies as same as the resistivity [11].

1.2.2 Electronic properties

Conventional TCOs (In_2O_3, SnO_2, CdO, ZnO etc) have similar chemical, structural and electronic properties. Oxides of the post-transition metals with $(n\text{-}1)d^{10}ns^2$ electronic configurations have densely packed structures. Strong interactions between the oxygen 2p and metal ns orbitals leads to electronic band structures. The valence band is formed by bonding and nonbonding O 2p states and the conduction band is formed from the anti-bonding metal s orbital- oxygen p orbital (Ms-

Op) interactions. Ms-Op interactions generate a gap between the valence and the conduction bands. The Ms-Op overlap causes the energy dispersion of the conduction band in these materials. The largest Ms-Op overlap is obtained when the oxygen atom have octahedral coordination by cations. Accordingly, the octahedral coordination of the oxygen atoms in rocksalt CdO causes the largest dispersion and smallest electron effective mass among the TCO materials [12]. The optical and transport properties of a conventional TCO are controlled by the carrier generation mechanism adopted. Substitutional doping with aliovalent ions is the general approach for free carrier generation in TCOs because it has better control over the resulting optical and transport properties as well as better environmental stability of the TCO films. Conventionally, same-period, next-row elements (Sn^{4+} for In^{3+} and In^{3+} for Cd^{2+}) are expected to furnish better compatibility and less disturbance in the host crystal and electronic structure. Transparent conducting ZnO can be prepared by doping with Group III (Al, Ga, In and B) Group IV (Si, Ge, Ti, Zr and Hf) and a Group VII element (F substituted at an oxygen site), leading tunable electrical conductivities over wide range [13].

Removal of an oxygen atom from a metal oxide can provide additional electrons in the crystal. These electrons become free carriers or remain localized at the vacancy site depending on free energy of formation of the oxide. In metal oxides like CaO or Al_2O_3 the formation energy is high and hence oxygen vacancies generate deep charge localized states within the electronic band gap which is known as color or F centers. A relatively low formation energy of the conventional TCOs cause higher free-carrier densities [14–17].

1.2.3 Optical and electrical performance

TCOs have two significant properties viz, optical transmission and electrical conductivity, and these two parameters are somewhat inversely related, and a method is required for comparing these properties. Generally researchers use "figure of merit "to compare the optical and electronic properties of a TCO. Researchers have developed different techniques to determine the figures of merit of the films. One of the earliest equations defining a figure of merit was developed by Fraser and Cook [18] is given by

$$F_{FC} = \frac{T}{R_s} \tag{1.14}$$

where T is the transmission and Rs is the sheet resistance of the thin film. This value was often multiplied by 1000 to allow comparisons of numbers greater than one. This definition have a dependence on the film thickness.

Haacke [19] made another defnition for figure of merit (F_H) which is also related to the above definition. F_H put more focus on the optical transparency because F_{FC} was too much in favor of sheet resistance, resulting in a maximum figure of merit at relatively large film thicknesses. The figure of merit was redefined as

$$F_H = \frac{T^x}{R_s} \tag{1.15}$$

where x > 1. Haacke selected the value of x = 10. The definition by Haacke is also thickness dependent. The third definition for figure of merit was proposed by Iles and Soclof [20]. A figure of merit that dont have film thickness dependence is given by.

$$F_{IS} = Rs[1 - T] = \frac{\alpha}{\sigma} \tag{1.16}$$

By this definition, a lower value of figure of merit indicates films of better quality. Most of the variation in the figure of merit of TCO is due to mobility variation, but the free electron concentration does not impact the figure of merit. The electron mobility is determined by the electron-scattering mechanisms that operate in the material. Generally some scattering mechanisms, such as scattering of electrons by phonons are exhibit in pure single crystals. Practical TCOs require much better doping levels and for these high doping levels, scattering by the ionised dopant atoms become another important mechanism that can limit the mobility. This maximum mobility is lowered still further by other scattering mechanisms such as grain-boundary scattering, present in polycrystalline thin films.

1.3 Amorphous semiconductors

1.3.1 Structure of amorphous materials

Amorphous materials have attracted much attention in the last three decades because of their potential industrial applications as suitable materials for fabricating devices, and the second reason is the lack of information about properties of these materials. Some of their properties even vary from sample to sample of the same material. An ideal crystal is defined as an atomic arrangement that has infinite translational symmetry in all direction, whereas such a definite definition is not possible for an ideal amorphous solid (a-solid).

Although an amorphous solid is generally defined as one that does not maintain long-range translational symmetry or has only short-range order. A real crystal does not have infinitely long translational

symmetry, because of its finite size (surface atoms), but that does not make it amorphous. In addition to surface atoms, amorphous materials shows structural disorders due to dissimilar bond lengths, bond angles and coordination numbers at individual atomic sites. But there are many properties of amorphous materials, which are similar to those of crystalline solids (c-solids).

Amorphous semiconductors and insulators are used for fabricating many opto-electronic devices. Amorphous silicon and its alloys are the most widely employed amorphous semiconductors for fabricating thin film solar cells, thin film transistors and other opto-electronic devices. Although one of the amorphous forms of solid is glass which is intensively known and used by human beings from the early stage.

The theory of amorphous systems is relatively hard, because some of the techniques of simplification applicable in crystals cannot be applied to amorphous structures.

It is commonly accepted that amorphous solids have mainly three types of structural disorders, which do not exist in crystalline solids. These are (1) different bond lengths (2) different bond angles and (3) under- and over-coordinated sites, In amorphous or crystalline silicon, each Si atom has four valence electrons to make the covalent bonding with the neighboring Si atoms. Thus each Si atom forms four covalent bonds with its neighbors, so the coordination number in crystalline Si is 4 at every site. In amorphous (a-Si) it is not essential that all atomic sites have the same coordination number 4. Some times one or more covalent electrons on a Si atom cannot form covalent bonds with the neighboring atoms and such uncoordinated bonds are called dangling bonds. In addition to dangling bonds, a-Si network also has many weak and strained bonds, which are generally longer than a

fully coordinated Si-Si bond. In order to lower the density of dangling bonds in a-Si, the technique used is to hydrogenate it to produce hydrogenated amorphous silicon (a-Si:H). The existence of strained and weak bonds gives rise in a-Si:H to band tail states, which are also found in other amorphous semiconductors and insulators [21].

A crystalline semiconductor has well-defined shrarp valence and conduction band edges, and hence a very well defined electron energy bandgap in between them as shown in figure 1.2(a). In amorphous semiconductors, the neutral dangling bond states lie in the midway of the energy band gap, and bonding and anti-bonding orbital of weak bonds lie above the valence band and beneath the conduction band edges respectively, as shown in the figure 1.2(b).

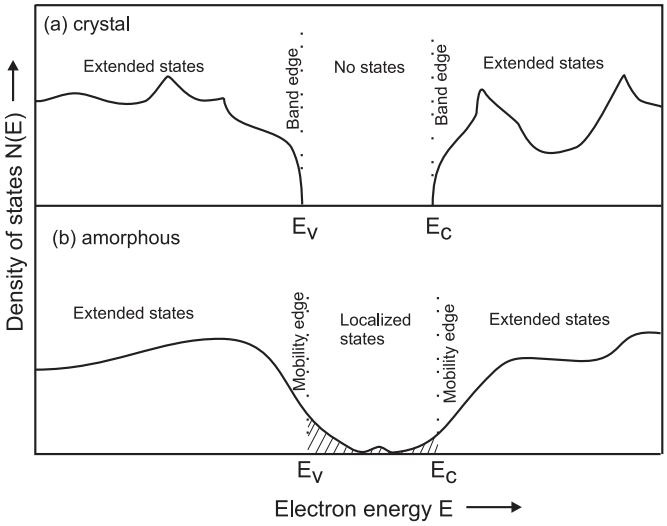

Figure 1.2: Schematic diagram of density of states for (a) crystalline and (b) amorphous semiconductors

In addition to the neutral dangling bond states, there is chance for

charged dangling bond states. If the charge carrier-phonon interaction is very strong in an amorphous solid then the positive charged dangling bond states (D_+) would lie above the neutral dangling bond state, but just below the conduction band edge. The negative charged dangling bond states (D_-) would lie below the neutral dangling bond state, but above the valence band edge [22].

In the case of weak charge carrier-phonon interaction, the positions of D+ and D- get interchanged on the energy scale. The band tail states lie above the valence and below the conduction band edges, these states are generally the highest occupied and lowest empty energy states in any amorphous semiconductor. Hence, band tail states got important role in most optical and electronic properties of amorphous semiconductors.

1.3.2 Band models

In amorphous semiconductors the band structure and electrical properties are determined by the long range disorder in their structure. Several models proposed for the energy distribution or the density of states is mainly focused on the question of the existence of localized states in the tails of valence band and conduction band and of a mobility edge distinguishing the extended states from the localized states. In the amorphous state if the short rang order is same as that of crystalline semiconductors, some basic features of the electronic structure as that of crystalline solids will be retained.

Modifications for band structure of amorphous solids have been suggested to incoperate the transnational disorder along with compositional disorder in multicomponent systems. Cohen-Fritzsche-Ovshinsky

(CFO) and Davis -Mott models are well known models in which they introduced the basic idea of the presence of localized states in the band extremities. Experimental results in electrical properties and optical properties are analysed by these band models.
A model for electronic structure is necessary for the correct evaluation of experimental results regarding the electrical and optical properties. Crystalline semiconductors have sharp structure for energy distribution of density of electronic states at valence band and conduction band. This sharp and abrupt termination in the distribution of density of states at valance and conduction band edge form a well defined forbidden energy gap. Particular features of the band structure are the result of the perfect short range and long range order of the crystal. Such a long range is absent in an amorphous solid, but the short range order is only some what modified. The concept of density of states also can be applied to non-crystalline solids. According to Mott, the spatial variation in the potential caused by configurational disorder in amorphous materials may result in the localized states, which do not reside all the different energies in the band, but produce a tail above and below the normal band. Mott also suggested that there should be sharp boundary between the energy ranges of extended and localized states. These states are treated as localized because at zero temperature an electron occupied in a region will not move to other regions with corresponding potential variation. Using the concept of localized states in the band tails, different models have been suggested for the electronic band structure of amorphous semiconductors.

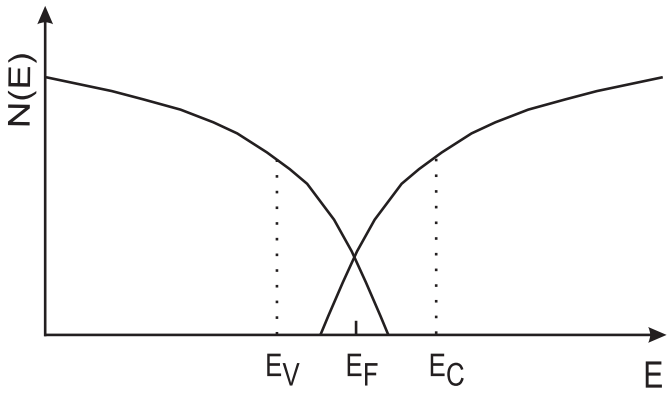

Figure 1.3: Schematic representation of DOS in CFO model. Symbols: E_V is valence band energy edge corresponding to crystalline case, E_C is conduction band energy edge corresponding to crystalline case and E_F is the Fermi energy

Cohen-Fritzsche-Ovshinsky (CFO) model

Figure 1.3 shows the energy states as explained by CFO model [24]. According to CFO model compositional and topological disorders cause extensive tailing of band edges. CFO model was particularly suggested for the multi component Chalcogenide glasses. Chalcogenide alloys have sufficiently great disorder so that the tails of conduction and valence band overlap, resulting in a considerable density of states in the mid-gap. Hence the filled states in the valence band have higher energies than the conduction band that are generally unfilled. A redistribution of charges takes place, making negatively charged filled states in the conduction band and positively charged empty states in the valence band which ensures self compensation and pinning of the Fermi level close to the mid gap [25, 26]. Major objection pointed against the CFO model has been the high transparency of amorphous chalcogenides below a well defined absorption edge which makes a con-

clusion that, the extent of tailing is only a few tenths of an electron volt in the gap. Another objection about this model is that it suggest the elemental semiconductors like a-Si, a-Ge, a-As etc, should not have the extensive band tailing as they are free from compositional disorder [27].

Davis and Mott (DM) model

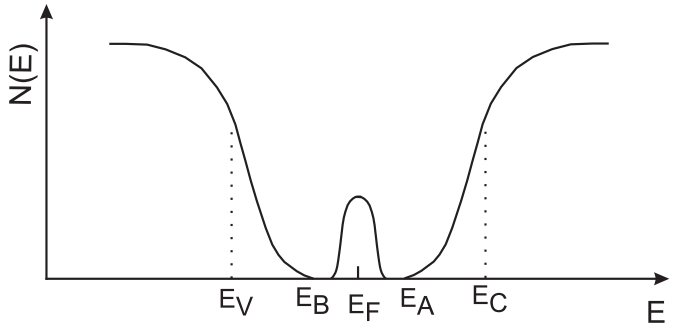

Figure 1.4: Schematic representation of DOS in Davis-Mott model. Symbols: E_V is valence band energy edge corresponding to crystalline case, E_C is conduction band energy edge corresponding to crystalline case, E_B and E_A are valence band and conduction band tailing edge and E_F is the Fermi energy

Figure 1.4 shows the band model suggested by Devis and Mott. The mobility edges for electrons and holes lie at Ec and Ev. DM model [27–29] suggest that the tails of localized states should be very narrow and should cover a few tenths of an electron volt into the forbidden gap. i.e. to E_A and E_B. The tails of localized states are originated from the absence of long-range order.

The centre of the band may be divided into a donor and an acceptor bands, which will also pin the Fermi level (figure 1.5). Transition from extended to localized states appreciably lower the mobility form-

ing a mobility edge. The mobility gap is the pseudo gap between the energies E_c and E_A. The model describes three processes related to the electrical conduction in amorphous semiconductors. At very low temperature the reason for electrical conduction is the thermally aided tunnelling between the states at the Fermi level. At higher temperature hopping is the reason for carrier transport which will be discussed in the section 1.3.4. The mobility in the localized state is rather lower than that of extended state . Hence temperature dependent conductivity measurement is necessary to analyse the electronic structure of amorphous semiconductors.

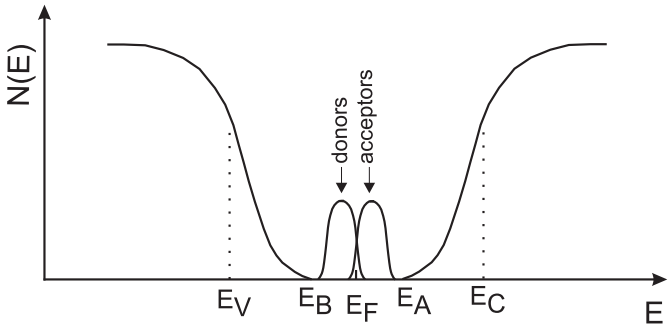

Figure 1.5: DOS in modified Davis-Mott model. Symbols: E_V is valence band energy edge corresponding to crystalline case, E_C is conduction band energy edge corresponding to crystalline case, E_B and E_A are valence band and conduction band tailing edge and E_F is the Fermi energy

1.3.3 Carrier transport

The transport of charge carriers in amorphous semiconductors becomes quite perplex due to the presence of tail states. According Mott and Davis [23] the delocalized extended and localized tail states

cannot coexist in amorphous solids. A charge carrier generated in the extended states can move freely, but in the tail states its motion will be confined. The height of the electron mobility edge in amorphous solids can be considered as a potential barrier for carriers that exists between different sites. Electron having energy higher than the barrier height, its motion remains wave like and if the electron energy is less than that of the barrier height, the electron wave function decays exponentially in the barrier region. The same idea can also be applied for the movement of the holes in the valence states. At very low temperatures, there is a chance to excite an electron by optical excitation from states near the hole mobility edge at the top of the valence extended states. Thus the hole will be generated near its mobility edge, but the state of the electron will depend on the energy of the exciting photon. Excited electron in the conduction states shall be considered first, similar results can be derived for holes. Only the nearest neighbor interaction for an excited electron-hole pair is taken in to account and assume that the electron mobility edge is at an energy E_c above the hole mobility edge. Assume that the electron is excited with energy E, and meanwhile it is interacting with the excited hole. Electron is bound to cross a barrier of height E_c before it can move to another site (Figure 1.6). Figure shows three regions. In region 1, the electron have an interaction with the excited hole only. In region 2, electron is influenced by of both Coulomb potential and the barrier potential E_c, and in region 3, it has moved to an energy state of another site but it is still influenced by Coulomb potential due to the same hole. If the energy E is less than E_c the electronic eigenfunction decreases exponentially within the barrier. Then an excited electron moves from one tail state to another Which is called as non radiative tunneling.

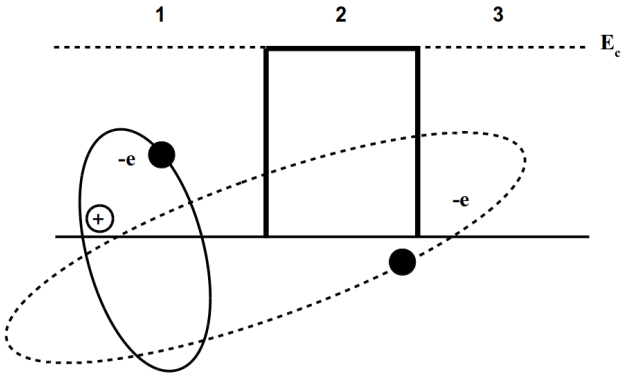

Figure 1.6: Schematic illustration of excitation of an e-h pair under the influence of Coulomb interaction in amorphous solids

The nature of the transport of charge carriers gets changed when a charge carrier move across the mobility edges E_C and E_V. The transport above E_C is the band conduction type for electrons and transport below E_V is band conduction type for holes. If the carrier is transported through localized states, it is known as the hopping conduction. The electronic transport at room temperature and above in amorphous solid is considered to occur in the extended states. An activation-type temperature dependence of the conductivity for an electron can be written as

$$\sigma = \sigma_0 exp(-\Delta E/kT) \tag{1.17}$$

where $\Delta E = E_C - E_F$ is called the activation energy and is the separation of E_F from the mobility edge E_C and σ_0 is the pre-exponential factor.

1.3.4 Hopping conduction

The hopping conduction is defined as electric conduction in which electronic jumping from one localized state to another quantum mechanically leading to carrier transport. The idea of hopping conduction was first explained for doped semiconductors [30, 31] and then it was extended to amorphous semiconductors [32]. The hopping may be aided by phonons and hence phonon-assisted hopping between sites will be treated here. Electron transport through localized state with in the band gap include

1. Movement of electron from one site (lower energy) to another (higher energy). A thermal energy is essential for this hopping which is known as thermally aided tunnelling.

2. Movement of electrons between the sites having same energy which is independent of temperature.

3. Movement of electron from higher energy site to lower energy site. Such hopping is the tunnelling process in which the emission of photon occurs.

According to Mott, the hopping conduction is simplified by assuming that the major contribution to the hopping current is through states within k_BT of the chemical potential μ, thereby avoiding the exact occupation probabilities of the states in the description [32]. Here hopping probabilities (P_{ij}) are the probability of a carrier tunnelling from a localized state i with energy E_i to void state j with energy E_j:

$$P_{ij} \approx \begin{cases} exp(-2\alpha R_{ij} - \frac{E_j - E_i}{k_B T}) & \text{if } E_j > E_i \\ exp(-2\alpha R_{ij}) & \text{if } E_j \leq E_i \end{cases} \tag{1.18}$$

with R the physical distance separating the two localized states, and α the localization parameter of these states. In a one-dimensional system the α parameter is the exponential decay of a wave function within a potential barrier and is directly proportional to the height of the potential barrier. In systems of higher dimensions this relation is not much correct, and the α parameter is characterized by an integration of all possible tunnelling paths between two sites. For the occurrence of hopping following conditions are required

1. Wave functions of the two localized states must interfere.

2. Occupied and empty states should exist for the hopping. This condition requires the hopping should happen between states close to the Fermi level.

3. An energy is required for the electron hopping from a localized state to another localized state with a higher energy level.

Nearest-neighbour hopping (NNH)

Nearest neighbour hopping (NNH) conduction is the hopping conduction in which an electron in a localized state attains required energy and moves to a nearest localized state with an energy E_{hop} above the former state. NNH conduction rate is limited by the thermal energy of electrons. Since the hopping probability relates on both the spatial

and energetic separation of the hopping sites, it is generally explained the hopping conduction in a four-dimensional hopping space, with three spatial coordinates and one energy coordinate. The range R in this hopping space is defined as

$$R_{ij} = -ln(P_{ij}) \tag{1.19}$$

This range, given by the magnitude of the exponent in equation 1.18, stand for a distance in four-dimensional hopping space, pointing the hopping probability. In a system in which localized states are arbitrarily distributed in both position and energy, the probability distribution function of all hops arising from one site is usually dominated by the hop to the nearest neighbouring site in the four-dimensional hopping space, due to the exponential character of the hopping probabilities. This site at closest range corresponds only with the spatially nearest neighbour if the first term on the right hand side of equation 1.18 is dominant. This is reliable if $\alpha R_0 \gg 1$, with R_0 the average spatial distance to the nearest neighbouring empty localized state. In cases of strong localization and/or low concentration of localized states, the hopping distance R is limited to the spatial nearest neighbouring hopping site at average distance R_0 and such conduction mechanism is called nearest neighbour hopping (NNH) which is schematically shown in the figure 1.7. When one electron move from one state to another, there could be a phonon absorbed or emitted. An activation energy E_{hop} is linked with the process of absorption of a phonon. The average distance of the two states depends on the concentration of the localized states.

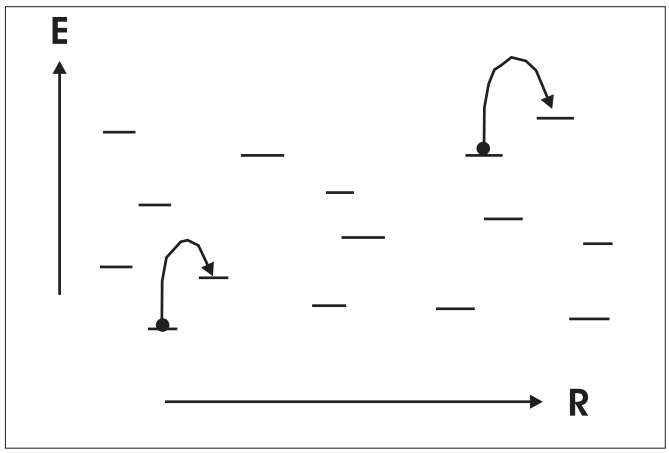

Figure 1.7: Schematic representation of nearest neighbour hopping

1.3.5 Variable range hopping

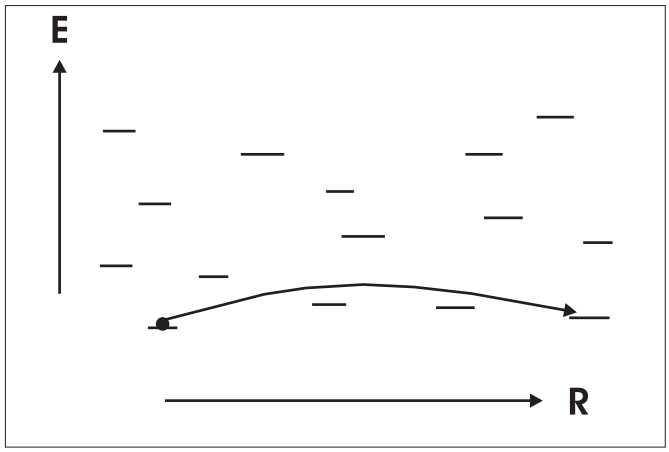

Figure 1.8: Schematic representation of variable range hopping

At lower temperature, the probability of the electron thermal activation between states that are close in space but far in energy be-

comes smaller than that of electron hopping between some more remote states whose energy levels happen to be very close to each other. In this case, the characteristic hopping length increases with decreasing temperature and such kind of hopping is known as variable range hopping (VRH) which is schematically shown in the figure 1.8. The temperature dependence of the conductivity is explained by Mott's law

$$\sigma = \sigma_0 exp\left(\frac{T_0}{T}\right)^{\frac{1}{4}} \tag{1.20}$$

with

$$T_0 = C_T \frac{\alpha^3}{k_B N_F} \tag{1.21}$$

proportionality constant C_T is given by $C_T = \frac{24}{\pi}$ and

$$\sigma_0 = \nu_{ph} \left(\frac{N_F}{\pi \alpha k_B T}\right)^{\frac{1}{2}} \tag{1.22}$$

The average hopping length d_{vr} as a function of temperature is

$$d_{vr} \propto (\frac{T_0}{T})^{\frac{1}{4}} \tag{1.23}$$

Hence as temperature decreases, the average hopping length increases as $T^{1/4}$.

1.3.6 Optical properties

One of the most significant properties of any amorphous solid is its optical property which is directly related to the structural and electronic properties of solids. In this regard, two very important and

related optical properties are the absorption coefficient and density of charge carrier states. A detailed knowledge about the absorption coefficient and density of charge carrier states can provide a huge amount of information on materials about their structure, optoelectronic behavior, transport of charge carriers, etc. In the case of localisation of electrons the effective mass approach is required to explain density of states (DOS). Systems having different effective masses of their charge carriers will have different density of electron states. charge carriers in amorphous semiconductors have generally a different effective mass than crystalline solids. Hence, the DOS of amorphous solids is expected to be different. For energies, $E > E_C$, in the conduction states, and $E < E_V$ in the valence states, the dependence of DOS on the energy agrees with what has been observed in most amorphous semiconductors. The sharp features ie the discontinuities in the slope in the DOS are the characteristics of crystalline solid . As the theory of DOS of Fermi free electron gas does suggest a sharp drop in the DOS at the mobility edges, which is not seen in any amorphous solid (Figure 1.2). The sudden drop can easily be seen by replacing E by ($E - E_C$) for conduction extended states and with ($E_V - E$) for valence extended states. Lack of a fully coordinated network of atoms and disorders present in the amorphous solids, influence the DOS near the mobility edges.

At energies near the mobility edges, E_C or E_V and within the mobility gap in amorphous solids, the non-zero DOS arises from the localized tail states arising from the disorders. It is impossible to build up a single approach that can explain the DOS near the mobility edges, below E_C in the conduction states, and above E_V in the valence states, which are the regions of localized tail states in amorphous semiconductors.

Absorption coefficient

As shown in the figure 1.9 there are three distinct regions, A, B and C, observed in the absorption coefficient of amorphous semiconductors near the electron mobility edge. In the region of strong absorption (region A in figure 1.9) above the mobility edge, the relation between the absorption coefficient α and photon energy $h\nu$ can be explained as [33, 34],

$$\alpha h\nu \propto (h\nu - E_0)^2 \tag{1.24}$$

where E_0 is the optical gap. Usually equation 1.24 is written as

$$(\alpha h\nu)^{1/2} = C(h\nu - E_0) \tag{1.25}$$

where C is not depend on photon energy. A plot of $(\alpha h\nu)^{1/2}$ as a function of the photon energy $h\nu$ is known as Tauc plot, and the extrapolation of straight line region into the energy axis would give the optical energy band gap E_0 (Tauc gap) [23, 35, 36]. Equation 1.25 is derived only for transitions from valence extended to conduction extended states without the involvement of any tail states and it is assumed that the matrix element is independent of the energies in the conduction and valence extended states. Hence the obtained optical gap should match to the situation where there are no tail states, as in crystalline solids.

In the low absorption region that is region B in figure 1.9, α increases exponentially with energy. In this region it can be explained by the equation as

$$\alpha \propto exp(h\nu/E_U) \tag{1.26}$$

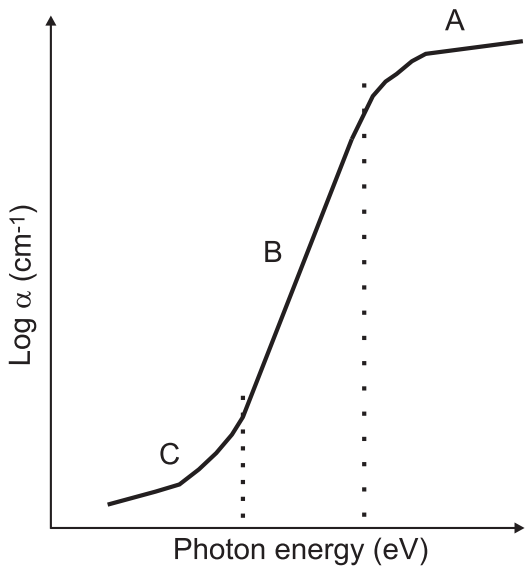

Figure 1.9: Three principal regions of optical absorption in amorphous semiconductors

where E_U is the he Urbach tail which is the width of the localized tail states. In the region C of figure 1.9, the absorption coefficient is described as another exponential function of the photon frequency

$$\alpha \propto exp(h\nu/E_d) \tag{1.27}$$

where E_d is the width of the defect states, and usually it is found that E_d is larger than E_U. The region C is so sensitive to the structural properties of materials [37].

Some times for amorphous solids, experimental data exhibit slight change from the square relations derived in equation 1.25 and a cubic dependence on the photon energy given by equation

$$(\alpha h\nu)^{1/3} = C_F(h\nu - E_0) \tag{1.28}$$

The above relation therefore used it to determine the optical gap E_0 and has been found to more apt with some experimental data. Here C_F is another constant [38]. The cubic dependence on photon energy can be accepted only when the DOS have linear relation with energy, provided the assumption of constant transition matrix is valid for every amorphous solid. Mott and Davis proposed the cubic root dependence, on the basis that the DOS may depend linearly on energy near the optical gap. Hence it is very difficult to obtain the unique value for the optical gap for any amorphous semiconductors. This also originate a question, whether optical gap is same for all amorphous samples of the same material with same dimension, but prepared at different times or by different technique. The ratio of the number of defect and weak bond states to that of the extended states shall affect the ratio of their widths. The ratio of the effective mass of charge carriers in the tail states to that in extended states depends on the ratio of width of the tail states to that of extended states [22].

In Cody's method of analysing the matrix element [39], it is treated as a dependent function of energy, which direct to an expression like:

$$(\alpha h\nu) = (h\nu)^2[h\nu - E_0]^2 \tag{1.29}$$

Thus there are two different ways of analysing the transition matrix element. Applying one approach it is found to be independent of the energy and momentum of the excited charge carriers, but the second approach shows that it depends on the photon energy and hence on energy of charge carriers. If one uses the first approach, then $(\alpha h\nu)^{1/2}$ is found to give the correct Tauc's plot (i.e. it is linear with the photon energy). However, if the second method was used, then $(\alpha/h\nu)^{1/2}$

would give the correct Tauc's plot. As the objective of Tauc's plot is to determine the optical gap, one may expect both approaches will produce the same value for the optical gap.

The DOS can be made to have parabolic relation with energy (equation 1.2) for any particle by connecting it with suitable effective mass. Hence absorption coefficient, obtained within the assumption of constant transition matrix element, will have the square root dependence on energy involving a different effective mass. The variation in Tauc's plot cannot be described by assuming the constant matrix element. Employing energy dependent matrix element, the RHS of equation 1.29 is a forth-order polynomial. Depending on which term on the polynomial may dominate, one can attain a deviation from Tauc's plot. Therefore in a material with a change from Tauc's plot is observed the transition matrix element may not be constant.

1.4 p-Type transparent oxide semiconductors

Semiconductor electronics and optoelectronic devices are an integral part of our lives, permitting us to pass on and target information almost anywhere and anytime with ever-increasing speeds. Transparent conducting oxides (TCO) are well known and have been widely used for a long time in optoelectronic applications as well as in research fields. It is generally believed that high optical transparency is mismatched with high electronic conduction, since large band gap is required for optical transparency and such a large gap makes carrier doping very difficult. The first transparent conducting thin films of cadmium oxide (CdO) was reported in 1907 by Badekar[40] who synthesied the films by thermal oxidation of sputtered films of cad-

mium. Later In_2O_3: Sn (ITO), was reported by Rupperecht [41] in 1954, followed by other TCOs (SnO_2 and ZnO). TCOs are being used extensively in the window layers of solar cells, as front electrodes in flat panel displays, low-emissivity windows, electromagnetic shielding of cathode-ray tubes in video display terminals, as electrochromic materials in rear-view mirrors of automobiles, oven windows, touch-sensitive control, panels, defrosting windows in refrigerators and airplanes, invisible security circuits, gas sensors, biosensors, organic light emitting diodes (OLED), polymer light emitting diodes (PLED), antistatic coatings, cold heat mirrors, etc.[1, 3, 4, 8, 42–54]. The room temperature deposition of TCOs onto polyethylene terephthalate (PET), polyamides and other polymer substrates in roll-coating processes for touch-screen and infrared reflector applications are the recent challenges for the TCO industries [55, 56].

Although the TCOs have a vast range of applications as mentioned above, very little work has been done on active device fabrication using TCOs [57, 58]. This is because most of these materials are of n type in nature and their use as oxide semiconductors is some what limited due to their monopolarity. In order to extend the use of TCOs to a range of additional applications such as transparent light emitting diodes, UV detectors, solar cells, etc. it is important to synthesis p-type TCOs. The conduction type of TCO materials had been limited to n-type semiconductors and possibility of simultaneous transparency and conductivity is rarer in p-type. The search for high mobility p-type wide bandgap semiconductors to substitute these n-type materials has been a major research thrust for more than 15 years. It must be mentioned here that the first report of a semitransparent p-type conducting thin film of nickel oxide (NiO) with 40% transmittance, was published in

1993 by Sato et al [59]. One of the major event in this area in recent years is the discovery of a p-type TCO, $CuAlO_2$, with delafossite structure in 1997 [60], which spark off the development of a series of p-type TCOs and transparent pn junction devices such as light emitting diodes (LEDs) [61].

1.4.1 Challenges

As compared to n-type transparent semiconducting oxides (TSOs), it is very hard to achieve good hole conduction because of O 2p orbitals, which form hole transport paths in many oxides, are rather localized, therefore hole effective masses are quite large and VBM levels are deep. p-Type conduction is related with carrier drift through a valence band. The significant characteristics of wide bandgap p-type semiconductors is the relatively low mobility of these carriers in comparison with those in a conduction band. Carrier mobility have an inverse relation with the band effective mass, which is in turn inversely proportional to the band curvature. Hence narrow or flat energy bands is the reason for low mobility. Valence bands are generally derived from tightly bound states. For example, it is usual to find valence bands derived from highly directional p or d orbitals, while conduction bands are derived from spherical and diffuse s orbitals. Hence the spatial overlap of atomic orbitals that form the valence band is smaller than that of conduction bands, and valence bands are consequently narrower and correspondingly less disperse. Another component that influence mobility is carrier scattering from neutral and ionized impurities. In fact such scattering is same for p-type and n-type materials, but if the mobility is very small, a higher carrier concentration is essential to achieve

a particular conductivity. This results in a higher concentration of ionized and, neutral impurities that enhance scattering and further lower the mobility. A compromise in transparency also occurred due to the enhancement of optical absorption from free carriers or tail states. The dispersion of VBM could be modified by (a) reducing the nearest neighboring oxygen-oxygen distance, (b) using hybridization of metal orbitals whose energy levels are nearer to those of O 2p or (c) using more extended orbitals for anions. Here we followed approach (b) and selected Cu^+ based oxides because the energy levels of Cu 3d are close to those of O 2p and the closed-shell configuration of Cu^+ $3d^{10}$ was expected not to give optical absorption in the visible region due to d-d or O2p-Cu3d transitions,which therefore met the requirements to keep optical transparency in the visible region [62]. Doping of wide bandgap p type semiconductors without compromising transparency is a challenging task. The dopants should induce shallow defect states so that band-to-defect absorption happens at energies either above or below the visible range. The ability of acceptor dopants to create hole carriers is compromised by the formation of compensating donor states. The cost of compensation is the formation energy of the donor state, but this is offset by the energy gain that results when a electron in the donor level relaxes to the acceptor state. Formation energies are almost similar for all materials , but the energy reduction from hole-filling generally scales with the gap energy. Wide bandgap materials are therefore more sensitive to compensation. Formation enthalpies of various defects as a function of the Fermi-level position and chemical potential to assess whether a particular doping strategy is likely to be successful [63, 64].

The introduction of defects may shift the Fermi level of a semicon-

ductor. The Fermi energy displace towards the valence band because of the introduction of acceptors, the formation enthalpy of donors reduces to the point where spontaneous generation of donors renders further attempts to introduce acceptors ineffective for the purposes of carrier generation. This depends further on the chemical potential of the system. For instance, in the case of a compound semiconductor, the enthalpy of formation of acceptor states is favored when the system is anion rich. The spontaneous formation of these killer defects leads to the idea of a Fermi level pinning.

If the pinning level corresponding to spontaneous generation of hole killers lies well above the valence band, then it is not possible to p-type doping.If it is near or even below the valence band, the material can be easily p-doped. If semiconductor band edges are aligned according to their band offsets, then the observed Fermi pinning levels in different materials within classes of semiconductors are remarkably similar relative to the vacuum level [65, 66]. This suggests that the positions of the VBM and CBM relative to the vacuum level also determine the dopability of a semiconductor. A large electron affinity reduces the CBM towards the upper pinning level or even below it, which in turn promotes n-type dopability. Conversely, a small ionization potential lift the VBM towards or above the lower pinning level, which implies p-type dopability. This is the general scheme to explains the doping trends in many wide bandgap semiconductors.

1.4.2 Criteria to choose p-type TCO

It is very difficult to prepare binary metal oxides with p-type conductivity because of the electronic structure of these metal oxides.

Strong localization of holes at upper valence band of oxygen 2p is due to strong Coulomb force exerted by the oxygen ions., ie the ionicity of metallic oxides cause this localization. O 2p levels are lying lower than the valence orbit of metallic atoms [67], leading to the formation of a deep acceptor level by the holes. Hence the holes have high probability to be localized around the oxygen atoms. Hence these holes need a large amount of energy to overcome a large barrier height in order to migrate within the crystal lattice, resulting in poor conductivity and hole mobility. According to Kawazoe et al [68] the possible solution is to introduce a degree of covalency in the metal oxygen bondings to induce the formation of an extended valence band structure, the valence band edge should be altered by mixing orbitals of appropriate counter cations that have energy filled levels comparable to the O 2p level. This would lower the strong coulombic force by oxygen ions thereby delocalizing the holes. Chemical Modulation of the Valence Band (CMVB) is the essential approach employed to obtain p-type TCO [68]. Two important requirements for the reduction on the localization of metallic oxide are, electronic configuration of cation species and the crystal structure of oxide. The localisation of metallic oxide was found to reduced by cations to have closed shell, such as Cu^+, Ag^+ and Au^+. From the detailed investigation it was clear that required cationic species are the $3d^{10}$ -closed shell of Cu^+ ions and $4d^{10}$ -closed shell of Ag^+ ions [68, 69]. Although some transition metal cations with an open d-shell may satisfy the energy requirement [70] for CMVB technique they show pretty coloration due to a d-d transition, which is not a property of transparent materials. Hence the investigation has been concentrated towards the cations with closed ($d^{10}s^0$) electronic configuration. Figure 1.10 shows a schematic illus-

tration of CMVB.

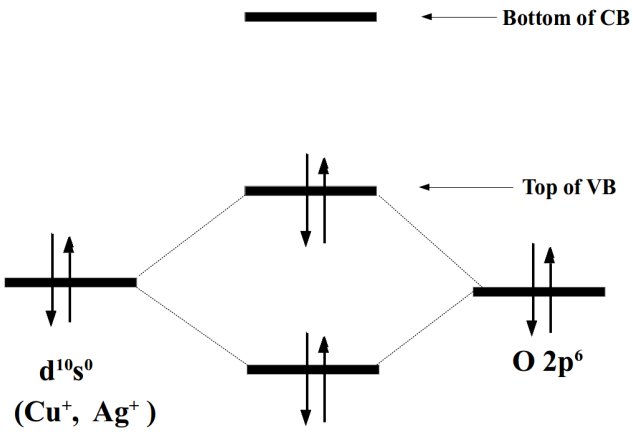

Figure 1.10: Schmatic diagram of CMVB method [68]

Next is the structural requirement to propose p-type TCO materials. Tetrahedral coordination of oxide ions is more apt for p-type conductivity, as it acts in reducing the localization behavior of 2p electrons on oxide ions [68]. The valence state of the oxide ions shall be expressed as sp^3. Eight electrons (including $2s^2$) on an oxide ion are distributed in the four s bonds with the cations. This electronic configuration reduces the non-bonding nature of the oxide ions and enhances the delocalization of holes at the valence band edge, which is the reason of p-type conductivity in Cu_2O [71–74]. But Cu_2O, although p-type in nature, has rather small bandgap (2.17 eV) [72]. The narrow band gap (2.17eV) is probably because of the three-dimensional interactions between $3d^{10}$ electrons of neighboring Cu^+ ions. It is expected that the low-dimensional crystal structure would keep down this interaction [75]. For a better transparent conducting oxides, the bandgap of the material (Eg) should be higher than 3.1 eV. Hence enhancement

of bandgap would be another structural requirement for designing p-TCO, so that there is no absorption of visible photons.

1.4.3 Delafossite

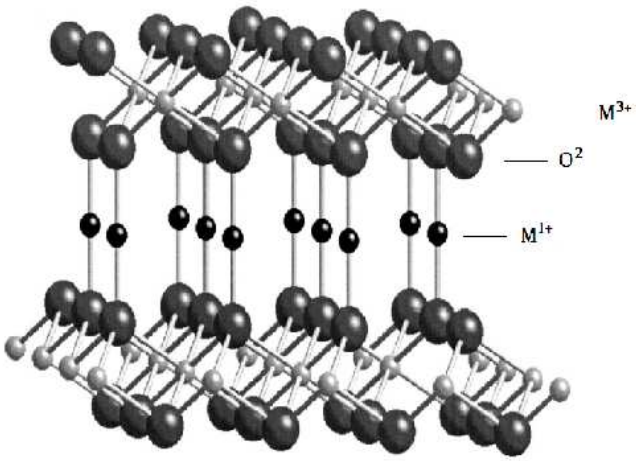

Figure 1.11: Delafossite crystal structure

Materials with delafossite crystal structure ABO_2 (A is Monovalent and B is trivalent) were chosen as the candidates for p-TCOs for several reasons. The atomic structure of delafossite group consists of a sheet of linearly coordinated A cations stacked between edge-shared octahedral layers (BO_6). In the delafossite atomic structure there are two alternating planar layers. One layer of triangular-patterned A cations and a layer of edge-sharing BO_6octahedra compacted with respect to the c-axis [76]. The delafossite structure can have two polytypes. According to the orientation of the planar layer stacking delafossite structure can be divided into two, Hexagonal 2H types with a space group of P63/mmc and a rhombohedral 3R type with

a space groupof R$\bar{3}$m. Delafossite crystal structure is shown in the figure 1.11. To understand the electrical transport and optical properties of the wide bandgap semiconductors, it is necessary to appreciate the unique aspects of the crystal structure. The delafossite materials $CuMO_2$ have an anisotropic trigonal/ hexagonal structure [77]. The Cu and M atoms lodge in discrete layers extending in the ab plane that are alternately arranged along the c axis. The Cu atoms are coordinated by two O atoms to form linear CuO_2 sticks and the M atoms are coordinated by six O atoms in some what distorted MO_6 octahedra. In this arrangement, the CuO_2 units are isolated one from the other and hence there are no Cu-O-Cu interactions. Oxygen atoms at the ends of the CuO_2 units are shared with six M atoms, occupying a distorted tetrahedral surroundings. Each Cu and M atom has three nearest neighbors of the same type with Cu-Cu and M-M distances scaling with the radii of the M atoms. corresponding distances are 2.86,2.98 and 3.21$\mathring{A}$ for M = Al, Ga and Sc, respectively, which compare with the Cu-Cu distance of 2.7 $\mathring{A}$ in Cu metal. Delafossites materials have the closed shell d^{10} electron configuration of Cu^+, a large energy separation between the Cu 3d and Cu 4s levels, and the isolated nature of the CuO_2 structural units. Apart from the structure hole conductivity in Cu (I) oxides is probably to be realized by direct Cu-Cu interactions and mixing of Cu 3d and O 2p orbitals near the top of the valence band, which can render broader bands than realized with O 2p orbitals alone. The presence or introduction of defects or appropriate acceptor dopants cause p-type conductivity. Cu-O orbital mixing near the top of the valence band was revealed from band structure calculations [78–80]. In the Delafossites the hole concentrations could be set through formation of vacancies, substitution of acceptors

on the Cu and M sites, incorporation of oxygen interstitial in to the Cu planes or combination of these features.

The first and the most relevant material in this group is copper aluminum oxide ($CuAlO_2$). p-Type conductivity of ($CuAlO_2$) was first reported by Benko and Koffyberg [81]. Kawazoe et al [60] first developed $CuAlO_2$ in transparent thin film. Structure of ($CuAlO_2$) belongs to the $R\bar{3}m$ D^{3d} space group with rhombohedral crystal structure [86]. Other p-TCO thin films belonging to this group are copper gallium oxide ($CuGaO_2$) and copper indium oxide ($CuInO_2$) [82–84]. The lattice parameters and band structure of these materials were reported [75, 81, 87–91]. Iron doped copper gallium oxide ($CuGaO_2$:Fe), calcium doped copper indium oxide ($CuInO_2$:Ca), magnesium doped copper scandium oxide ($CuScO_2$:Mg), magnesium doped copper chromium oxide ($CuCrO_2$:Mg), calcium doped copper yttrium oxide ($CuYO_2$:Ca) etc are already reported [83–85, 92–94]. Preparation of some other new delafossite materials such as $CuFe_{1-x}$ V_x O_2(x= 0.5), Cu-$Ni_{1-x}Sb_x$ O_2, $CuZn_{1-x}Sb_x$ O_2, $CuCo_{1-x}$ Sb_x O_2, $CuMg_{1-x}$ Sb_x O_2, $CuMn_{1-x}$ Sb_x O_2(x = 0.33) in powder form had been reported to have high resistivity [97]. Preparation of 10% Sn doped $CuNi_{1-x}$ Sb_x O_2 thin film has been reported by the same group [85, 97], having reasonable transparency and conductivity. Among the delafossite structure oxides, $CuCrO_2$ has a resistivity of the order of 1 cm, and upon doping with 5% Mg the resistivity can be lowered to 0.045 Ωcm, which is the lowest resistivity in the delafossite systems [97]. Reported transmission values for materials $CuAlO_2$ $CuGaO_2$ $CuInO_2$ are 70% , 80%, and 70% respectively at wavelengths greater than 500 nm [60, 82, 98]. These transmission values are still lower than to n- type materials which have typical transmissions of 90% over the entire visible spectrum. As far as the

active device fabrication is concerned, it is very important to have a lattice matching between both the p and n types materials. Presently a major thrust of research in this field is to propose p-type materials, which can exhibit almost similar transmission characteristics as compared to n -type TCOs. $CuBO_2$ is considered a potential system because of recent theoretical investigations [99, 100], which predicts that the band gaps of $CuMO_2$ should increase as the ionic radius of M decreases. According to these postulates $CuBO_2$ should have the largest band gap and hence better transmission in visible spectrum. A study by Snure and Tiwari has identified delafossite $CuBO_2$ as a new p-type TCO [275]. $CuBO_2$ thin films of prepared by Snure have shown an appreciable room temperature electrical conductivity of 1.65 S/cm, and a direct optical band gap of 4.5 eV. Santra et al reported a new cost effective sol-gel technique to synthesize the $CuBO_2$ nanopowders [276].

1.4.4 Binary oxides

SnO, NiO and ZnO are the important non-Cu-based p-type oxides. Tin oxides have recently attracted much attention as a novel p-type material. Tin oxide is one of the most relevant p-type materials simply due to its relatively high hole mobility and stability. Hosono group established p-channel operation using SnO thin films [101]. Even though SnO_2 is generally known as a n-type semiconductor, Ni et al [102] and Ou et al [103] fabricated p-channel SnO_2 TFTs. This indicates that the general concept relating to phase identification of tin oxide and the determination of electrical property is still obscure. It is reported that binary oxides such as SnO_2, ZnO shows p-type conductivity due to

oxygen enrichment in the sample. Origin of holes may be from cation vacancy, interstitial oxygen and the mixed valance state of Sn^{2+} and Sn^{4+} [104].

NiO has been known as a p-type semiconductor with a band gap of about 3.5-3.8 eV, and it is insulating when stoichiometric. p-Conductivity can be achieved by the introduction of Li, which results in the formation of Li^{+}-Ni^{3+} acceptor complexes, or by making nonstoichiometric $Ni_{1-x}O$ in highly oxidizing conditions[105]. Sato et al [59] reported Conductive thin films of NiO [59]. NiO with transparency 55-60% has been employed as a hole transporting/electron blocking anode interfacial layer in organic solar cells [106].

p-Type conductivity in ZnO is a highly desirable goal given its environment friendly composition, excellent optical transparency, the ease of inducing complementary n-conductivity, and its large exciton binding energy. The p-type conductivity with low-carrier-density can be obtained by doping with N and P on the oxygen site and this p-conductivity can be increased by eliminating the abundant native donors by careful growth methods. A p-i-n homojunction has been demonstrated with all ZnO layer with hole concentration of 10^{16} cm^{-3} [107]. The attempt to develop p-ZnO was first made by Lander [108]. Later appreciable experiments were made to produce p-ZnO doped with N [109–114]. Recently Yamamoto and Yoshida [115] suggested that co-doping of donor-acceptor dopants in ZnO might lead to p-type ZnO. Joseph et al [116] succeeded in the fabrication of p-ZnO using co doping. In this method both acceptor and donor are simultaneously doped into the ZnO lattice with an acceptor concentration double that of the donor concentration to get a dominated p-type conductivity in ZnO. But several reports pointed out difficulties and a lack of repro-

ducibility of p-ZnO employing the co-doping method [117–119].

1.4.5 Transport properties

Defect levels that are either native to the material or deliberately introduced is the reason for conductivity in wide band gap semiconductors. Extrinsic doping by substitutional cations and anions yield control, but native defects are equally important and different native defects may dominate under various processing conditions. If the defect levels are within tens of meV of the band edge, they generate carriers at levels high enough to let appreciable conductivity. Degenerate doping creates free carriers at densities about two orders of magnitude smaller than in metals. Degenerate conduction has been obtained in BaCuTeF and LaCuOSe:Mg at carrier densities approaching $10^{20}$to 10^{21}cm^{-3}. Conductivity of many of the p-type wide band gap materials show strong dependence with temperautre, ie lower conductivity with decreasing temperature following a relation as

$$\sigma = \sigma_0 e^{-(\frac{T_0}{T})^n} \tag{1.30}$$

When n=1, the activation energy of carriers from defects into the band (or across the band in the case of intrinsic conductivity) can be easily obtained from a plot of semi logarithmic conductivity with inverse temperature. In classic band theory of conduction, number of carriers is exponentially related to temperature, while the carrier mobility is more weakly temperature dependent. When n=1/4, the conductivity is called as variable range hopping, and carrier motion is considered to be a combined effect of thermally activated hopping and carrier tunneling from site to site within an impurity band or low-mobility

states in band tails. When strong interactions of the carriers with the lattice result local distortions, the effective inertia of the carriers is increased, and the mechanism is called as polaron conductivity [120].

1.5 An overview of the development of thin film transistors

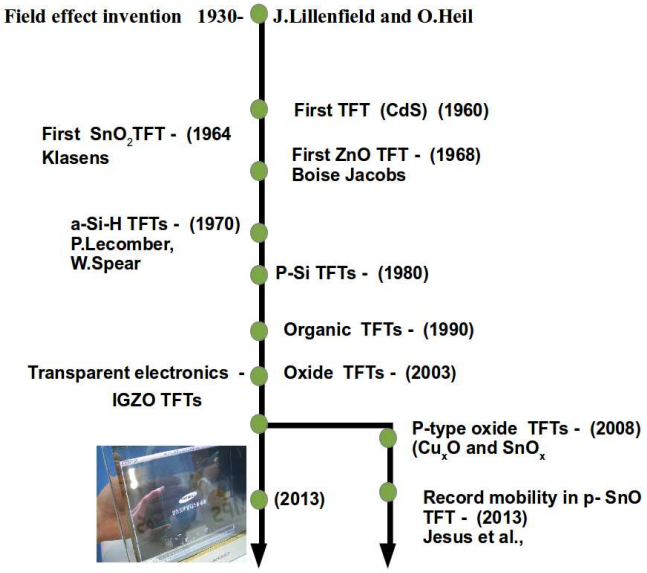

Figure 1.12: Major achievements in the field of TFTs

The history of TFTs begins from the invention of the metal insulator field effect transistor in 1925 which was patented in 1930 by J.E. Lilienfeld [121–123] and O. Heil [124]. The basic principle of semiconductor field effect transistor (MESFET) was reported in 1930.

The first TFT was fabricated by Weimer in 1962 [125, 126]. Weimer

used a vacuum technique evaporation to deposit gold electrodes, a polycrystalline cadmium sulfide (CdS) n-type semiconductor and a silicon monoxide insulator, using shadow masks. Later Weimer relpaced the cadmium sulfide channel layer by cadmium selenide which made a better improvement in the transistor performance.

Klasens and Koelmans proposed in 1964 a TFT with an evaporated SnO_2 semiconductor on glass, with aluminium source-drain and gate electrodes and an anodized Al_2O_3 gate dielectric [127].

In 1968, Boesen and Jacobs [129] reported a TFT with a lithium-doped ZnO single crystal semiconductor, with SiO_x dielectric and aluminium electrodes. Drain current (I_D) modulation by applying a gate voltage (V_{GS}) was a very small and no drain current saturation were observed on these devices. In 1970 Aoki and Sasakura [130] fabricated SnO_2 TFT with poor electrical performance. TFTs using hydrogenated amorphous silicon (a-Si:H) was first fabricated by Spear and Le Comber in 1975 [131]. The a-Si:H TFT was identified as the most appropriate device for large-area AMLCDs soon after its invention [132]. In 1981, they proved that a-Si TFTs can be used to drive liquid crystal displays (LCDs)[133]. In 1983, Sharp established a prototype 3-inch full color LCD panel. In 1988, Sharp developed a 14-inch TFT LCD and attested that a-Si TFT LCDs are flat panel displays (FPDs) that will replace cathode ray tube (CRT) displays and become the mainstream of next-generation displays. In 1996 oxide semiconductors SnO_2:Sb and In_2O_3, were used as channel layers for ferroelectric field-effect devices by Prins et al and Seager respectively [134]. Over the last few years, much interest has been shown in the development of TFTs with wide band gap semiconductor channel layers. In 2003 report appeared on the literature on good performing fully transparent

ZnO TFTs with TCO based electrodes and its mobility was high (2.5 $cm^2V^{-1}s^{-1}$) as compared to a-Si-H and organic TFTs [135, 136, 138]. Room temperature deposited ZnO channel layer was used by Carcia et al [136] for the fabrication of transparent TFTs. A bunch of papers relating to the oxide semiconductors were published after the year 2004 with high mobility and depostion of channel layer at room temperature [139–141]. Non-vacuum deposition of ZnO channel layer was also successful for the fabrication of TFTs [142]. Completely transparent ZnO TFTs were fabricated at room temperature [144]. ZnO and In_2O_3 nanowires were employed as a channel layer for the fabrication of TFTs [145–147]. In 2003 Nomura et al [148] demonstrated a complex $InGaO_3(ZnO)_5$ single crystalline semiconductor layer TFT channel with mobility 80 $cm^2V^{-1}s^{-1}$, turn on voltage of -0.5 V and on/off ratio of 10^6. Among the various types of channel layer materials, amorphous oxide semiconductors (AOSs) appear to promising, especially when the factors of large area deposition on flexible substrates and their mechanical stability are concerned. Following the Nomura's work, number of publications appeared in following years relating the application of amorphous multicomponent oxides as channel layers in TFTs. Combining different cations with (n-1) $d^{10}ns^0$ (n=4) electronic configuration [149], multicomponent oxides like zinc tin oxide (ZTO) [150–153] and indium gallium zinc oxide [IGZO] [154–159] were also investigated for TFT applications. The tremendous achievements in n-type oxide semiconductors and its application to TFTs has activated the research in p-type oxide based semiconductors for TFT applications. However, up to the date there is no report about p-type oxide TFTs with similar performance as n-type oxide TFTs. p-Type oxide TFTs are mainly restricted by the small hole mobilities since the

mobility of valence band derived holes is generally lower than that of conduction band derived electrons, as in the case of n-type conductivity.

In organic TFTs most of the reports are on p-type channels [160–163]. Organic materials have been explored and the important developments in the semiconducting properties associated to the invention of electroluminescence in organic diode structures make these materials as splendid candidates for low-cost electronic and optoelectronic devices [164, 165]. Low temperature fabrication is the main attraction of organic materials which leads to flexible displays. Even though intense research have been carried out in the field of organic TFTs, the overall device performance is still poor as compared to oxide materials [166] (low mobility, poor stability. N-type organic semiconductors are also having lower mobilities restricting their field of applications in CMOS [167–169]. The success in high performance p-type oxide TFTs will definitely lead to a new era for electronics in rigid and flexible substrates, apart from silicon. Moreover, it will frame the electronics of tomorrow by the fabrication of complementary metal oxide semiconductors (CMOS). For p-type oxides, valence band is mainly derived from the oxygen p-orbitals, which badly reduce the carrier mobility. Hence p-type oxides have poor carrier mobility compared to their n-type oxides, which is the main hindrance in getting high performance p-channel oxide TFTs. There are only two oxides (SnO and Cu_xO) that have been successfully employed as channel for TFT. Now Cu based semiconductors are attracting the renewed interest in which the delafossite family $CuMO_2$ (M = Al, Ga, In, Y, Sc, La, etc.) is the most important.

1.6 Relevance of present work

Semiconductor electronics based on oxide materials are integral part of our lives, allowing us to communicate and direct information almost anywhere and anytime with ever-increasing speeds. To establish semiconductor electronics, both n-type and p-type conductivity is essential. Simultaneous transparency and conductivity is rarer in p-type as compared with n-type semiconductors. Mobility of p-type semiconductors are very low because of valence band derived carrier as compared to conduction band derived carriers in n-type semiconductors. The reported transparent circuits to date [170] are based on only n-type materials (oxides of Zn, Sn, In, Ga, and others as well). Transparent electrodes in commercial use (ITO, SnO_2:F, ZnO:Al) are also all n-type materials. The success in n-type semiconductors and its optoelectronic derive application motivated the interest in p-type oxide semiconductors which can be used for TFT applications. The research on high-mobility p-type wide band gap semiconductors to complement these n-type materials has now been undergoing for more than 10 years. From the literature review it is clear that to the date there is no report on p-type TFT which compliment the n channel oxide TFTs. Only two p-type channel layer (SnO and Cu_xO) have been explored for TFT applications and there is no report on room temperature deposited p-type channel layers. This work mainly focused on developing room temperature deposited p-type transparent oxide semiconductors and its application in thin film transistors. Even though the copper oxide is well known p-type semiconductor, now it is attracting a renewed interest as potential candidate for optoelectronic applications. Reported mobility for room temperature deposited Cu_xO TFTs are less

than one. In the present study we have made an attempt to enhance the mobility by optimising the growth parameters of Cu_xO channel layer. Possibility of fabrication of the p-type transparent CuO TFT also investigated since the narrow window of oxygen partial pressure to form Cu_2O phase, even though CuO have lower band gap. Delafossite oxide materials ($CuMO_2$) are identified as wide band gap p-type oxide semiconductors, But there is no report on TFT application using these materials yet. In the present study we have developed copper boron oxide and copper chromium oxide using room temperature co-sputtering technique. Single target preparation by normal solid state reaction method is very difficult for copper boron oxide due to the low melting point of boron. In delafossite family $CuBO_2$ is expected to have wide band gap because of the the smaller ionic radius of boron. Hence the room temperature deposited $CuBO_2$ will open a new frontier of transparent electronics. A p-n heterojunction is successfully fabricated using p-type copper boron oxide thin films which is the first report on heterojunction using copper boron oxide. Copper chromium oxide is reported with highest conductivity among p-type oxide materials with doping of Mg. Until now there is no report on TFTs fabricated using $CuCrO_x$ channel layer. In this work we have made an attempt to fabricate p-channel TFTs using room temperature deposited copper chromium oxide thin films. Development of wideband gap p-type oxide material discussed in this thesis shall make a pathway to transparent electronics.

Chapter 2

Experimental techniques, characterisation tools and basic operation of thin film transistors

Various techniques that have been used in the process of thin film deposition is discussed in this chapter. RF magnetron sputtering deposition technique was used for the development of thin films and fabrication of TFTs. Various thin film characterisation tools viz, stylus profiler, glancing angle X-ray diffraction, atomic force microscopy, X-ray photo electron spectroscopy, TEM, Raman spectroscopy, Hall effect measurements, UV-Vis-NIR spectrophotometer and FIB cross sectional SEM were used for charecterisation and optimisation of thin film deposition. The working principle of thin film transistors and extraction of the various device performance parameters like thresh-

old voltage, mobility, subthreshold voltage swing, on-off ratio etc are reviewed towards the end of the chapter.

2.1 Experimental techniques

Study of the various material properties in the bulk form is highly beneficial in transparent electronics. But in the optoelectronic device applications, the materials in the thin film form having the interesting properties of bulk material is appreciated. A thin film is defined as a low-dimensional material formed by condensing, one-by-one, atomic/molecular/ionic species of matter. The thickness of a thin film is generally less than a few micrometers. A thick film is defined as a low-dimensional material developed by thinning a three-dimensional material or assembling large clusters/aggregates/ grains of atomic/molecular/ionic species [171]. Thin films have been utilized for more than a period of 50 years in fabricating electronic devices, optical coatings, hard coatings, and for decorative coatings. A thin film deposition technique begin with a random nucleation process followed by nucleation and growth stages. Thin film properties have strong dependence with methods of deposition, substrate materials, substrate temperature, rate of deposition and back ground pressure. The nucleation stage can be altered remarkably by external agencies, such as electron or ion bombardment. Film micro-structure, associated defect structure, and film stress depend on the deposition conditions at the nucleation stage. The basic properties of film, such as film composition, crystal phase and orientation, film thickness, and micro-structure, are controlled by the deposition conditions.

The chemical composition of deposited films is controlled by the

substrate temperature and/or the deposition atmosphere. Under low substrate temperatures, the chemical composition of deposited films coincides with that of the source materials. Under high substrate temperatures, the chemical composition of deposited films differs from the source materials due to the re-evaporation of high vapor pressure materials from the films during the deposition.

Thin films exhibit unique properties that cannot be observed in bulk materials: unique material properties resulting from the atomic growth process like size effects, including quantum size effects, characterized by the thickness, crystalline orientation, and multi-layer aspects.

Almost all thin-film deposition and processing method employed to characterize and measure the properties of films requires either a vacuum or some sort of reduced-pressure ambient. Different techniques like evaporation, sputtering, laser assisted deposition, chemical vapor deposition etc are widely used for thin film fabrication. The decision of whether to evaporate, sputter, or chemically deposit thin films for particular applications is not always obvious and has fostered a lively competition among these alternative technologies.

Chemical vapor deposition (CVD) is the process of chemically reacting a volatile compound of a material to be deposited, with other gases, to produce a nonvolatile solid that deposits on a suitably placed substrate [173]. It is different from physical vapor deposition (PVD), which relies on material transfer from condensed-phase evaporant or sputter target sources. CVD technique is widely used for commercial application because it don not vacuum or unusual level of electric power as compared to PVD. Since CVD technique is subject to thermodynamic and kinetic limitations and constrained by the flow of

gaseous reactants and products, it is usually more complicated than those involving PVD.

2.1.1 Sputtering

Sputtering is the most versatile deposition technique used for high quality thin films over a large area with better control of composition and thickness, better addition and homogeneity Sputtering is a process by which atoms are ejected from a solid target material due to bombardment of the target by energetic particles. Sputtering has become a commercial deposition technique for different industrial applications especially in semiconductor industry where it is is widely employed in the metallization process for the fabrication of integrated circuit. Various sputtering methods are suggested for thin-film growth including dc diode, RF diode, magnetron, and ion-beam sputtering.

Mechanism of sputtering

Two theoretical models suggested for sputtering are
1. Thermal vaporization theory; the surface of the target is heated enough to be vaporized due to the bombardment of energetic ions.
2. Momentum transfer theory; surface atoms of the target are emitted when kinetic moments of incident particles are transferred to target surface atoms.
In earlier stage the thermal vaporization theory was considered the most important mechanism which was supported by Hippel in 1926, Sommermeyer in 1935 and Townes in 1944 . In 1956 the detailed study by Wehner proved that the most important mechanism is not thermal vaporization but the momentum transfer process. At present

sputtering is believed to be caused by a collision cascade in the surface layers of a solid

The target material and the substrate is placed in a vacuum chamber for sputtering. After evacuating the chamber argon atoms are introduced into a vacuum chamber at a pressure of 1 to 10 mTorr. A voltage is applied between them so that the target is the cathode and the substrate is attached to the anode. High voltage across cathode and anode can ionize argon atoms and generates a plasma, hot gas-like phase consisting of ions and electrons, in the chamber. This plasma is also known as a glow discharge due to the light emission. These argon ions are now accelerated towards the target. Their collision with the target ejects target atoms, which travel to the substrate and eventually settle. The momentum transfer from the particles to the surface atoms can impart enough energy to allow the surface atoms to escape. Ejected atoms (or molecules) can travel to a substrate and deposit as a film. Electrons ejected during argon ionization are accelerated to the anode substrate, subsequently colliding with additional Argon atoms, generating more ions and free electrons in the process, continuing the cycle. The source material is called the target and the emitted atoms or molecules are said to be sputtered off.

One or more linear collision cascades are started at higher energetic ions. Then the density of recoils is low enough so that most collisions involve one moving and one stationary particle, rather two moving particles. The outcome of such processes is sputtering that is the ejection of target atoms.

The average number of atoms ejected from the target per incident ion is called the sputter yield S which varies with the incident angle, the energy of the ion, the masses of the ion and target atoms, and

the surface binding energy of atoms in the target. In the low-energy region near the threshold, S obeys the relation $S \propto E^2$. If the the ion energy is in the order of 100 eV, $S \propto E$. In this energy region, the incident ions collide with the surface atoms of the target, and the number of displaced atoms due to the collision will be proportional to the incident energy. At higher ion energies of 10 to 100 keV, the incident ions travel beneath the surface and the sputter yields are not governed by surface scattering, but by the scattering inside the target. Above 10 keV, The sputter yields will decrease if the ion energy is greater than 10 keV, because of the energy dissipation of the incident ions deep in the target. Maximum sputter yields are observed in the ion energy region of about 10 keV [171].

2.1.2 DC sputtering

Among the different sputtering methods, the simplest model is the dc sputtering. The dc sputtering system is composed of a pair of planar electrodes (cathode and anode). The front surface of the cathode is covered with target materials to be deposited. The substrates are placed on the anode. The sputtering chamber is filled with sputtering gas, typically argon gas at 5 Pa. The electric field accelerates the electrons, which in turn collide with argon atoms,breaking some of them up into argon ions and more electrons to produce the glow discharge The glow discharge is sustained by the applied dc voltage between the electrodes. The Ar^+ ions generated in the glow discharge are accelerated towards the cathode and sputter the target, resulting in the deposition of the thin films on the substrates. When the ions strike the cathode, they may sputter some of the target atoms off. They may

also liberate secondary electrons from the target which are responsible for maintaining the electron supply to sustaining glow discharge. The sputtered atoms from the target fly off in random directions, and some of them land on the substrate, condense there, and form a thin film. In the dc sputtering system, the target is composed of metal since the glow discharge is maintained between the metallic electrodes.

Sputtering pressure and current can modulate the relative film deposition-rate. Low pressures cause wide cathode sheath, hence ions are produced far from the target, and their chances of being lost to the walls is great. Due to the large mean free electron path , electrons collected by the anode are not replenished by ion-impact-induced secondary-electron emission at the cathode. Therefore, ionization efficiencies are low and self sustained discharges cannot be maintained below about 10 $mtorr$. At a constant voltage as the pressure is increased, the electron mean free path is decreased and hence more ions are generated. When the pressure is too high the collisional scattering of the sputtered atoms increased and effective deposition is not possible [172]. The amount of sputtered material deposited on a unit substrate area, W is then given by

$$W \cong \frac{k_1 W_0}{pd} \tag{2.1}$$

the deposition rate R is given by

$$R = \frac{W}{t} \tag{2.2}$$

where k_1 is a constant, W_o is the amount of sputtered particles from the unit cathode area,p is the discharge gas pressure, d is the electrode spacing, W is the density of the sputtered films, and t is the sputter time.

Even though the DC sputtering technique is simple, it is not recommended for commercial application because of the low deposition rates. These rates cannot be considerably increased at higher operating pressures, because of gas scattering and enhanced contaminant levels of O_2 and H_2O in chamber gases, which can oxidize cathodes [171]. Thin insulating layers that developed on the target further reduce the current and deposition rates. Triode sputtering is used to enhance the efficiency of dc sputtering. An assembly of filament cathode and anode is introduced close to the target, parallel to the plane of the target-substrate electrodes. When the filament is heated to high temperatures, thermionic emission and injection of electrons into the plasma enhance the gas-ionization probability and the resulting ions are then pulled out by the negative potential of the target.

2.1.3 Radio frequency sputtering

If we replace the metal target with an insulating target in the dc sputtering discharge system, the sputtering discharge cannot be maintained because of the sudden accumulation of a surface charge of positive ions on the front side of the insulator. To sustain the glow discharge with the insulator target, RF voltage shall be supplied to the target. This system is called rf sputtering. Sputtering in the RF-discharge has been used for the deposition of dielectric thin films in 1960 and a practical RF-sputtering system was developed [174, 175].

When sufficient DC voltage is applied to two metal electrodes of equal area facing one another, a dark space develop at the cathode. Instead of DC, if a low frequency alternating voltage is applied, the system behaves as though it had two cathodes since a dark space is

seen at both electrodes since there is ample time for a DC discharge to become fully established within each cycle. At very high frequency of the applied voltage, electrons oscillate in the RF filed and pick up sufficient energy from the field to cause ionization in the body of the gas. Thus the minimum pressure required to sustain the discharge gradually decreases with the increase of the frequency of applied field. The electron gain energy from the field if it undergoes collisions with gas atoms while it is oscillating so that its ordered simple harmonic motion is changed to a random motion. The electron can increase the random component of its velocity with each collision until it builds up sufficient energy to make an ionizing collision with a gas atom. Since the energy absorbed is proportional to the square of the electric field, electron can continue to gain energy in the field even though it may be moving either with or against it [171, 172].

In RF diode sputtering, the target current density is is given by

$$I_s = C\frac{dV}{dt} \tag{2.3}$$

where C is capacitance between discharge plasma and the target, dv/dt denotes the time variations of the target surface potential. This indicates that the increase of the frequency increases the target ion currents. RF frequency of 13.56 MHz is used in practical systems.

Since the applied RF field appears mainly between the two electrodes, an electron which escapes from the inter-electrode space as a result of a random collision will no longer oscillate in the RF filed and will therefore not acquire sufficient energy to cause ionization. This will be lost to the glow. A magnetic filed, applied parallel to the RF field, will constraint the electron motion and reduces their chance of

being lost. Thus magnetic field is considerably more important for enhancing the RF discharge than it is for the DC case.

The net result is that there is no need to rely on secondary electrons emitted from the cathode to sustain the discharge. Secondly, at radio frequencies, voltage can be coupled through any kind of impedance so that the electrodes need not be conductors. This makes it possible to sputter any material irrespective of its resistivity.

RF sputtering essentially works because the target self-biases to a negative potential (where the electrode areas are unequal). Once this happens, it behaves like a DC target where positive ion-bombardment sputters away atoms for subsequent deposition. Negative target bias is a consequence of the fact that electrons are considerably more mobile than ions and have little difficulty in following the periodic change in the electric field. The disparity in electron and ion mobilities means that isolated positively charged electrodes draw more electron current than comparably isolated negatively charged electrodes draw positive ion current. For this reason the discharge current-voltage characteristics are asymmetric.

The RF sputtering system requires an impedance-matching network between the power supply and discharge chamber.

2.1.4 Reactive sputtering

When a reactive gas species such as oxygen or nitrogen is introduced into the chamber, oxide or nitride thin films are deposited by the sputtering of the metal targets. This type of sputtering is known as reactive sputtering and may be used in either the dc or RF mode. Reactive sputtering is used in practice for the high-rate deposition of

insulating metal oxide films. However, dc sputtering from a metal target is unstable in a standard large-scale dc sputtering operation due to the deposition of an insulating layer on the cathode leading to the buildup of a charge. To reduce the charge-up phenomenon, medium-frequency sputtering with twin targets is used in practice. A medium-frequency power source is connected to the twin targets. The targets act as anode and cathode alternatively at the frequency of several tens of kilohertz, and deposition can be carried out with no appreciable decrease in the deposition rate.

2.1.5 Magnetron sputtering

Low pressure sputtering is one of the most promising techniques for the fabrication of thin film devices. A wide variety of thin films can be deposited with little film contamination and at a high deposition rate by this technique. In 1935 Penning first employed low pressure sputtering in which a transverse magnetic field was superposed on a dc glow discharge tube. The experimental system was composed of coaxial cylindrical electrodes with an axial magnetic field, similar to a cold cathode magnetron. As compared to DC sputtering, one to two orders of magnitude more current is typically drawn in magnetron for the same applied voltage. Hence magnetron sputtering can cause higher deposition rates and another important advantage is low operating pressures. At typical magnetron-sputtering pressures of a few millitorr, sputtered atoms fly off in ballistic manner to impinge on substrates [171].

There are two types of magnetron sputtering systems widely used for thin film growth. One is a cylindrical type, the other is a planar

type. Within the cathode target, permanent magnets are embedded in such way to produce magnetic field of several hundred gauss. The glow discharge is concentrated in the high magnetic field region, thus a circular cathode glow is observed. The surface of the cathode is nonuniform due to the circular cathode glow. This shortens the actual life of the of the cathode target. When magnetic materials are used magnetron sputtering targets have been observed to be of limited use. The magnetic field lines are confined within the target material unless very thin targets are used where magnetic saturation can be attained.

In the magnetron sputtering system the working pressure is 10^{-5} to 10^{-3} Torr, and the sputtered particles traverse the discharge space without collisions. Deposition rate R is given by

$$R \cong \frac{kW_0}{t} \tag{2.4}$$

where k = 1 for the planar system, k = r_e/r_a for the cylindrical system and r_e is the cathode radius and r_a is the anode radius. W_0 is the amount of sputtered particles given [176].

2.1.6 Specifications of sputtering system

A planar magnetron sputtering system is used to carry out the work presented in this thesis (figure 2.1). It consists of a semi cylindrical steel vacuum chamber which houses two 2" magnetron guns (Sierra Applied Sciences, USA) and a substrate holder. There are feed through provisions for supplying the working gas argon and reactive gas oxygen. Gas flow to the chamber is controlled by separate gas flow meters (GFC 17, Aalborg, USA). A circular substrate holder is attached to a programmable stepper motor to rotate it during the

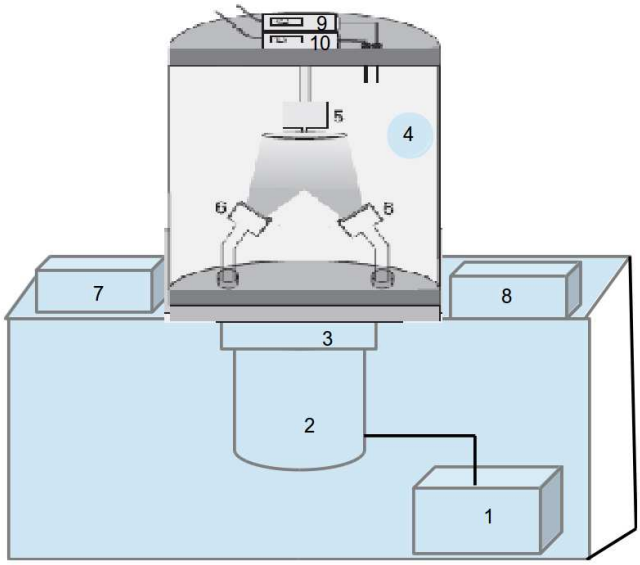

Figure 2.1: Schematic diagram of co-sputtering setup used in the study. (1) Diaphram pump, (2)turbo molecular pump, (3) gate valve, (4) box-type vacuum chamber, (5) stepper motor with substrate holder, (6) magnetron guns, (7&8) RF generators, (9&10) gas flow controllers

deposition.

Base vacuum required for the deposition is created in the chamber using Turbo molecular pump backed by an oil free diaphram pump. Cold water is circulated through the diffusion pump and magnetron guns. For the deposition of multi-component oxide thin films, co-sputtering method is employed. In this technique, two targets are simultaneously sputtered so that an alloy of the materials are formed at the substrate. During co-sputtering, two separate RF generators are used to energize the magnetron guns. We have two RF generators: one with 300 W (PFG 300 RF, Huttinger, Germany) maximum capacity

and another one with 600 W capacity (SERN R 601). Throughout this study, thin film deposition is carried out at room temperature without any intentional substrate heating.

2.1.7 Thermal evaporation by resistive heating

Vacuum thermal evaporation moderately transfer atoms from a heated source to a substrate placed a distance away, where film growth proceed atomistically. Themal evaporation is the most commonly used technique for the preparation of thin films of metals, alloys, and also many compounds. The major requirement is to have a vacuum environment in which sufficient amount of heat is given to the evaporants to attain the vapour pressure necessary for the evaporation. When evaporation is made in vacuum, the evaporation temperature will be considerably reduced and the formation of the oxides and incorporation of impurities in the growing layer will be lowered. Chamber pressure of 10^{-5} Torr is optimum for evaporation, at which a straight line path for most of the emitted vapour atoms is ensured for a substrate to source distance of approximately 10 to 50 cm. The evaporated material is allowed to condense on a substrate kept at a desirable temperature. The characteristics and quality of the deposited film will depend on the substrate temperature, rate of deposition, ambient pressure, etc. and the uniformity of the film depends on the geometry of the evaporation source and its distance from the source. Drawbacks of resistively heated evaporation sources include contamination by crucibles, heaters, and support materials and the limitation of relatively low input power levels. This makes it difficult to deposit pure films or evaporate high-melting-point materials at appreciable rates.

Holland [177] made excellent and detailed review on thermal evaporation technique. The deposition of gold electrodes was done using thermal evaporation via resistive heating in the work presented in this thesis.

2.2 Characterisation techniques

2.2.1 Thin film thickness

Thin film thickness is one of the most significant parameter to be characterized since it plays an important role in the film properties unlike a bulk material. Microelectronic applications usually need the maintenance of precise and reproducible film metrology. Several techniques are available to characterize the film thickness which are basically classified into optical and mechanical methods, and are usually nondestructive but sometimes destructive in nature. Film thickness may be measured either by in-situ monitoring of the rate of deposition or after the film deposition. The stylus profiler takes measurements electromechanically by moving the sample beneath a diamond tipped stylus. The high precision stage moves the sample as per the user defined scan length, speed and stylus force. The stylus is mechanically coupled to the core of a linear variable differential transformer (LVDT). The stylus moves over the sample surface. Surface variations cause the stylus to be translated vertically. Electrical signals corresponding to the stylus movement are produced as the core position of the LVDT changes. The LVDT scales an ac reference signal proportional to the position change, which in turn is conditioned and converted to a digital format through a high precision, integrating,

analog-to-digital converter [178]. The film whose thickness has to be measured is deposited with a region masked. This creates a step on the sample surface. Then the thickness of the sample can be measured accurately by measuring the vertical motion of the stylus over the step. The thicknesses of the thin films deposited for the work presented in this thesis were measured by a stylus profiler (Dektak 6M).

2.2.2 Structural characterisation

Glancing angle x-ray diffraction (GXRD)

The structural characterization was carried out recording the glancing angle x-ray diffraction (GXRD) pattern of the samples using PANalytical X'Pert PRO with Cu-K_α radiation (λ = 1.5418 Å). Glancing angle x-ray diffraction (GXRD) is a nondestructive, surface sensitive technique used to record the diffraction pattern of thin films with minimum contribution from the substrate. In the conventional XRD patterns of thin films deposited on a substrate, the contribution from the substrate to the diffraction can dominate the contribution from the thin film. Conventional x-ray diffraction reveals information about a top layer of a thickness of the order of 5-10 μm. By increasing the path length of the incident x-ray beam through the film, the intensity from the film can be increased. Thin films as thin as 100 $\mathring{A}$ can be analysed by using a grazing incidence angle arrangement along with a parallel beam geometry. This technique is based on the fact that, for high energy x-rays, the refractive index of material is slightly less than unity, as a result of which material is less refractive (for x-rays)than it is for vacuum. Hence it is possible to have total external reflection from a surface if the angle of incidence is small enough (typically 1-25

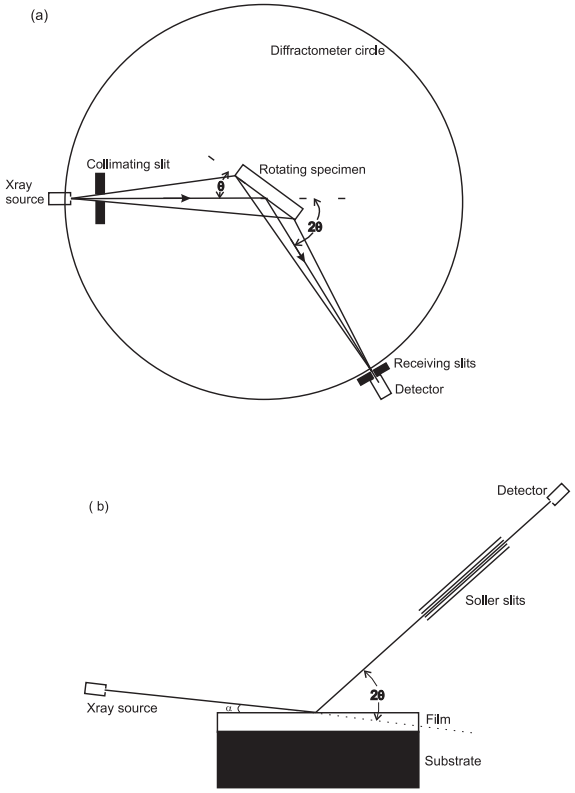

Figure 2.2: Geometries of (a) conventional and (b) glancing angle XRD.

milliradians or 0.05-1.5^o), depending on the substrate electron density and the x-ray energy. At this point the substrate is not completely invisible to x-rays, but only an evanescent wave penetrates into and scatters from it. The x-ray intensity is therefore maximum at the surface [179].

In the conventional $\theta/2\theta$ geometry, a parafocusing arrangement is employed where the x-ray source and the detector slit are at the focal points of the incident and diffracted beams, respectively. For GXRD,

the incident and diffracted beams are made nearly parallel by means of a narrow slit on the incident beam and a long Soller slit on the detector side. In addition, the stationary incident beam makes a very small angle with the sample surface, which increases the path length of the x-ray beam through the film. This helps to increase the diffracted intensity, while at the same time, reduces the diffracted intensity from the substrate. Overall, there is a dramatic increase in the film signal to the background ratio. Since the path length increases when the grazing incidence angle is used, the diffracting volume increases proportionally which subsequently gives increased signal strength. During the collection of the diffraction spectrum, only the detector rotates through the angular range, thus keeping the incident angle, the beam path length, and the irradiated area constant. The long soller slit on the receiving side allows only those beams that are nearly parallel to arrive at the detector. This has an additional benefit of decreasing sensitivity to sample displacement from the rotation axis.

2.2.3 Transmission electron microscopy (TEM)

Transmission electron microscopy (TEM) is an imaging technique whereby a beam of electrons is focused onto a specimen causing an enlarged version to appear on a fluorescent screen or on a photographic film or to be detected by a CCD camera. The first practical transmission electron microscope was built by Albert Prebus and James Hillier at the University of Torondo in 1938 using concepts developed earlier by Max Knoll and Ernst Ruska. Electrons are generated by a process known as thermionic discharge in the same manner as the cathode in a cathode ray tube, or by field emission; they are then accelerated by

an electric field and focused by electrical and magnetic fields onto the sample. The electrons can be focused onto the sample providing a resolution far better than that possible with light microscopes, with improved depth of vision. Details of a sample can be enhanced in light microscopy by the use of stains. Similarly with electron microscopy, compounds of heavy metals such as osmium, lead or uranium can be used to selectively deposit on the sample to enhance structural details. The electrons that remain in the beam can be detected using a photographic film, or fluorescent screen [180]. So areas where electrons are scattered appear dark on the screen, or on a positive image.

Transmission electron microscopy is a straight forward technique to determine the size and shape of the nanostructured materials as well as to obtain structural information. In TEM, electrons accelerated to 100 keV or higher, are projected on to a thin specimen by means of a condenser lens system, and they penetrate in to the sample [181]. TEM uses transmitted and diffracted electrons which generates a two dimensional projection of the sample. The principal contrast in this projection or image is provided by diffracted electrons. In bright field images, the transmitted electrons generate bright regions while the diffracted electrons produce dark regions. In dark field image, the diffracted electrons preferentially form the image. In TEM, one can switch between imaging the sample and viewing its diffraction pattern by changing the strength of the intermediate lens. The greatest advantage that TEM offers are the high magnification ranging from 50 to 10^6 and its ability to provide both image and diffraction information of the same sample. The high magnification or resolution of TEM is given by

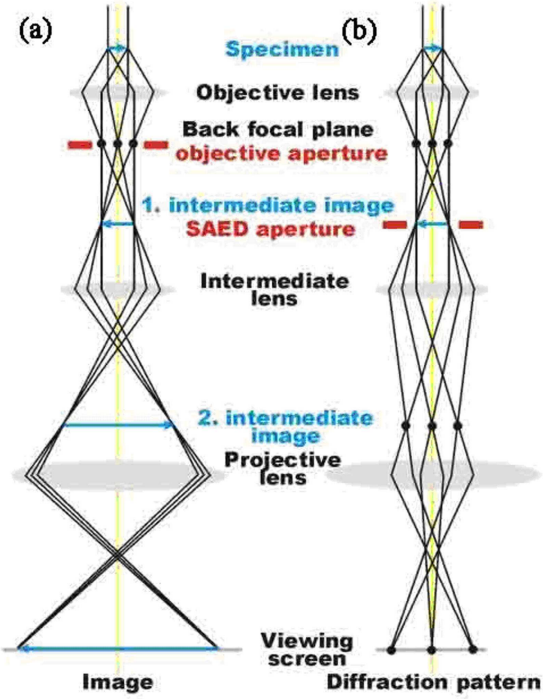

Figure 2.3: Transmission electron microscope for imaging and selected area electron diffraction pattern

$$L = \frac{h}{\sqrt{2mqV}} \tag{2.5}$$

where m and q are the electron mass and charge, h the Planck's constant and V is the potential difference through which the electrons are accelerated. The schematic of a transmission electron microscope is shown in figure 2.3.

Typically a TEM consists of three stages of lensing. The stages are the objective lenses, intermediate lenses and the projector lenses. The objective lens forms a diffraction pattern in the back focal plane

with electrons scattered by the sample and combines them to generate an image in the image plane (intermediate image). Thus diffraction pattern and image are simultaneously present in the TEM. It depends on the intermediate lens which appears in the plane of the second intermediate image and magnified by the projective lens on the viewing screen. Switching from a real space to a reciprocal space (diffraction pattern) is easily achieved by changing the strength of the intermediate lens. In imaging mode, an objective aperture can be inserted in the back focal plane to select one or more beams that contribute to the final image (Bright field (BF), Dark field (DF), High Resolution TEM (HRTEM)). The BF image is formed by effectively cutting out all the diffracted beams, leaving out only transmitted beam to form the image. The bright field image is bright only in areas that have crystalline planes that are tilted such that they do not satisfy the Bragg condition. The DF image will be obtained on the other hand if the transmitted beams are blocked instead of diffracted beams. TEM, JEOL operating at an accelerating voltage of 200 kV was used in the present work.

2.2.4 Raman spectroscopy

The Raman effect occurs when light impinges upon a molecule and interacts with the electron cloud and the bonds of that molecule. For the spontaneous Raman effect, which is a form of scattering, a photon excites the molecule from the ground state to a virtual energy state. When the molecule relaxes it emits a photon and it returns to a different rotational or vibrational state. The difference in energy between the original state and this new state leads to a shift in the emitted

photon's frequency away from the excitation wavelength.

If the final vibrational state of the molecule have more energy than the initial state, then the emitted photon will be shifted to a lower frequency in order for the total energy of the system to remain balanced. This shift in frequency is referred to Stokes shift. If the final vibrational state is less energetic than the initial state, then the emitted photon will be shifted to a higher frequency and this is designated as an Anti-Stokes shift. Raman scattering is an example of inelastic scattering because of the energy transfer between the photons and the molecules during their interaction. A change in the molecular polarization potential or amount of deformation of the electron cloud with respect to the vibrational coordinate is required for a molecule to exhibit a Raman effect. The amount of the polarizability change will determine the Raman scattering intensity. The pattern of shifted frequencies is determined by the rotational and vibrational states of the sample.Typically, a sample is illuminated with a laser beam. Light from the illuminated spot is collected with a lens and sent through a monochromator. Wavelengths close to the laser line, due to elastic Rayleigh scattering, are filtered out while the rest of the collected light is dispersed onto a detector. The Raman effect, which is a light scattering phenomenon, should not be confused with absorption (as with fluorescence) where the molecule is excited to a discrete (not virtual) energy level.

Spontaneous Raman scattering is typically very weak, and as a result the main difficulty of Raman spectroscopy is separating the weak inelastically scattered light from the intense Rayleigh scattered laser light. Historically, Raman spectrometers used holographic gratings and multiple dispersion stages to achieve a high degree of laser re-

jection. In the past, photomultipliers were the detectors of choice for dispersive Raman setups, which resulted in long acquisition times. However, modern instrumentation almost universally employs notch or edge filters for laser rejection and spectrographs (either axial transmissive (AT), Czerny-Turner (CT) monochromator) or FT (Fourier transform spectroscopy based) and CCD detectors.

The information about structure, phase, grain size, phonon confinement etc can be obtained from Raman spectroscopy. The extend of phonon confinement in a material can be observed as the shift in Raman line frequencies. Acoustic modes are not observed by Raman measurements in bulk systems because of their low frequencies. But in nanostructured materials, they appear in the measurable frequency range (below 100 cm^{-1}) [183, 185]. Confinement of optical phonons results in the frequency shift and asymmetrical broadening of longitudinal optical (LO) and transverse optical (TO) mode line shape [184]. The information about the structure and quality of the low dimensional structures can be obtained from Raman spectroscopy.

In the present work, Raman studies were carried out with Lab RAM HR spectrophotometer (HORIBA JOBIN YVON) with Ar ion laser (514.5 nm) as the excitation source.

2.2.5 Surface morphology

Surface morphology is an important property while studying nanostructures. Characterization tools used to study the surface morphology of the nanostructures is described below.

i) Atomic force microscopy

After the invention of the scanning tunneling microscope (STM), a number of new scanning probe microscopes (SPM) has been developed that use the key components of the STM. One of the most significant SPM is the atomic force microscope (AFM) [182]. In atomic force microscopy a tip, integrated to the end of a spring cantilever, is brought within the inter-atomic separations of a surface, such that the atoms of the tip and the surface are influenced by interatomic potentials (figure 2.4). As the tip is rastered across the surface, it bounces up and down with the contours of the surface. By measuring the displacement of the tip (i.e. the deflection of the cantilever), one can theoretically map out the surface topography with atomic resolution.

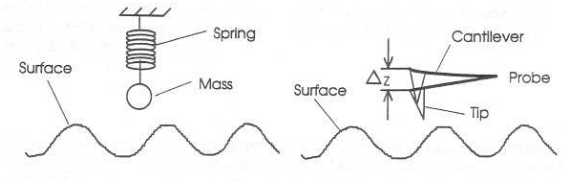

Figure 2.4: Shows how the tip is attached to the cantilever.

Initially cantilever deflections of AFM were measured using a piggy-backed STM. Later instruments used more practical optical techniques. The AFM have similar concept of scanning profilometer, except that the deflection-sensitivity and resolution are improved by several orders of magnitude. There are a plenty of applications for the AFM, including biological systems, polymers and a host of insulator and semiconductor materials.

An AFM images a surface in a manner analogous to the gramophone stylus sensing the groves of gramophone disk. The essential

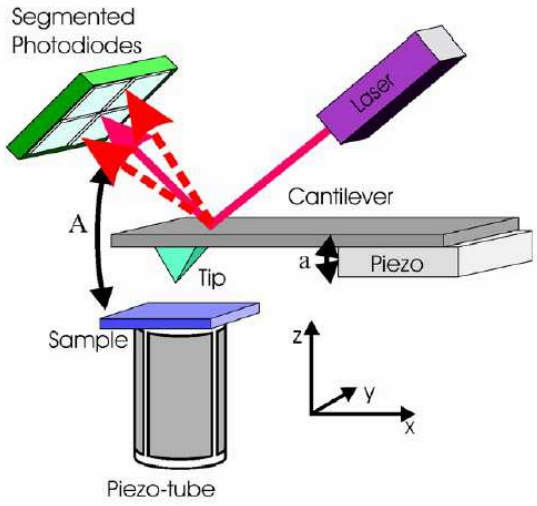

Figure 2.5: The essential elements of an AFM.

components of an AFM are shown in the figure 2.5. The tip is attached to a cantilever type spring as the tip and sample interact, forces act on the tip and cause the cantilever to deflect. The cantilever position is tracked by a position detector. The output of the detector is connected to a feedback controller that modulate the force between the sample and the tip by moving the sample up or down. The sample is moved by a PZT scanning actuator. The cantilever must be soft enough to deflect a measurable amount without damaging the surface features of the sample. The amount of deflection is proportional to the force acting on the tip.

Variations of AFM include contact mode, dynamic force mode, phase mode, current image, friction force microscope, magnetic force microscope, surface potential microscope, etc. In the present work, Agilent 5500 series AFM was used for the morphological study.

1. **Contact mode:** Contact mode is the most widely used method in which the tip scans the sample and force on the tip is repulsive with a mean value of 10^{-9} N. This force is set by pushing the cantilever against the sample surface with a piezoelectric positioning element. In contact mode AFM the deflection of the cantilever is sensed and compared in a DC feedback amplifier to some desired value of deflection. If the measured deflection is different from the desired value the feedback amplifier applies a voltage to the piezo to raise or lower the sample relative to the cantilever to restore the desired value of deflection. The voltage that the feedback amplifier applies to the piezo is a measure of the height of features on the sample surface. The typical problem with the contact mode is that the tip may scratch the surface and change its intrinsic features

2. **Non-contact mode:** In this mode the tip is held at 50 - 150 Å above the sample surface. Attractive Van der Waals forces acting between the tip and the sample are detected, and topographic images are constructed by scanning the tip above the surface. Since the attractive forces from the sample are substantially weaker than the forces used by contact mode therefore the tip is given a small oscillation so that AC detection methods can be used to detect the small forces between the tip and the sample by measuring the change in amplitude, phase, or frequency of the oscillating cantilever in response to force gradients from the sample. For highest resolution, it is necessary to measure force gradients from Van der Waals forces which may extend only a nanometer from the sample surface.

3. **Semi-contact mode:** Semi-contact mode was developed as a method to achieve high resolution without including destructive frictional forces both in air and liquid. In this mode, the cantilever is made to oscillate at its natural frequency by using a piezo-electric crystal. The oscillating tip is moved close to the sample surface till it begins to just tap it and is then immediately lifted off again, while the sample is continuously scanned below the tip. The change in oscillation amplitude during the tapping period is used as a feedback to maintain constant height or force between the tip and the sample. The feedback voltage serves as a measure of the surface features. The advantages of the semi-contact mode are that as the tip is not dragged over the sample there is no damage caused to the sample and also the tip is prevented from sticking to the sample surface due to adhesion. This method usually gives higher resolution than the previous two methods. With the semi contact mode, the very soft and fragile samples can be imaged successfully.

2.2.6 Compositional analysis

i) X-ray photoelectron spectroscopy (XPS)

X-ray photoelectron spectroscopy (XPS) is a quantitative spectroscopic technique that measures the elemental composition, empirical formula, chemical state and electronic state of the elements that exist within a material. XPS spectra are obtained by irradiating a material with a beam of x-rays while simultaneously measuring the kinetic energy and number of electrons that escape from the top 1 to 10 nm of the material being analyzed (figure 2.6). XPS requires ultra-high

vacuum (UHV) conditions.

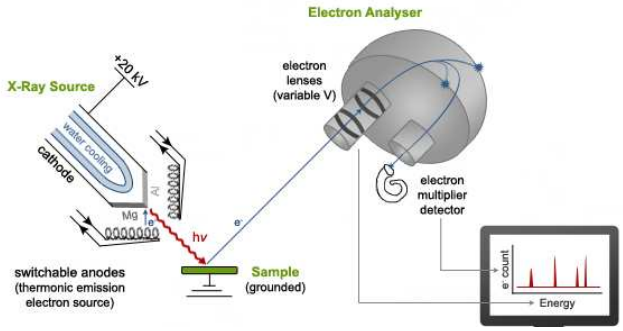

Figure 2.6: Schematic diagram of X-ray photoelectron spectrometer

XPS is a surface chemical analysis technique that can be used to analyze the surface chemistry of a material in its "as received "state, or after some treatment, for example: fracturing, cutting or scraping in air or UHV to expose the bulk chemistry, ion beam etching to clean off some of the surface contamination, exposure to heat to study the changes due to heating, exposure to reactive gases or solutions, exposure to ion beam implant, exposure to ultraviolet light. The main features of the XPS are

1. XPS detects all elements with an atomic number (Z) of 3 (lithium) and above.

2. Detection limits for most of the elements are in the parts per thousand range.

3. XPS is routinely used to analyze inorganic compounds, metal alloys, semiconductors, polymers, elements, catalysts, glasses, ceramics.

4. Uniformity of elemental composition across the top surface (or line profiling or mapping).

In the present study XPS spectrum is recorded by Kratos Analytical AMICUS spectrometer fitted with the Mg Kα /Al Kα dual anode x-ray source.

2.2.7 Focused ion beam (FIB)

Focused ion beam (FIB), is a technique used especially in the semiconductor and materials science for site-specific analysis, deposition, and ablation of materials. An FIB setup is a scientific instrument that is similar to a scanning electron microscope(SEM). Basic difference between SEM and FIB is that SEM uses a focused beam of electrons to image the sample in the chamber where FIB setup make use of a focused beam of ions. FIB can also be integrated in a system with both electron and ion beam columns, allowing the same feature to be investigated using either of the beams.

liquid-metal ion sources (LMIS), especially gallium ion sources are most commonly used as ion source in FIB. Ion sources based on elemental gold and iridium are also usable. In a gallium LMIS, gallium metal is made contact with a tungsten needle and heated gallium wets the tungsten and moves to the tip of the needle where the opposing forces of surface tension and electric field form the gallium into a cusp shaped tip called a Taylor cone. The tip radius of this cone is very small ($\sim$ 2 nm). The large electric field at this small tip (greater than 1 x 10^8 volts per centimeter) produces ionization and field emission of the gallium atoms. Source ions are accelerated to an energy of 1-50 keV (kiloelectronvolts), and directed to the sample by electrostatic

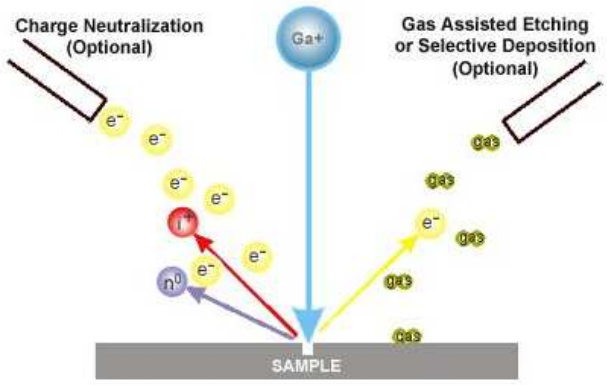

Figure 2.7: The principle of FIB

lenses. LMIS generate high current density ion beams with very small energy spread. A modern FIB can provide tens of nanoamperes of current to a sample, or can image the sample with a spot size on the order of a few nanometers. As shown in the figure 2.7 gallium (Ga^+) primary ion beam strike the sample surface and sputters a little amount of material, which leaves the surface as either secondary ions or neutral atoms. The primary beam also generates secondary electrons (e^-). As the primary beam rasters on the sample surface, the signal from the sputtered ions or secondary electrons is collected to develop an image. In the present study the cross sectional analysis of the TFT was performed using Carl Zeiss Neon 40 FIB/SEM.

2.2.8 Hall effect measurement

The Hall effect measurement technique is most widely used for the characterisation of semiconductor materials as it gives the resistivity,

the carrier density, type of carriers and the mobility of carriers.The magnetic field applied to a conductor perpendicular to the current flow direction, can develop an electric field at perpendicular to the direction of magnetic field and the current (figure 2.8). This phenomenon is known as Hall effect and the voltage developed is called Hall voltage. For a charge charge (q) moving with a velocity v in the presence of an

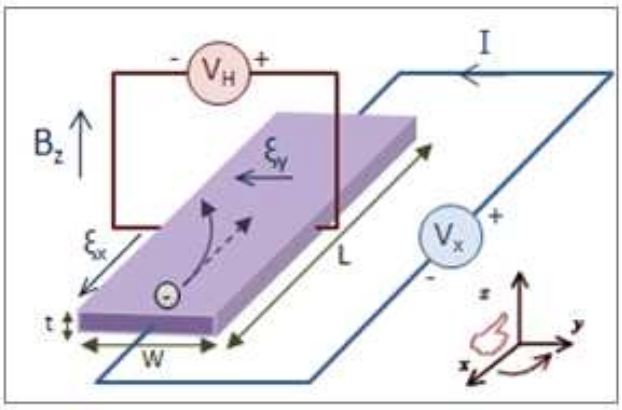

Figure 2.8: Hall effect measurement set up

electric (E) and magnetic (B) fields, the force experienced is given by the vector expression

$$\overrightarrow{F} = q(\overrightarrow{E} + \overrightarrow{v} \times \overrightarrow{B}) \tag{2.6}$$

electrons in n-type and holes in p-type samples deflect to the same side of the sample for the same current direction because electrons flow in the opposite direction to holes and have opposite charge.

The Hall coefficient R_H is defined as

$$R_H = \frac{V_H d}{BI} \tag{2.7}$$

where d is the sample dimension in the direction of magnetic field B, V_H is the Hall voltage and I is the current through the sample [182]. Hall coefficient is related to hole (p) and electron (n) densities by the equation:

$$p = \frac{1}{qR_H};\ and\ n = -\frac{1}{qR_H} \tag{2.8}$$

Equation 2.8 is derived under the assumption of energy independent scattering mechanisms. With this assumption relaxed, the expressions for the hole and electron densities can be written as

$$p = \frac{r}{qR_H};\ and\ n = -\frac{r}{qR_H} \tag{2.9}$$

where r is the Hall scattering factor, defined by $r = \langle\tau^2\rangle/\langle\tau\rangle^2$, with τ being the mean time between carrier collisions. The scattering factor depends on the type of scattering mechanism in the semiconductor and generally lies between 1 and 2. For lattice scattering, $r = 1.18$, for impurity scattering $r = 1.93$, and for neutral impurity scattering $r = 1$. The scattering factor is depending on magnetic field and temperature and can be determined by measuring R_H in the high magnetic field limit, i.e.,

$$r = \frac{R_H(B)}{R_H(B = \infty)} \tag{2.10}$$

In the high field limit $r \to 1$.

Sample geometries for van der Pauw resistivity and Hall effect measurements is shown in the figure 2.9. The cloverleaf design will have the least error due to its smaller effective contact size, but it is more difficult to fabricate than a square or rectangle.

For semiconducting films on insulating substrates, the mobility is frequently found to decrease toward the substrate. Surface depletion

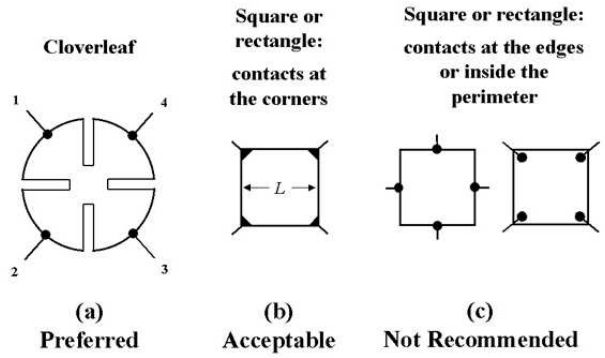

Figure 2.9: Sample geometries for Hall effect measurement

forces the current to flow in the low-mobility portion of the film, giving apparent mobilities lower than true mobilities. Hall effect measurements are simple to interpret for uniformly doped samples. Nonuniformly doped layer measurements are more difficult to interpret. If the doping density varies with film thickness, then its resistivity and mobility also vary with thickness. A Hall effect measurement gives the average resistivity, carrier density, and mobility.

Electrical resistivity and Hall coefficients of the films described in this thesis were measured by four probe van der Pauw configuration at room temperature using using Ecopia, HMS-3000.

2.2.9 Optical characterisation

Optical absorption coefficients of thin films can be determined from optical transmission or absorption measurements. During transmission measurements light is incident on the sample and the transmitted

light is measured as a function of wavelength.The band gap of a semiconductor is measured by studying the absorption of incident photons by the material. Here the photons of selected energy are directed to the sample and the relative transmission of the various photons is observed. Since photons with energies greater than the band gap energy are absorbed while photons with energies less than band gap energy are transmitted, the experiment gives an accurate measure of band gap. As per equation 1.24, the optical bandgap (Tauc gap) of amorphous films are determined by plotting $(\alpha h\nu)^{0.5}$ versus $h\nu$ and taking the intercept to energy axis. For crystaline films, bandgap can be estimated from a plot of $(\alpha h\nu)^2$ versus $h\nu$.

Swanepoel has shown that the optical properties of a uniform thin film of thickness t, refractive index n, and absorption coefficient α, deposited on a substrate with a refractive index s can be obtained from the transmittance given by

$$T = \frac{Ax}{B - Cxcos\phi + Dx^2} \tag{2.11}$$

where A = $16n^2s$, B = $(n+1)^3(n+s^2)$, C = $2(n^2-1)$ (n^2-s^2),
D= $(n^2-1)^3(n-s^2)$.

Transmission spectra of the thin films were recorded using Jasco V-570, UV-vis-NIR spectrophotometer.

2.2.10 Thin film transistor structures

Depending on the electrode positions, TFT structure may be classified in to four: Co-planar top-gate, co-planar bottom gate, staggered top-gate, and staggered bottom-gate(figure 2.9). In a coplanar configuration, The source and drain contacts and the insulator are on

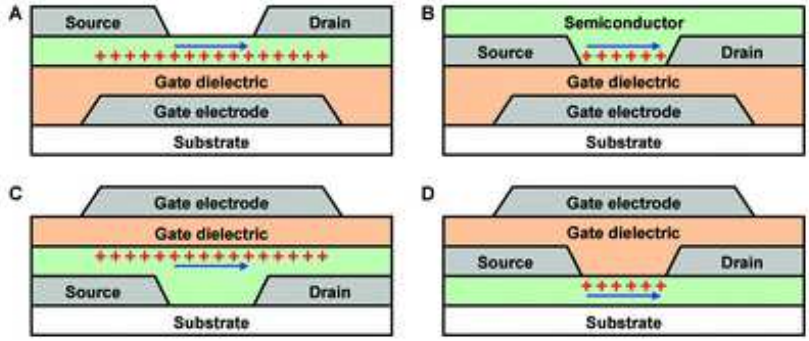

Figure 2.10: Schematic cross-sections of the four principle TFT structures. (a) Bottom-gate (inverted) staggered TFT. (b) Bottom-gate (inverted) coplanar TFT. (c) Top-gate staggered TFT. (d) Top-gate coplanar TFT.

the same side of the channel in coplanar configuration.The source and drain contacts are on opposite sides of the channel from the insulator in staggered configuration. Both the staggered and the coplanar configurations are again classified categorized as bottom-gate and top-gate structures.

For the fabrication of TFT, among the different layers of the device, insulator layer deposition need the use of a higher power for evaporation or sputtering. Semiconductor channel layer is deposited first in the coplanar top-gate structure. Here the maximum semiconductor processing temperature is determined by the semiconductor and the substrate because the high power deposition of insulator layer may damage the channel-insulator interface. Insulator layer is deposited before the channel layer deposition, in bottom-gate structures. Each of the four TFT structures has certain merits and demerits. For example, the presence of an energy barrier at the interfaces between the semiconductor and the source and drain contacts is expected to

impede the exchange of charge carriers between the contacts and the semiconductor Experiments and simulations have proved that for the same energy barrier height, TFTs with a staggered structure (A, C) have the advantage of being less affected by this energy barrier than TFTs with a coplanar structure (B,D) [186]. The inverted-staggered structure is most commonly used in the manufacturing of LCD panels. This structure is significant because of its simplicity of fabrication and the availability of a high-quality substrate-gate-insulator stack that necessitates the use of a bottom-gate structure. One of the main disadvantage of this approach is the exposure of the semiconducting channel to atmosphere. Exposure to atmosphere can degrade of the electrical properties of the TFT, such as the formation of a surface accumulation layer. A surface accumulation layer can provide a conduction path in parallel with the insulator-semiconductor accumulation layer associated with ideal square-law current-voltage behaviour.

2.2.11 Basic device operation

Field effect in semiconductor physics physics refers to the modulation of the electrical conductivity of a material by the application of an external electric field normal to the surface of the semiconductor. The working principle of a TFT is similar to that of a MOSFET. The operation of a p-type TFT (p-TFT) can be described based on the following : the semiconductor is p-type with work function less than that of the metal contact, there is no charge present in the insulator, the TFT structure is inverted-staggered, and the surface/atmosphere interface has no effect on the energy bands.

Consider the case when the p-TFT is in equilibrium, with V_{GS}

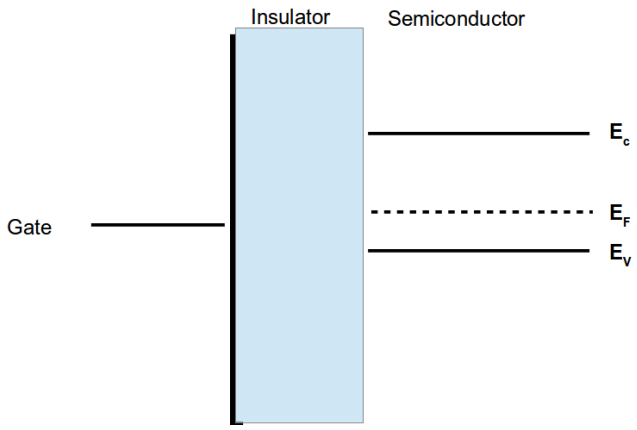

Figure 2.11: An energy band diagram for a p-type TFT before gate biasing

=0 V, where V_{GS} is the terminal voltage applied from gate-to-source. Figure 2.11 shows the energy bands in the cross-section from gate to semiconductor to the exposed semiconductor surface. When no bias is applied, the Fermi level is constant across the device. For positive gate voltage, the majority carrier holes are pushed back from the semiconductor surface, thereby leaving it depleted of free carriers. For an ideal p-TFT in this biasing regime, a negligible amount of current flows from drain-to-source. In a real TFT, the dominant current mechanisms in this regime are leakage current through the insulator, I_G, and source/drain leakage current.

Figure 2.12 shows the p-TFT when $V_{GS} < 0$ V, i.e., under an accumulation condition. When a negative gate-voltage is applied, majority carrier holes in the semiconductor are attracted and thus accumulated at the insulator/semiconductor interface. The accumulation layer provides a low-resistance conduction path for holes to traverse the semiconductor from source-to-drain. A negative bias applied from

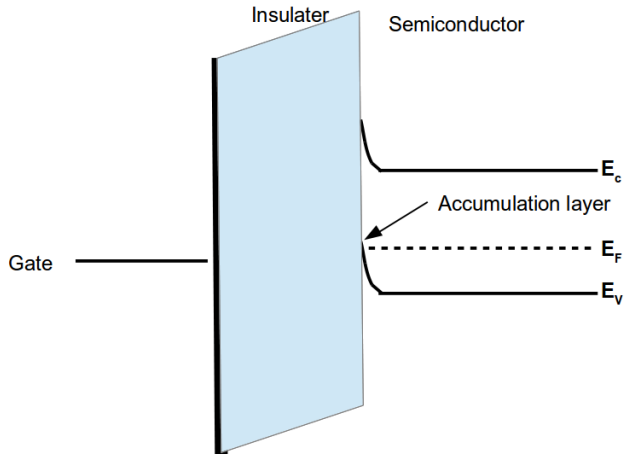

Figure 2.12: An energy band diagram for a p-type TFT under an accumulation condition, i.e. V_{GS} = -ve. At the insulator/semiconductor interface, the valence band is very close to the quasi-Fermi level, implying a high density of holes at that location.

the drain electrode to the source electrode (V_{DS}) results in an electric field which facilitates hole movement from source to drain. As a larger V_{DS} voltage is applied, the current increases proportionally until the channel near the drain pinches off and saturation occurs. Before saturation occurs, the accumulation channel extends continuously from the source to the drain. As the drain-to-source voltage is decreased more negatively, the change in potential from gate to drain causes carriers to be extracted from the channel [6]. This results in pinch-off of the channel in which a depletion, or extraction region is formed at the drain. A consequence of pinch-off and the formation of the extraction region is that the current-voltage characteristics saturate because as a more negative V_{DS} is applied, the extraction region at the drain grows further, and more of the V_{DS} voltage is dropped across the ex-

traction region instead of the channel. The point at which the current saturates is known as the pinch-off voltage, given as $V_{SAT} = V_{GS} - V_T$.

The gate voltage at which there is an appreciable carrier density present at the interface establishes the threshold voltage (i.e. $V_{GS} = V_T$). Now that channel formation has been established, application of a negative voltage on the drain attracts electrons towards the drain and accounts for the drain current, I_D (Figures 2.13 a & b). Initially, the drain current increases linearly with drain-source voltage V_{DS} (Figures 2.13 c & f). As the drain voltage increases, the width of the depletion region near the drain also increases. The voltage at which the channel region near the drain is depleted of carriers, negating the effect of the surface accumulation layer, is the pinch-off voltage V_P or the saturation voltage V_{sat} (Figures 2.13 d & g). Further increase in V_{GS} confines the channel more towards the source side and drain current remains constant if the change in channel length is small compared to the channel length (Figures 2.13 e & h).

TFTs can be operated in enhancement mode or depletion mode depending on whether it require a gate voltage to induce the channel conduction. An enhancement mode device does not conduct at zero gate voltage and requires an applied gate voltage (negative gate voltage in the case of a p-TFT), to induce a conductive channel.In an enhanced mode of operation, the channel conductance is low in the absence of an applied gate voltage. Hence a low carrier density in the channel is essential to achieve this mode. If a gate bias voltage is required to deplete the channel of carriers, then it is called as depletion mode. Hence a depletion mode TFT consumes power even in its off state. For low power displays, the primary interest is in TFT devices

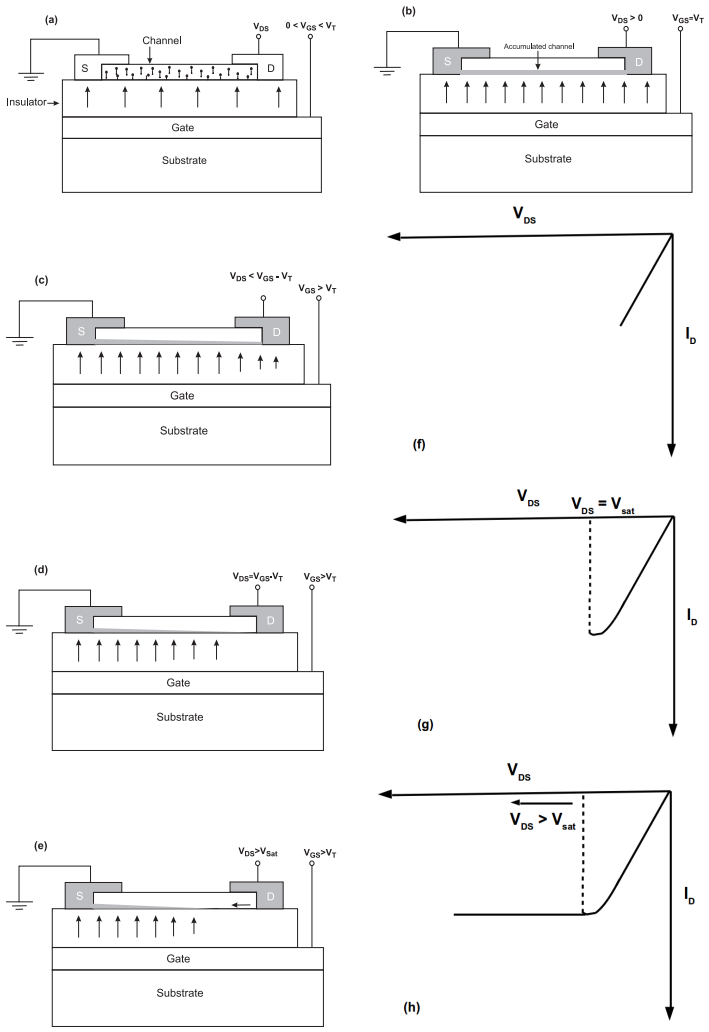

Figure 2.13: Schematic illustration of working of a p-channel TFT. (a)Holes are attracted by the applied electric filed when $0 < V_{GS} < V_T$. (b) Channel formation at $V_{GS} = V_T$. Figures (c-e) show the variation in accumulated charge density with respect to the increase in V_{DS} (near the drain terminal, charge density becomes zero) for a fixed gate voltage $V_{GS} > V_T$. Figures (f-g) show corresponding variations in drain current

that operate in enhancement mode exhibiting a normally off channel state.

2.2.12 Thin film transistor characterisation

Mobility and threshold voltage

As in the case of MOSFET the electrical characterization of TFT include the measurement of transistor output characteristics and transfer characteristics . TFT performance parameters like threshold voltage (V_T), subthreshold voltage swing (S), field effect mobility (μ_{fe}), saturation mobility (μ_{sat}) etc are then derived from these characteristics. The ideal TFT drain current characteristics are similar to those of the MOSFET. Hence the drain current can be expressed by the relations:

$$I_D = \mu C_i \frac{W}{L}\left[(V_{GS} - V_T)V_{DS} - \frac{V_{DS}^2}{2}\right], \text{ for } V_{DS} \leq V_{GS} - V_T \quad (2.12)$$

and

$$I_D = \frac{1}{2}\mu C_i \frac{W}{L}(V_{GS} - V_T)^2, \text{ for } V_{DS} \geq V_{GS} - V_T \quad (2.13)$$

where μ is the average mobility of the carriers in the channel, C_i is the insulator capacitance, W is the channel width, L is the channel length, V_{GS} is the gate-source voltage, V_{DS} is the drain-source voltage and V_T is the threshold voltage.

The mobility and threshold voltage are the most important device performance parameters and can be estimated in three different ways. For TFTs, operating in the linear region ($V_{DS} << V_{GS} - V_T$), equation 2.12 can be written as:

$$I_D \approx \mu C_i \frac{W}{L}(V_{GS} - V_T)V_{DS} \quad (2.14)$$

The mobility and threshold voltage can be estimated from this expression using either the linear region drain conductance

$$g_d \equiv \frac{dI_D}{dV_{DS}}|_{V_{GS}=constant} = \mu C_i \frac{W}{L}(V_{GS} - V_T) \tag{2.15}$$

or the linear region transconductance

$$g_m \equiv \frac{dI_D}{dV_{GS}}|_{V_{DS}=constant} = \mu C_i \frac{W}{L} V_{DS} \tag{2.16}$$

The mobility obtained from the linear region drain conductance is referred to as the effective mobility, μ_{eff}. The effective mobility and threshold voltage is then graphically estimated by plotting linear region drain conductance versus V_{GS}. For V_{GS}-V_T >>V_{DS}, this should become linear; the slope of which gives the effective mobility and the x-intercept gives the threshold voltage V_T. The μ_{eff} and V_T can also be estimated numerically from the equation 2.15. The mobility obtained from the linear region drain transconductance is referred to as the field effect mobility, μ_{fe}. For a small constant value of V_{DS}, a plot of I_{DS} as a function of V_{GS} would yield a straight line, the slope of which is proportional to μ_{fe} and the x-intercept gives V_T (Figure 2.14). That is,

$$\mu_{fe} = \frac{slope}{C_i(W/L)V_{DS}} \tag{2.17}$$

By numerical method, the μ_{fe} and V_T is calculated from equation 2.16 as:

$$\mu_{fe} = \frac{g_m}{C_i(W/L)V_{DS}} \tag{2.18}$$

and

$$V_T = V_{GS} - \frac{I_D}{\mu_{fe} C_i(W/L)V_{DS}} \tag{2.19}$$

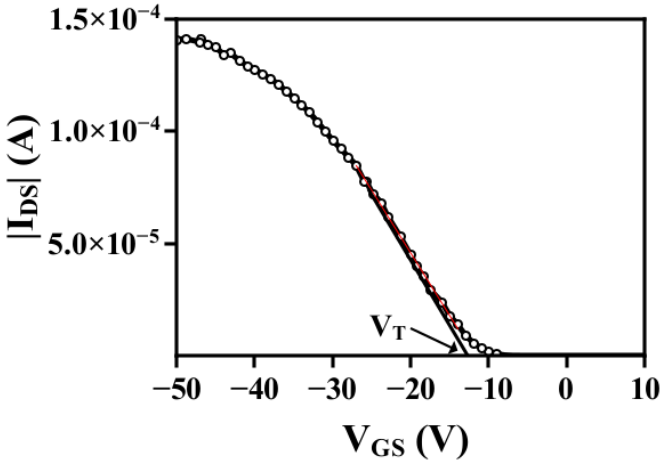

Figure 2.14: Determination of field-effect mobility and threshold voltage from the linear region of device operation.

The mobility and threshold voltage can also be derrived from the saturation region (V_{DS} >V_{GS}-V_T) of transistor characteristics. Corresponding mobility is called saturation mobility μ_{sat}. The expression for I_D, in this region is given by equation 2.13. μ_{sat} and V_T are obtained by plotting $\sqrt{I_D}$ as a function of V_{GS}. For $V_{GS} > V_T$, this plot would become linear and the slope of the linear part is proportional to μ_{sat} and the x-intercept gives V_T (Figure 2.15). That is,

$$\mu_{sat} = \frac{slope^2}{1/2C_i(W/L)} \tag{2.20}$$

Numerically,

$$\mu_{sat} = \frac{\left(d\sqrt{(I_D)}/dV_{GS}\right)^2}{1/2C_i(W/L)} \tag{2.21}$$

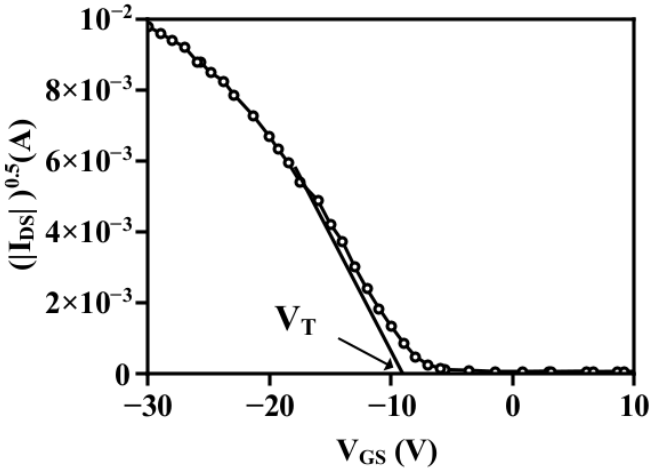

Figure 2.15: Determination of saturation mobility and threshold voltage from the saturation region of device operation.

and

$$V_T = V_{GS} - \sqrt{\frac{I_D}{1/2C_i(W/L)}} \tag{2.22}$$

which is valid for $V_{GS} > V_T$ such that the assumption of saturation region operation is satisfied.

On-off current ratio

On-off ratio is another important TFT performance parameter. It is the ratio of the maximum drain current at above threshold region to the drain current when the device is in off condition (figure 2.16). For higher resolution displays, TFTs are required to have a sufficiently large on current to drive imaging pixels and a small off current to minimize power consumption, which consequently requires large on-off current ratio.

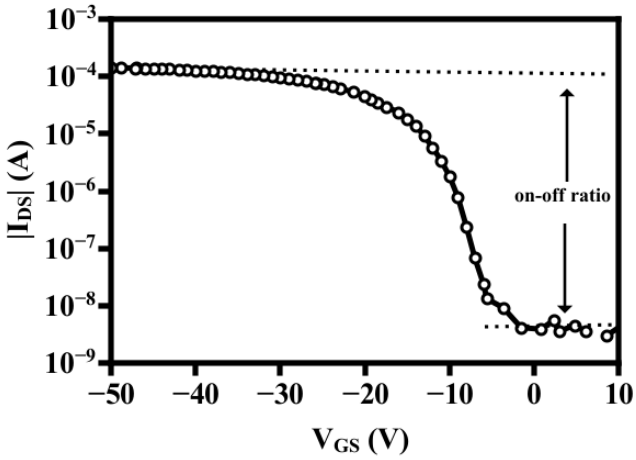

Figure 2.16: Typical transfer characteristics for p-channel TFTs.

Subthreshold slope analysis

Subthreshold conduction is typically derrived from the inverse subthreshold slope (S) which given by the equation:

$$S = \left(\frac{dlog(I_D)}{dV_{GS}} \right)^{-1} \tag{2.23}$$

Subthreshold swing S characterizes the effectiveness of the gate voltage in reducing the drain current to zero. Desirable value of S is very small since this corresponds to a very sharp transition from on to off state (Figure 2.17). The large S values indicates a larger density of tail states (D_{it}) because the S value is related to D_{it} by the equation [187]

$$S = \frac{2.3 k_B T}{e} \left(1 + \frac{e D_{it}}{C_i} \right) \tag{2.24}$$

where k_B is Boltzmann's constant and C_i is the gate insulator capacitance).

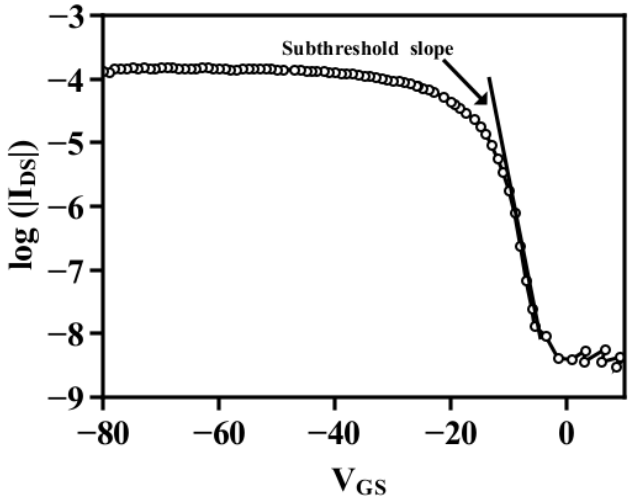

Figure 2.17: $log(I_D) - V_{GS}$ characteristics for subthreshold slope analysis.

In the present work, electrical characterizations of the TFTs were performed using Keithley 4200 semiconductor characterization system.

2.3 Conclusion

Thin film deposition techniques and thin film characterisation methods that were used in the present investigation was briefly explained in this chapter. Working principle of p-channel thin film transistors and methods of deriving the various device performance parameters were also discussed.

Chapter 3

Growth and characterisation of tin oxide thin films and fabrication of transparent p-SnO/n-ZnO pn heterojunction

3.1 Introduction

Transparent conducting oxides (TCOs) are a class of materials that transmit visible radiation and conduct electricity [1–6]. Amorphous transparent conducting oxides are becoming the material of choice for optoelectronic applications in numerous devices such as photovoltaics, flat-panel displays, invisible security circuits and heat reflectors [45, 46, 188]. Tin oxide has been one of the prominent mate-

rial used in various industrial applications such as a transparent electrode,transparent thin film transistor, solar-electric energy conversion device and also as a chemical sensor element [101]. Tin oxide has two stable forms : stannic oxide (SnO_2) and stannous oxide (SnO). The existence of these two oxides reveals the dual valency of tin, with oxidation states of 2^+ and 4^+. The physical properties stannous oxide have not been well explored than that of stannic oxide. For instance, optical band gap of SnO is not accurately known but lies somewhere in the range of 2.5-3 eV. SnO exhibits a smaller band gap than SnO_2, which is commonly greater than 3.3 eV. The crystal structure of SnO_2 and SnO is shown in figure 3.1.

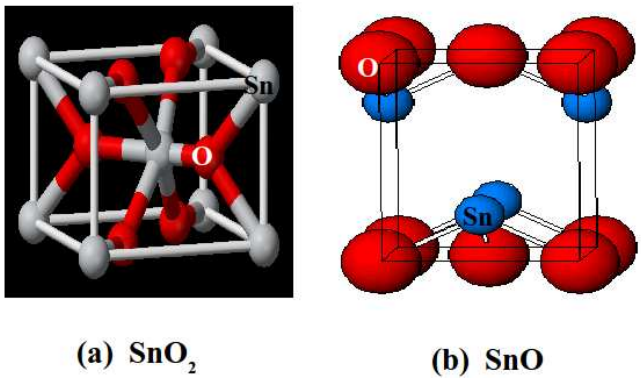

Figure 3.1: Unit cell of the crystal structure of SnO_2 and SnO.

SnO_2 has a tetragonal rutile structure and unit cell contains two tin and four oxygen atoms. Tin atom is at the centre of six oxygen atoms placed approximately at the corners of a regular octahedron, while each oxygen atom is coordinated by by three tin atoms at the corners of an equilateral triangle. SnO_2 is an intrinsic n-type semiconductor and it is used for gas sensing applications and oxidation catalysts.

Stannic oxide is the more stable and abundant form of tin oxide and its electrical conduction is due to the existence of defects which may be act as a donor. Oxygen vacancies and interstitial tin atoms are responsible for the defects which provide electrons in conduction band.

SnO has a tetragonal unit cell with the litharge structure, similar to PbO. The symmetry space group is P4/nmm and the lattice constants are a = b = 3.8029 $\mathring{A}$ and c = 4.8382 $\mathring{A}$ [190]. Each Sn and O atom form four fold coordination with a bond length of 2.23$\mathring{A}$. The structure is layered in the crystallographic direction with a $Sn_{1/2}$-O-$Sn_{1/2}$ array and a van-der-Waals gap between two adjacent tin planes is 2.52 $\mathring{A}$. The positive charge of the Sn^{2+} ions is shielded by electron charge clouds between the Sn planes,which can lower the Coulombic repulsion between neighbouring tin layers [191–193]. These charge clouds arise from Sn5s electrons that do not involve in the bonding for Sn(II) and thus can be treated as a lone pair. According to Galy et al [194] lone pair can be defined as an intermediate state between an inert spherical s orbital that is centered on the nucleus and a non-bonded hybridized-orbital lobe that is not spherical but localized far from the atomic nucleus. Figure 3.2 shows the comparison between the band structure of SnO_2 and SnO. In most of p-type transparent semiconductors (TSs), valence band originates from highly directional p-orbitals which severely limit carrier transport in a slightly disordered structure. The valence band maxima (VBM) of oxide semiconductors are mainly formed from localized and anisotropic O 2p orbitals, which track to a low hole mobility due to a percolation/hopping conduction [195]. However, if we consider the case of stoichiometric/nonstoichiometric SnO_x, this can be changed [196]. In this case the higher-energy region of VBM contains Sn 5s, Sn 5p and O 2p components nearly equally,

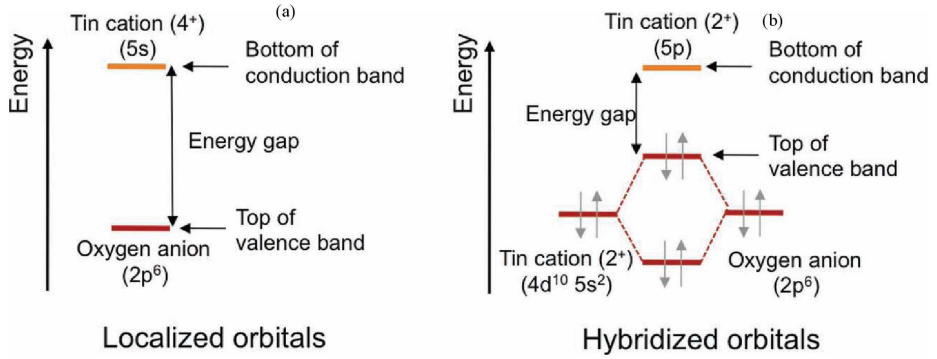

Figure 3.2: Comparison between the band structure of SnO_2 and SnO (*adapted from [189]*).

but very near the upper part of VBM, the contributions of Sn 5s and O 2p are predominant and so they define the way how free holes are generated. This can lead to an enhancement in hole mobility. This is advantageous in reducing the localization of the valence band edge, since the O 2p component is relatively small and the states near the conduction band minimum are mainly formed by Sn 5p. Under this condition, it is expected that the hole transport demands the structures mainly dominated by SnO_x with some embedded β-Sn cations in which VBM is made of pseudo closed ns^2 orbitals to form hybridized orbitals. In this scene, SnO has a specific electronic structure associated with the presence of divalent tin, Sn(II), in a layered crystal structure. The unit cell of SnO is composed by layered pyramids which are faced and engage each other alternately. The pyramid consists one Sn atom on the top of the squared four O atoms. Electrons spread into the open space between the layers (lone pairs) are expected to create characteristic physical properties of SnO. The origin of p-type conductivity of SnO is mainly due to the Sn vacancies and the O in-

terstitial [197]. If there is surplus oxygen in the film, some cations will be transformed into Sn^{4+} in order to maintain electrical neutrality. This process can be treated as Sn^{2+}capturing a hole and forming weak bonded holes. These holes are located inside the band gap near the top of the valence band and serve as acceptor states in the energy band structure [198].

The peculiar electro-optical properties of tin oxide thin films depend sensitively on the chemical surface composition, micro structure, oxygen vacancies and doping concentration. In contrast with those of SnO_2 very little is known about the properties of SnO. It is reported that the tin oxide films had SnO-like and SnO_2-like phases simultaneously and the thin film with abnormal dual conduction exhibited distinct phase separation behavior with structural modulation [199]. This indicates that the general concept relating to phase identification of tin oxide and the determination of electrical property is still obscure. Fabrication of heterojunction using p-type SnO will lead to the application of junction devices. Arun Kumar Sinha et al [200] have reported the tuning of the tin oxide (SnO/SnO_2) heterojunction by heating the as-prepared p-type SnO semiconductor in air in a controlled fashion and obtained a better photocatalytic activity for dye degradation under UV, visible as well as solar light irradiation. Tin oxide is the most significant material for use in gas sensing applications. Tin oxide gas sensors were first proposed [201] and patented in 1962. In the past 15 years, considerable research has been carried out to identify the chemical and electronic mechanisms that control semiconductor sensor functioning. There are several reports which provide detailed reviews of the scientific literature on SnO_2 sensors [202–205]. Hozer [204] has a strong emphasis on practical fabrication and the

ability of SnO_2 as sensors to the detection of a wide range of gases. A detailed discussion of the electrical properties of tin oxide sensors and schematic interpretations of sensor electronic, chemical, and physical considerations are all provided in the report of Gopel and Schierbaum [202]. Yamazoe [203] stressed on explanation of experimentally detected trends in terms of suggested electronic mechanisms for sensor response. Galatsis et al [206] fabricated p-type and n-type Fe-doped tin oxide gas sensors by the mechanochemical processing technique.

Recently p-SnO has been received particular attention as a candidate for thin film transistor applications. The first p-channel SnO TFT was fabricated by Ogo et al in 2008 using PLD [101]. Top-gate TFTs, using the epitaxial SnO channels, showed field-effect mobility of 1.3 $cm^2V^{-1}s^{-1}$, on/off ratios of 10^2 and a threshold voltage of 4.8 V. Dhananjay etal [208] have reported a hybrid complementary inverter composed with a p-SnO_2 and a n-In_2O_3 TFTs with an output gain of 11. Lee et al [209] reported p-type bottom gate TFTs on silicon substrate using a polycrystalline tin monoxide film deposited by vacuum thermal evaporation. Yabuta et al [210] reported p-type SnO TFT using polycrystalline SnO thin films as channel layer deposited by conventional RF sputtering with a subsequent annealing treatment. The authors have also explained the chance for oxidation of the SnO films which decrease hole density and produce n-type SnO_2. Fortunato et al [212] reported SnO_x TFTs deposited by RF magnetron sputtering at room temperature, and the final device was annealed at 200^oC in air for one hour. The polycrystaline SnO channel layer was composed of a mixture of tetragonal α-Sn and β -SnO phases. The TFTs exhibited a field-effect mobility above 1 $cm^2V^{-1}s^{-1}$ and an on/off ratio of 10^3. The same group could improve the transistor performance by

controlling the SnO oxidation state which led to saturation mobility of 4.6 $cm^2V^{-1}s^{-1}$ and on/off ratio above 7 x 10^4 [213]. In 2013 Jesus et al [216] reported a record mobility of 5.87 $cm^2V^{-1}s^{-1}$ in transparent p-type TFT using tin monoxide deposited by reactive dc magnetron sputtering. Table 3.1 shows the important list of p-channel SnO TFTs reported during the past 5 years.

Growth of p- type SnO thin film in pure form for the application of thin film transistor, is a challenging task since it is easily oxidized to SnO_2. In this chapter, the condition for growth of stable and reproducible p-type and n-type SnO_x, thin films by RF magnetron sputtering are described. The influence of oxygen partial pressure and annealing temperature on the structural, morphological, electrical and optical properties of tin oxide thin films were studied. A pn hetero-junction using p-type SnO and n-type ZnO has also been fabricated.

Table 3.1: Oxide p-type TFTs using tin oxide channel layer reported during the last 5 years.

Channel layer	Technique	T_{dep}-T_{post} [^{o}C]	Substrate	μ ($cm^2V^{-1}s^{-1}$)	on-off ratio	Year	Reference
SnO_x	PLD	575-200	YSZ-Al_2O_3	1.3	10^2	2008	[101]
SnO_x	Evaporation	RT-100	Si	0.01	10^3	2008	[207]
SnO_x	Evaporation	RT-100	Si	4.7 x 10^{-3}	10^2	2008	[208]
SnO_x	Evaporation	RT-310	Si	4.0 x 10^{-5}	10^2	2010	[209]
SnO_x	sputtering	RT-400	Si-SiN_x	0.24	10^2	2010	[210]
SnO_x	Evaporation	RT-400	Si	0.87	10^6	2010	[211]
SnO_x	sputtering	RT -200	Glass	1.2	10^3	2010	[212]
SnO_x	sputtering	RT -200	Glass	4.6	10^4	2011	[213]
SnO_x	PLD	RT -250	Si	0.75	10^3	2011	[214]
SnO_x	sputtering	RT-200	Si	4.6	10^3	2012	[215]
SnO	sputtering	180	PET	6.75	10^3	2013	[216]

3.2 Experimental

SnO thin films were deposited on glass substrates by RF magnetron sputtering using a metallic tin (99.999% pure, 2 inch dia) target. Depositions were carried out at room temperature, in a controlled atmosphere of oxygen and argon to favor the formation of SnO phase. Base pressure of the chamber was 6×10^{-6} mbar. Target substrate distance was kept constant at 5cm for all deposition. During sputtering RF power was fixed at 50W and substrates were rotated at a speed of 200 ^{o}/s. Argon flow rate to the chamber was 9.8 sccm for entire deposition while oxygen flow rate was varied from 0.4 sccm to 4.5 sccm for different depositions. The sputtering was performed for 5 minutes at different oxygen partial pressure Opp = $Po_2/(Po_2+P_{Ar})$, keeping the total sputtering pressure constant at 1.0×10^{-3} mbar. At this condition, the deposition rate obtained for the films deposited at Opp = 3% was 47 nm/min and the sputtering rate was found to decrease slightly with increase in oxygen partial pressure. Films prepared at lowest oxygen partial pressure with thickness 235nm, were annealed in vacuum (5×10^{-5} mbar) for three hours at temperature varying from 100 ^{o}C to 400 ^{o}C .

The structural characterization of the tin oxide thin films were carried out by PANalytical X'Pert PRO X-ray diffractometer using Cu Kα line (1.5418 Å). Compositional analysis was carried out by x-ray photoelectron spectroscopy (XPS). The thicknesses of the thin films were measured by a stylus profiler (Dektak 6M). Surface morphology of the film was studied by Agilent 5500 series atomic force microscopy (AFM) in non contact mode. Optical transmittance measurements were performed with Jasco V-570, UV-vis-NIR spectrophotometer.

Transport properties of the charge carriers were studied by Hall effect measurement. A pn heterojunction was fabricated using n-ZnO and p-SnO layer in a structure of glass/ITO/n-ZnO/p-SnO. ITO coated glass was used as the substrate for the fabrication of the pn junction. The thickness of the ITO layer was 200 nm. The ZnO n-layer film (300 nm) was deposited on ITO surface by sputtering ZnO powder target at RF power of 60 W with target to substrate distance 5 cm for 30 minutes. The SnO p-layer (350 nm) was deposited through shadow mask by the sputtering the Sn target (at Opp=3%), at RF power of 50 W for 7 minutes with target to substrate distance 5 cm.

3.3 Results and discussion

Among the range of Opp studied, p-type conduction was observed for the films deposited at the Opp in the range 3-9 % in the deposition chamber during sputtering. Below Opp=3%, films were highly metallic in nature with poor adhesion to the glass substrate. Since we used a metallic tin target for sputtering, very low Opp was not sufficient to oxidize tin resulting in metallic film. It was observed that for a deposition pressure of 1.0×10^{-3} mbar (Opp in the range of 3-9%) favours p-type SnO phase where as a high Opp (more than 9%) favors SnO_2 phase leading to n-type conduction. This could be understood based on the two well known forms of tin oxide: p-type stannus oxide (SnO)and n type stannic oxide(SnO_2).

Figure 3.3 is a selected-area electron diffraction pattern (SAED) of as-deposited tin oxide thin films showing a superposition of electron diffraction patterns of amorphous (diffuse rings) structure. Figure 3.3a is the SAED pattern of SnO thin film deposited at 3% oxygen partial

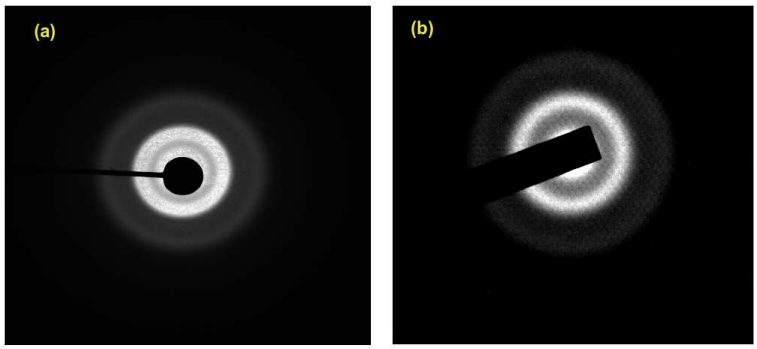

Figure 3.3: SAED patterns of (a) SnO thin film deposited at at 3% Opp. (b) SnO_2 thin film deposited at at 30% Opp.

pressure and figure 3.3b is that of SnO_2 thin film deposited at 30% oxygen partial pressure in room temperature.

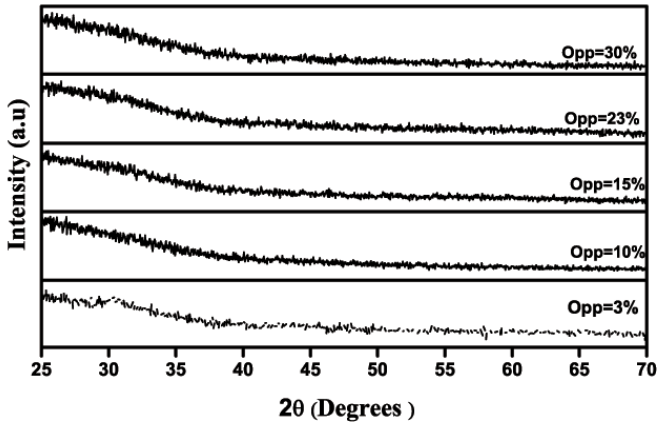

Figure 3.4: X-ray diffraction patterns of SnO_x thin films prepared at different Opp.

Figure 3.4 shows the glancing angle x-ray diffraction (GXRD) patterns of the tin oxide thin films deposited at different oxygen partial pressure. All the room temperature deposited tin oxide thin films

were amorphous in nature. Figure 3.5 shows the glancing angle x-ray

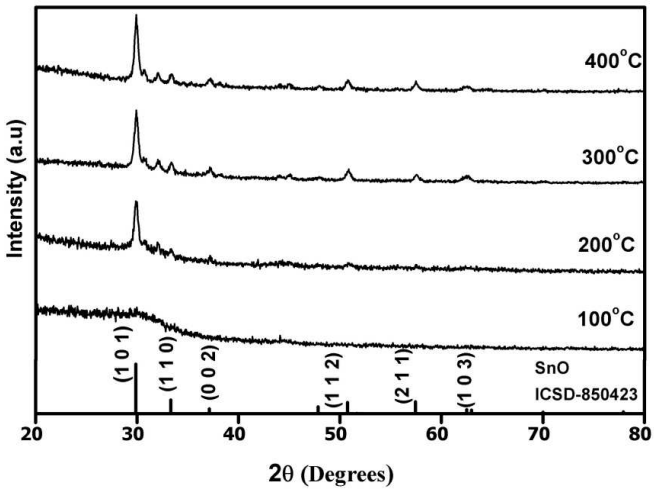

Figure 3.5: X-ray diffraction patterns of SnO_x thin films prepared at 3% Opp and annealed at different temperature.

diffraction (GXRD) patterns of the tin oxide thin films annealed in vacuum for three hours at various temperatures. Films annealed at and above 200 ^{o}C showed polycrystalline SnO phase for low Opp (3%). It can be seen from the XRD pattern that crystallinity of the films increases with the increase of annealing temperature. GXRD studies confirmed that annealed films were SnO with tetragonal structure. All the diffraction peaks are in line with the reported ICSD-850423 data and the diffraction peaks around 30 ^{o} and 32 ^{o} may be due to the presence of metallic Sn (ICSD -040038) since the metallic Sn target was used for sputtering. The average grain size of the film was calculated using full width half maximum (FWHM) of (101) peak using Scherrer equation. Since the major aim of this work was to develop p-type SnO, n-type tin oxide thin films have not been considered for

annealing treatments.

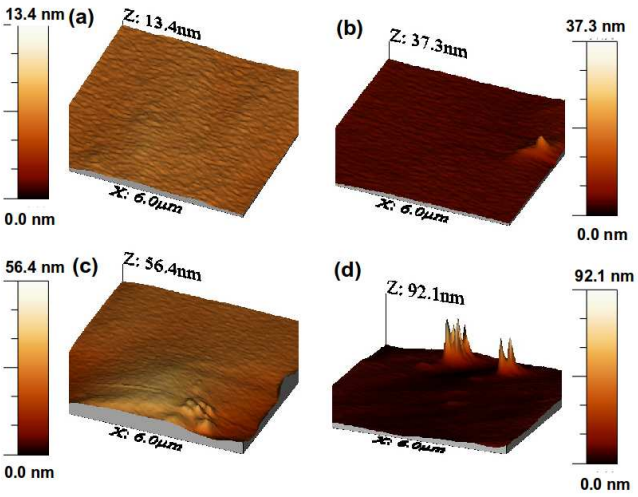

Figure 3.6: AFM images of SnO thin films annealed at (a) 100^{o}C (b) 200^{o}C (c) 300^{o}C (d) 400^{o}C.

Surface morphology of the SnO thin films were studied by AFM measurements. Figure 3.6 shows three dimensional AFM pictures of SnO thin films for different annealing temperature and figure 3.7 shows the dependence of grain size estimated from XRD using Scherrer equation and average roughness with annealing temperature. Average grain size was increased with increasing annealing temperature. This could be explained by considering the annealing coalescence of small grain boundary diffusion which resulted in major grain growth. Root mean square (rms) roughness of SnO thin film was also increased with annealing temperature. This could be explained in terms of major grain growth which yields in increase in the surface roughness [217, 218].

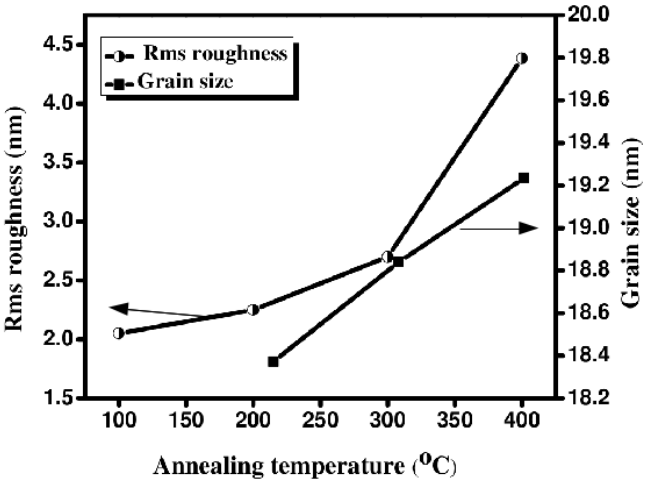

Figure 3.7: Dependence of surface roughness and grain size with annealing temperature for the film deposited at Opp of 3%.

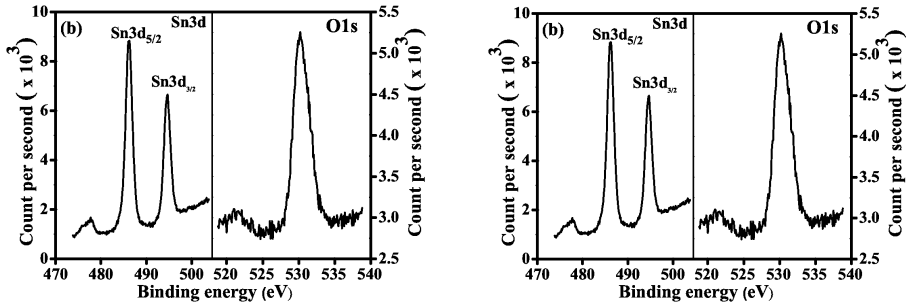

Figure 3.8: (a) XPS core level spectra of SnO_x thin film prepared at Opp=3% . (b) XPS core level spectra of SnO_x thin film prepared at Opp=30% .

XPS core level spectra of as-deposited tin oxide thin films at different oxygen pressure is shown in figure 3.8. For as-deposited SnO_x thin film at oxygen partial pressure of 3% Sn $3d_{5/2}$ and $3d_{3/2}$ binding

energy peaks were obtained at 488 eV and 496 eV respectively. (figure 3.8a). Atomic percentage of the compound according to the intensity of the XPS peak was about 49% and 51% for tin and oxygen respectively. Figure 3.8b represents XPS spectra of SnO_x thin film prepared at oxygen partial pressure of 30%. Atomic percentage of the compound according to the intensity of the XPS peak was about 36% and 64% for tin and oxygen respectively, which indicate the formation of SnO_2 phase. Atomic percentage of Sn:O is 1:2 for films grown at Opp = 30%, indicating high oxygen pressure leads to the formation of SnO_2 while low oxygen pressure leads to the formation of SnO [219–221].

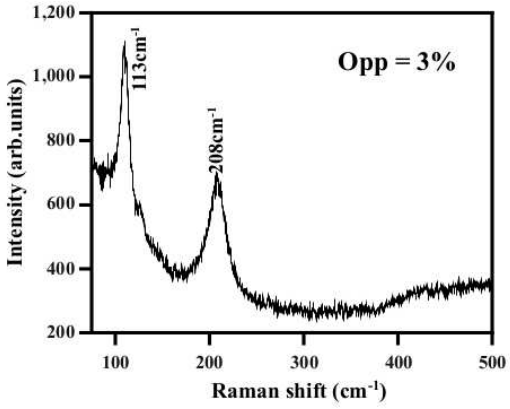

Figure 3.9: Raman spectra of as deposited SnO thin film.

The Raman spectrum (Figure 3.9) obtained from amorphous SnO thin films deposited at Opp = 3% shows two peaks, one at 113 cm^{-1} and the other at 211 cm^{-1}, as already been reported in literature [223]. The peak at 113 cm^{-1} appears for the diagonal configuration (i.e. the scattered electric field parallel to the incident electric field) as well as for the off-diagonal configuration (i.e. the scattered electric field

perpendicular to the incident electric field), although the xy and yx components in the Raman tensors vanish. The 113 cm^{-1} peak can be assigned to the B_{1g} mode. The peak at 211 cm^{-1} essentially appears only in the diagonal configuration, which can be assigned to the A_{1g} mode, where E_s is always parallel to E_i [222]. Characteristics peaks of SnO_2 at 471 cm^{-1} (E_g), 632 cm^{-1} (A_{2g}) and 773 cm^{-1} (B_{2g}) are absent in the Raman spectra obtained, which indicate that films deposited at Opp=3% is perfectly SnO.

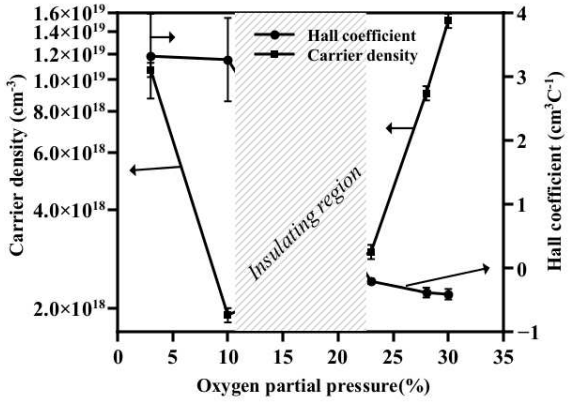

Figure 3.10: Variation of carrier density and Hall coefficient with oxygen partial pressure.

In the present study, as-deposited tin oxides samples have shown fluctuations in the sign and magnitude of Hall coefficient. The variation of carrier concentration and Hall coefficient with the oxygen partial pressure, with error bar is shown in the figure 3.10. Films prepared at Opp of 3-9% showed positive Hall coefficient while films prepared at Opp greater than 9% showed negative Hall coefficient. Carrier concentration of SnO_x thin films deposited at 3% Opp was 1.02×10^{19} cm^{-3} which first decreased and then increased with the

Opp and a maximum carrier concentration of 1.5 × 10^{19} cm^{-3} was obtained at Opp = 30%. Carrier concentration of p-type SnO_x films decrease with Opp while that of n-type SnO_x films increase with Opp.

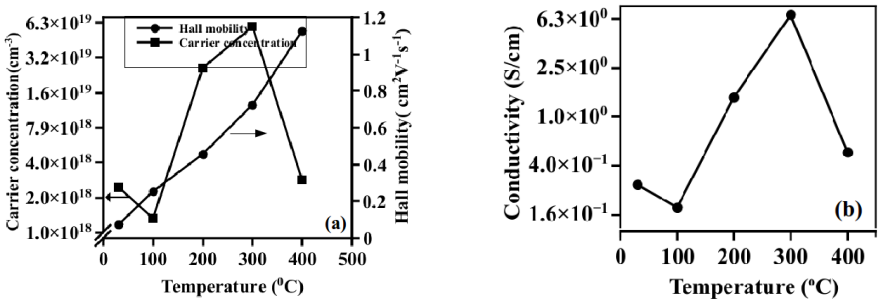

Figure 3.11: (a) Variation in the mobility and carrier concentration of SnO_X films deposited at Opp=3% as a function of annealing temperature. (b) Variation of conductivity of SnO_Xthin films deposited at Opp=3% with annealing temperature.

After annealing in the range of 100^{o}C to 400 ^{o}C for 3 hours in vacuum, films prepared in the Opp of 3% have shown positive Hall coefficient consistently. There was no change in Hall coefficient sign even though the magnitudes were shown small fluctuations. This suggests a considerably large density of holes compared to the density of electrons. Figure 3.11a shows the variation Hall mobility and carrier concentration with respect to the annealing temperature of SnO_x films. Typical carrier mobilities obtained for annealed p type SnO thin films were in the order of 0.1-1.2 cm^2 $V^{-1}s^{-1}$. Conductivity of films were measured by four probe technique. Variation in the conductivity of SnO films as a function of annealing temperature is shown in the figure 3.11b. Maximum conductivity of 6.89 S/cm was obtained for films annealed at 300 ^{o}C. The reason for decrease in conductivity may

be due to the desorption of interstitial oxygen on annealing in vacuum at 400 ^oC.

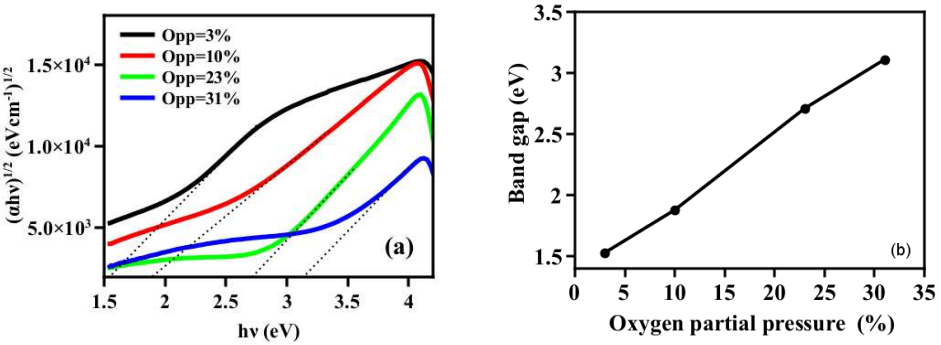

Figure 3.12: (a) Band gap estimation of as prepared SnO_x thin films deposited at different Opp (b) Variation of band gap with Opp.

Optical transmittance of as deposited films were very poor in the visible region, mainly because of the presence of large concentration of metallic tin in the films. Optical transmittance was found to increase with oxygen atmosphere. Tau plot for tin oxide thin films deposited at different Opp is shown in the figure 3.12a. Band gap of as deposited SnO_x thin films calculated from the Tauc plot was found to vary from 1.6 eV to 3.2 eV (figure 3.12b) as the oxygen atmosphere varies from 3 to 30% which indicates the oxidisation of metallic phase tin to SnO and SnO_2.

SnO_x thin films deposited at an oxygen partial pressure of 3% were annealed up to 400^oC in vacuum. Annealing considerably increased the optical transmittance in the visible region. As shown in the figure 3.13b band gap of p-type SnO_x films varied from 1.7 eV to 3.1 eV on annealing at various temperature. From the Hall measurement studies it was confirmed that all the annealed films deposited at Opp = 3%

were p-type in nature.

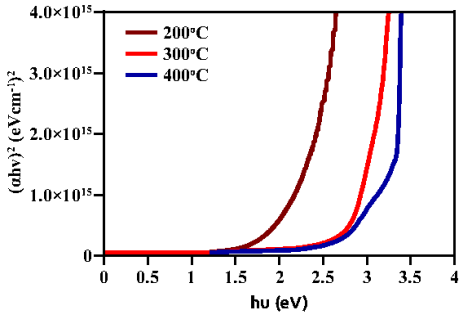

Figure 3.13: Variation of band gap with annealing temperature for SnO_x thin films deposited at Opp of 3%.

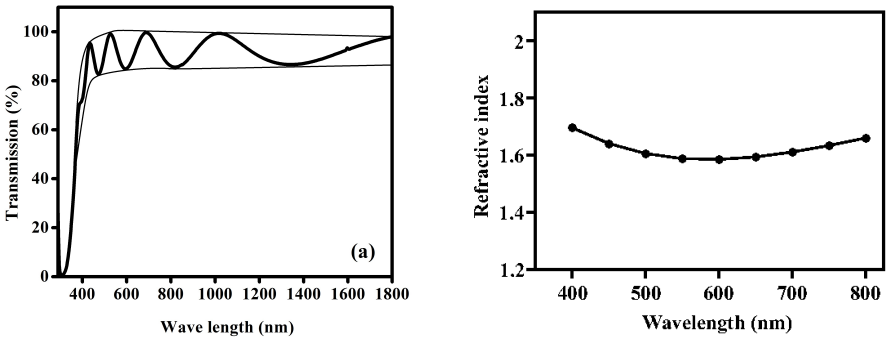

Figure 3.14: (a)Transmission spectra of SnO_2 thin film. (b)Variation of Refractive index with wavelength for SnO_2 thin film.

The Swanepoel method was employed for the analysis of the transmittance curves to estimate the refractive index and the thickness of the film. Figure 3.14a shows transmission spectrum of thin film of thickness 1200 nm. Figure 3.14b shows the variation of refractive index with wavelength for SnO_2 thin film. Film thickness was also

measured using stylus profilometer which got a good agreement with the thickness calculated from the Swanepoel technique [224].

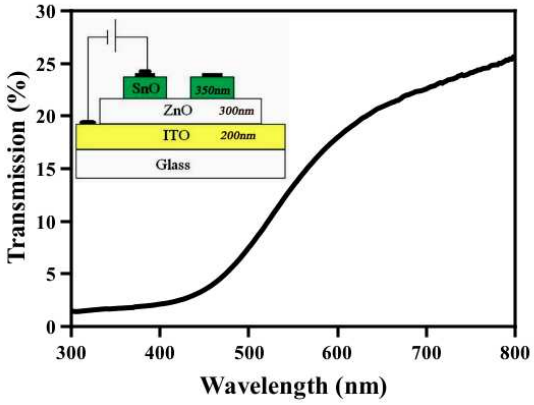

Figure 3.15: Transmission spectra of pn junction.Inset figure is the structure of pn junction.

Transmission spectra and schematic diagram of transparent pn heterojunction fabricated with structure glass/ITO/n-ZnO/p-SnO is shown in the figure 3.15. Area of the pn junction was 0.7×10^{-1} cm^2. The I-V characteristics of the junction measured using keithley 4200-SCS, is shown in figure 3.16a. The I-V characteristics shows a typical rectifying behaviour. The turn on voltage is obtained as 3V. The maximum forward to reverse current ratio is about 12 at 4.5 V. The figure inset (figure 3.16a) shows the I-V characteristics of ITO-ZnO contact which indicates the ohmic nature. Hence figure 3.16a shows the I-V characteristics of ZnO/SnO junction only.

The diode equation is $I = I_0 \exp(\frac{eV}{nkT}\text{-}1)$, where I_0 is the maximum reverse current, e is the electronic charge, V is the voltage for the current I, k is the Boltzmann constant, T is the temperature, and

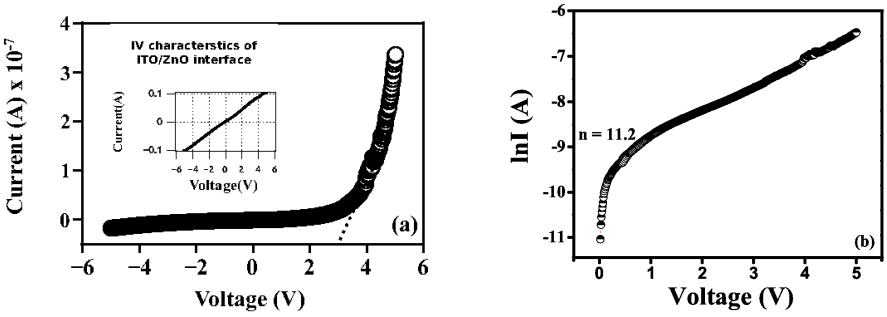

Figure 3.16: (a) I-V characteristics of ZnO-SnO junction and I-V characteristics of ITO/ZnO contact (inset). (b) Plot between voltage and lnI.

n is the ideality factor. For ideal diodes n varies between 1 and 2. From the plot lnI versus V (figure 3.16b), at very small voltages the ideality factor is 11.2 and at higher voltages it is 62. The high value of ideality factor can be attributed to poor interface and defects at the interface. The n-ZnO/p-SnO junction can not be considered as an ideal abrupt junction. Since ZnO is deposited in pure argon and and oxygen deficiency in ZnO generates carriers while SnO is deposited in 3% of oxygen pressure. This may lead to oxygen diffusion to ZnO layer forming a very thin intrinsic region of ZnO. According to Wang et al, the heterojunction diode can be modeled in different bias ranges by a series of diode and resistance [313]. The ideality factor of the device is the sum of ideality factors of the individual junction and may lead to ideality factor much greater than two [226–229].

The attempts to fabricate bottom gate structured TFT using p-channel SnO by RF sputtering was not successful. A glass substrate deposited with 200 nm thick layer of sputtered ITO and a 220 nm thick layer of aluminium-titanium oxide (ATO) was used for TFT fabrication. Unfortunately fabricated TFT have not shown any tran-

sistor action because of large carrier concentration ($10^{18}/cm^3$) of the channel layer. Difficulty in controlling the carrier concentration was main hindrance for the successful functioning of p-channel SnO TFT. Growth parameter for p-channel SnO with lower carrier concentration have to be optimised for the further fabrication of successful TFTs.

3.4 Conclusion

p-Type and n-type tin oxide thin films were deposited by RF-magnetron sputtering at different oxygen partial pressure. Structural, optical and electrical properties of these films were studied as a function of oxygen partial pressure and annealing temperature. Amorphous structure of as-deposited SnO_x films and polycrystalline tetragonal structure of annealed SnO films were confirmed by GXRD. Surface morphology of synthesized samples was characterised by atomic force microscopy. Atomic percentage of the SnO thin film according to the intensity of the XPS peak was about 48.85% and 51.15% for tin and oxygen respectively. Band gap of as deposited SnO_x thin films was varying from 1.6 eV to 3.2 eV as the oxygen partial pressure varies from 3-30% which indicates the oxidization of metallic phase tin to SnO and SnO_2. Type of the charge carrier and conductivity of the tin oxide thin films were varied with oxygen partial pressure. Transparent pn heterojunction fabricated in the structure glass/ITO/n-ZnO/p-SnO show rectifying behaviour. By controlling the carrier concentration p-type tin oxide films can be used as the channel layer for transparent thin film transistor and in various industrial applications such as a solar-electric energy conversion device and chemical sensor element.

Chapter 4

Growth of copper oxide thin films for possible transparent electronic applications

4.1 Introduction

The first reported semiconductor metal oxide was cuprous oxide in 1917 by Kennard et al [230]. It was used for solid state device even before the era of silicon devices. Several reports on copper oxides have been published in recent years mainly because of their p-type conductivity, making these key semiconductor materials for active applications in the field of transparent electronics [231, 232].

Copper forms two well known oxides: cuprite (Cu_2O) and tenorite (CuO). A metastable copper oxide, paramelaconite (Cu_4O_3), which is an intermediate compound between the previous two, has also been reported[233]. Cu_2O forms a cubic (figure 4.1a) structure with a lattice

parameter of 4.27 $\mathring{A}$, the Cu_4O_3 bears a tetragonal structure having lattice parameters: a = 5.837 $\mathring{A}$ and c = 0.9932 $\mathring{A}$. In CuO, units of Cu_2O are chained and Cu forms four coplanar bonds with oxygen [234]. Amongst the mono oxides of 3d transition series elements, CuO is unique as it has a square planar coordination of copper by oxygen in the monoclinic structure (figure 4.1b). The lattice parameters of CuO are a = 4.684 $\mathring{A}$, b = 3.425 $\mathring{A}$, c = 5.129 $\mathring{A}$ and $\beta = 99.28^o$ [235].

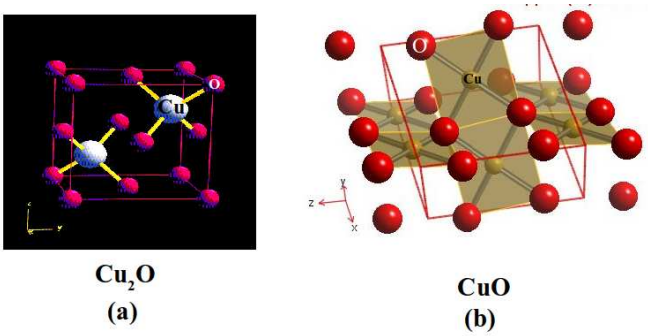

Figure 4.1: Crystal structure of (a) Cu_2O and (b) CuO.

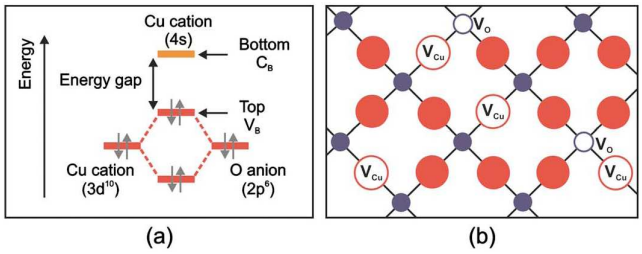

Figure 4.2: Chemical bond between oxide ion and copper cation that has a a closed shell configuration (b) a pictorial representation of the more significant defects in Cu_2O.

Both cubic Cu_2O and monoclinic CuO shows p-type conductivity.

Optical band gap of Cu_2O is 2.1-2.6 eV and that of CuO is 1.6-1.9 eV [238]. The p-type behaviour of these materials arises from the existence of negatively charged copper vacancies and interstitial oxygen has also been refered as a possible cause [236, 237]. The top of valence band is mainly formed from completely occupied hybridised orbitals of Cu 3d and O 2p with Cu d states dominating the top of the valance band [68]. Figure 4.2a represents the chemical bonding between oxide ion and Cu cation and figure 4.2b shows a pictorial representation of most significant defects in Cu_2O. The deposition of CuO thin films has been reported by a variety of growth techniques, such as electrodeposition [239], spin coating [240], magnetron sputtering [241], pulsed laser deposition [242] and chemical vapour deposition [243]. Magnetron sputtering allows easy tailoring the phase composition from Cu_2O via Cu_4O_3 to pure CuO by simply tuning the oxygen partial pressure during reactive deposition [244, 245]. Recently, few groups have reported p-type oxide semiconductor based TFTs using the CuO and Cu_2O as active channel material [249, 251, 253, 254, 256, 257, 296]. Recent developments in copper oxide TFTs are summaraised in table 3.1 concerning the technique, deposition temperature, substrate, channel moblity and on off ratio. Fortunato et al [250] fabricated Cu_2O thin films by thermal treatment at 200^oC for 10 hours and fabricated Cu_2O TFTs with field effect mobility of 1.2×10^{-3} $cm^2V^{-1}s^{-1}$. Sung et al [248] fabricated TFT on p-type silicon substrate using post annealed CuO channel layer with field effect mobility of 0.4 $cm^2V^{-1}s^{-1}$ and on/off ratio 1.1×10^4. This chapter is divided in to three sections viz., the systematic synthesis of copper oxide thin films at room temperature using RF magnetron sputtering by varying oxygen partial pressure so as to get Cu_2O and CuO phase, Fabrication of transpar-

ent flexible pn heterojunction in the structure PET/ITO/n-ZnO/p-CuO/Au and fabrication of room temperature deposited transparent p-type thin film transistors with Cu_2O and CuO channel layers.

Table 4.1: p-Type TFTs using copper oxide channel layers reported during the last 5 years.

Channel layer	Technique	T_{dep}-T_{post} [^{o}C]	Substrate	μ ($cm^2V^{-1}s^{-1}$)	on-off ratio	Year	Reference
Cu_2O	PLD	700	MgO	0.26	0.6 x 10^1	2008	[247]
CuO	sputtering	RT-200	Si	0.4	10^4	2010	[248]
Cu_2O	PLD	500	Si	4.3	3 x 10^6	2010	[249]
Cu_2O	PLD	RT-200	glass/ITO	1.2 x 10^{-3}	2 x 10^2	2010	[250]
Cu_2O	PLD	500	Si	2.40	1.5 x 10^6	2011	[251]
Cu_2O	sputtering	RT -500	PET/ITO	2.7	3.9 x 10^4	2012	[252]
Cu_2O	sputtering	RT -450	Si	0.063	10^4	2012	[253]
Cu_2O	spin coating	RT -400	Si	0.16	10^2	2013	[254]
Cu_2O	sputtering	RT -450	Si	.07	10^4	2013	[255]
Cu_2O	spray pyrolysis	275-200	Si	10^{-3}-10^{-4}	10^3	2013	[256]
Cu_2O	sputtering	RT -800	Si	.06	10^4	2013	[257]
CuO	sputtering	RT	glass	0.01	10^4	2014	[258]
Cu_2O	sputtering	RT -150	Si	1.31	10^4	2014	[259]

4.2 Growth and characterisation of copper oxide thin films

4.2.1 Experimental

Copper oxide thin films were deposited on glass substrates by RF magnetron sputtering using a metallic copper (99.999% pure, 2 inch dia) target. Depositions were carried out at room temperature in a controlled atmosphere of oxygen and argon which favors the formation of Cu_2O or CuO phase depending on the oxygen to argon ratio in the chamber. Base pressure of the chamber was 6×10^{-6} mbar. Target to substrate distance was kept constant at 10 cm for all depositions. RF power was fixed at 60 W and substrates were rotated at a speed of 200 ^{o}/s. Flow rate of argon to the chamber was 50 sccm for the entire deposition process and the oxygen flow rate was varied from 0.4 sccm to 16 sccm. The sputtering was performed for 30 minutes at different oxygen partial pressure Opp = $\frac{Po_2}{Po_2+P_{Ar}}$ x 100.

The structural characterization of the copper oxide thin films were carried out by PANalytical X'Pert PRO x-ray diffractometer using Cu Kα line (1.542512 Å). Compositional analysis was carried out by x-ray photo electron spectroscopy (XPS). The thicknesses of the thin films were measured by a stylus profiler (Dektak 6M). Surface morphology of the film was studied by Agilent 5500 series atomic force microscopy (AFM) in non contact mode. Optical transmittance measurements were performed with Jasco V-570, UV-vis-NIR spectrophotometer. Transport properties were studied by Hall effect measurement in the van der Pauw geometry using Ecopia, HMS-3000.

4.2.2 Results and discussion

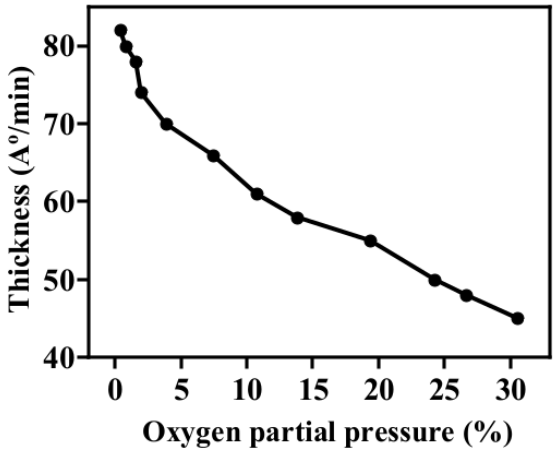

Figure 4.3: Variation of film thickness with oxygen partial pressure.

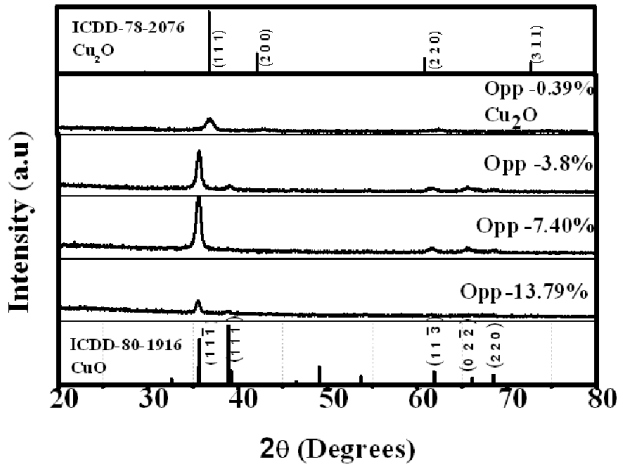

Figure 4.4: X-ray diffraction patterns of copper oxide thin films prepared at different Opp.

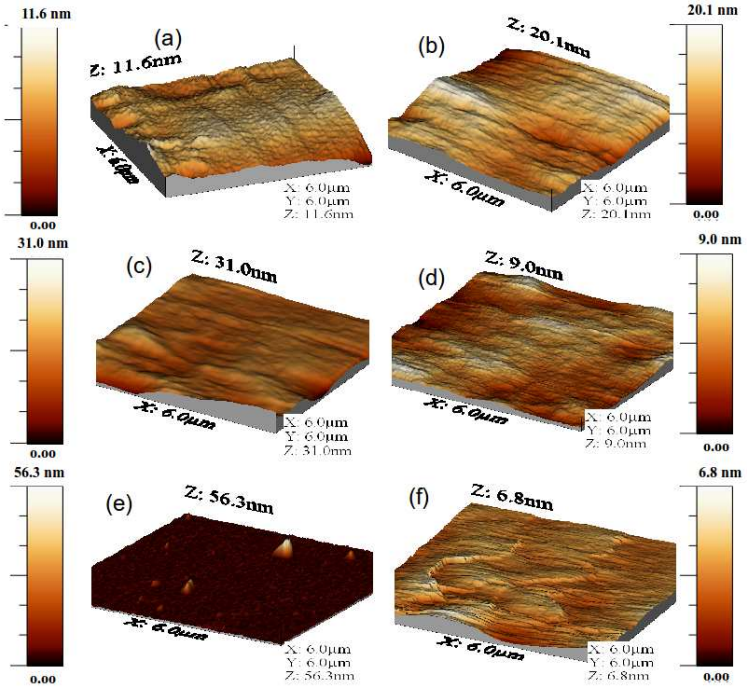

Figure 4.5: AFM images of copper oxide thin films deposited at different Opp. (a) 0.39% (b) 0.7% (c) 3.8% (d) 7.39% (e) 13.79% (f) 24.24%.

Copper oxide thin films were successfully grown on glass substrate by varying oxygen partial pressure. Sputtering rate was found to decrease with increase in oxygen partial pressure figure 4.3. The decrease in deposition rate with oxygen pressure in the sputtering of metal oxides is a generally observed phenomenon and it is attributed to the compound formation at the metal target surface due to the presence of reactive oxygen gas [260, 261].

Figure 4.4 shows the glancing angle x-ray diffraction (GXRD) patterns of the copper oxide thin films deposited at Opp 0.39%, 3.8%,

7.4% and 13.7% respectively for 30 minutes at room temperature. It can be seen from the figure that at Opp 0.39% Cu_2O film with cubical structure (ICDD-78-2076) is obtained and at higher Opp CuO phase with monoclinic structure is obtained. This indicates that the oxidation of Cu^{1+} to Cu^{2+} when increasing the oxygen partial pressure. All the diffraction peaks were in line with the reported ICDD (80-1916) data of CuO.

Surface morphology of the CuO thin films were studied by atomic force microscopy(AFM). Figure 4.5 shows three dimensional AFM morhology of copper thin films deposited at different oxygen partial pressures. Rms roughness values were 1.41 nm, 2.8 nm, 2.37 nm, 1.33 nm , 1.90 nm and 0.63 nm for the copper oxide films deposited at at 0.39%, 0.7%, 3.8%, 7.4%, 13.79% and 24.24% respectively. CuO films with smooth surface (Opp: 7.39% and 13.79%) were used for device fabrications.

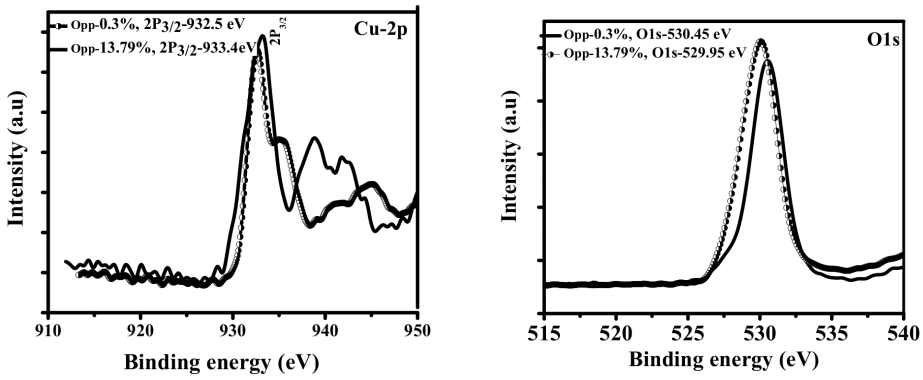

Figure 4.6: (a) XPS core level spectra of Cu-$2p_{3/2}$ and (b) O1s for the films deposited at Opp=0.3% and 13.79%.

X-ray photoelectron spectroscopy (XPS) core level spectra of the as

deposited copper oxide thin films at different oxygen pressure is shown in figure 4.6. By increasing the oxygen partial pressure the binding energy of Cu $2p_{3/2}$ in the as-deposited films increased from 932.5 eV to 933.4 eV due to the oxidation of Cu^{+} to Cu^{2+}. The binding energies of O 1s were observed to be 530.45 eV for the as-deposited Cu_2O films and 529.95 eV for CuO films deposited at higher Opp(13.73%). Binding energy values obtained in this experiment are similar to the observation made by Ghijsen et al [267]. These results indicated that copper oxide film deposited at Opp = 0.39% and Opp = 13.73% have one main peak of Cu^{+}, Cu^{2+} respectively. It is evident that higher Opp is required for the formation of CuO phase.

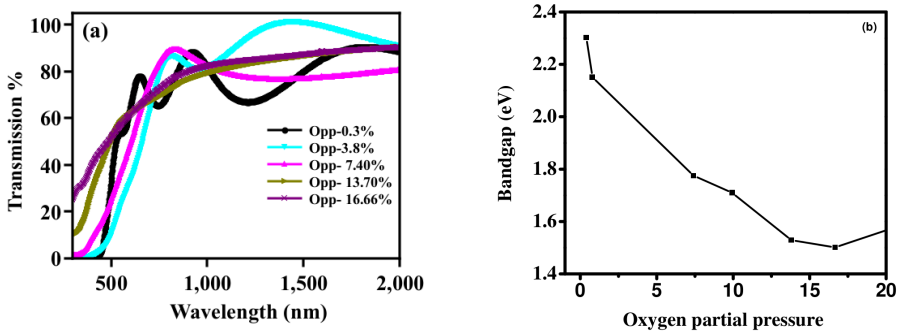

Figure 4.7: a) Transmsission spectra of copper oxide thin films deposited at different Opp.(b) Band gap variation of copper oxide thin films with oxygen partial pressure.

Transmission spectra of copper oxide thin films deposited at different oxygen partial pressure is shown in the figure 4.7a. Direct band gap of copper oxide thin films were estimated from the plot of $(\alpha h\nu)^2$ versus $h\nu$. Variation of band gap with oxygen partial pressure is shown in the figure 4.7b. The band gap is found to be greater than 2 eV for films deposited at lower Opp and less than 2 eV for films deposited at

higher Opp, which indicates conversion of Cu_2O phase to CuO phase as the oxygen partial pressure increases [268].

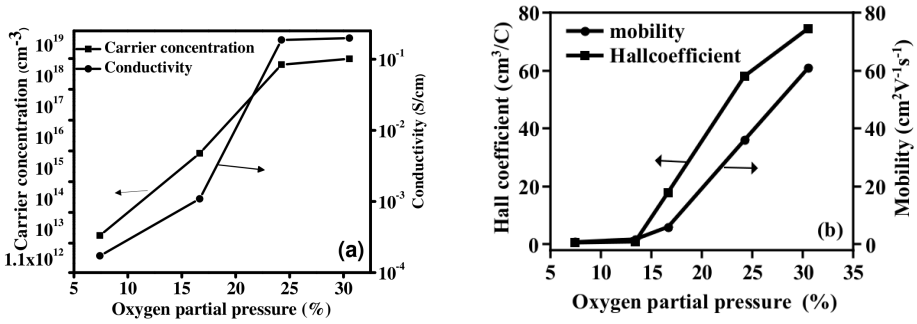

Figure 4.8: a) Dependence of carrier concentration and conductivity of copper oxide thin films on Opp.(b) Variation of Hall mobility and Hall coefficient of copper oxide thin films with oxygen partial pressure.

Dependence of carrier concentration and conductivity of copper oxide thin films on oxygen partial pressure is shown in the figure 4.8a. Hall coefficient and mobility values obtained for films deposited at different Opp is shown in figure 4.8b. All the as deposited copper oxide thin film showed p-type Hall coefficient. Cu_2O film deposited at Opp = 0.39% was highly resistive and hence Hall measurement did not lead to consistent result due to the limitation of experimental set up. Conductivity and mobility of copper oxide thin films increased with Opp. This may be due to the increase of interstitial oxygen in copper oxide films with lower carrier concentration (Opp = 13.79% and 7.39%) was used as the channel layer for the fabrication of TFT and for fabrication of pn junction.

4.3 Fabrication of pn heterojunction

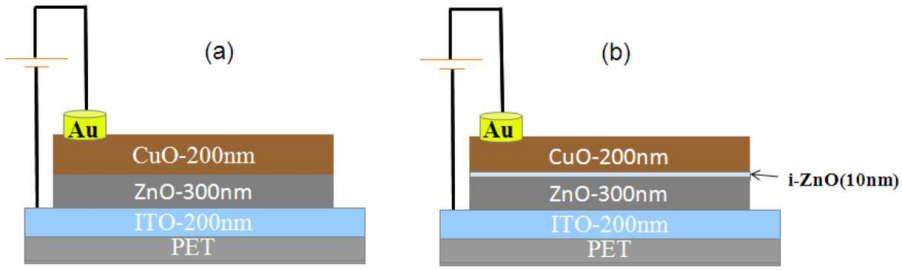

Figure 4.9: Schematic diagram of pn heterojunction (a) with out intrinsic layer of ZnO and (b) with intrinsic layer of of ZnO.

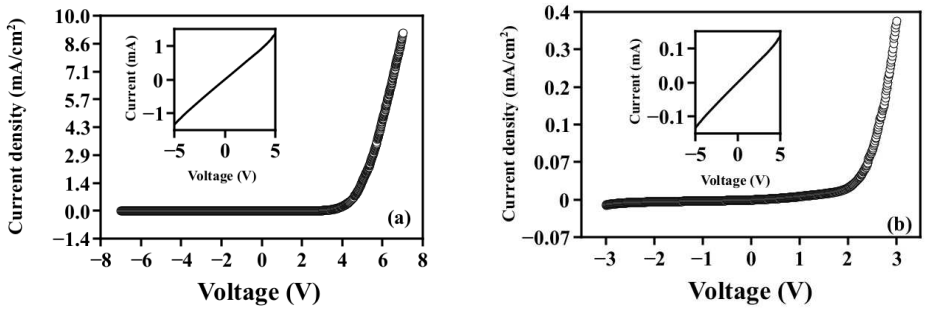

Figure 4.10: I-V Characteristics of pn heterojunction (a) with out intrinsic layer of ZnO and (b) with intrinsic layer of of ZnO.

A pn heterojunction was fabricated using n-ZnO and p-CuO layer in the structure of PET/ITO/n-ZnO/p-CuO. ITO coated PET substrate was used for the fabrication of the pn junction. The thickness of the ITO layer was 200 nm. Schematic diagram of pn heterojunction (pn) with ZnO intrinsic layer is shown in the figure 4.9a. The ZnO n-layer film (300 nm) was deposited on ITO surface by sputtering ZnO powder

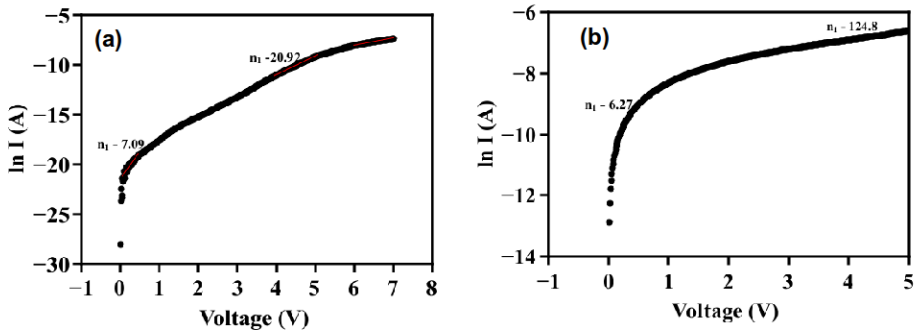

Figure 4.11: Plot between voltage and lnI for diode (a) with out intrinsic layer of ZnO and (b) with intrinsic layer of of ZnO.

target at RF power of 60 W for 30 minutes, keeping 5 cm of distance between target and substrate. Schematic diagram of pn heterojunction (pin) with ZnO intrinsic layer is shown in the figure 4.9b. The ZnO n-layer film (290 nm) was deposited on ITO surface by sputtering ZnO powder target at RF power of 60 W for 25 minutes, keeping 5 cm of distance between target and substrate. For the deposition of ZnO intrinsic layer (10 nm) oxygen is fed to the chamber at the rate of 10 sccm and all other deposition parameters kept constant. The CuO p-layer (200 nm) was deposited through shadow mask by the sputtering of the Cu target (at Opp=7.4%) at RF power of 60 W for 30 minutes, keeping 10 cm of distance between target and substrate.

Figure 4.10a and 4.10b show the I-V characteristics of heterojunction without and with ZnO intrinsic layer. The I-V characteristics shows a typical rectifying behaviour. The turn on voltage is obtained is 4 V and 2 V for diode (pn) with out intrinsic layer and with ZnO

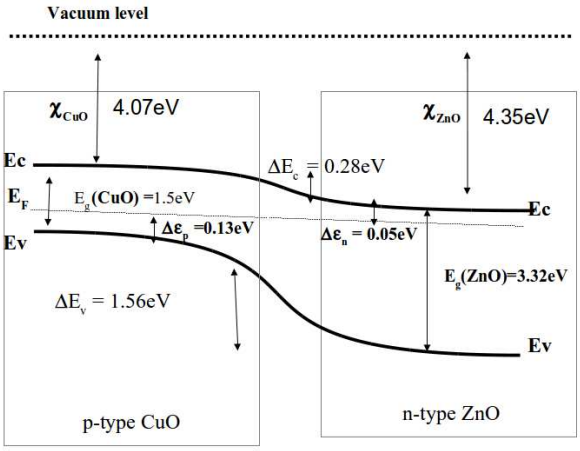

Figure 4.12: Band structure of n-ZnO/p-CuO heterojunction in equilibrium.

intrinsic layer (pin) respectively. The maximum forward to reverse current ratio is about 12 at 5 V for pn junction and 35 at 2 V for pin junction. The figure inset shows the I-V characteristics of ITO-ZnO contact which indicates ohmic nature. Hence the I-V characteristics shown in the figure 4.10a and 4.10b shows that the junction is between ZnO/CuO. The diode equation is $I = I_0 \exp(\frac{eV}{nkT}\text{-}1)$, where I_0 is the maximum reverse current, e is the electronic charge, V is the voltage for the current I, k is the Boltzmann constant, T is the temperature, and n is the ideality factor. For ideal diodes n lies between 1 and 2. From the plot lnI versus V (figure 4.11a), at very small voltages the ideality factor is 7.09 and at higher voltages it is 20.92 for pn junction. Ideality factor of pin junction calculated from the figure 4.11b, is 6.27 at lower voltage and 124.8 at higher voltage. The high value of ideality factor can be attributed to poor interface and defects at the interface

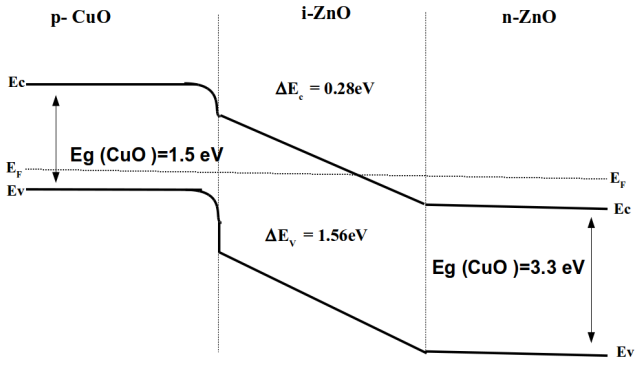

Figure 4.13: Energy-band diagram for the p-CuO/i-ZnO/n-ZnO pin heterojunction in equilibrium.

of ZnO/CuO. The n-ZnO/p-CuO junction cannot be considered as an ideal abrupt junction. Since ZnO is deposited in pure argon and oxygen deficiency in ZnO generates carriers while CuO is deposited in 7.4% of oxygen pressure. This may lead to oxygen diffusion to ZnO layer forming a very thin intrinsic region of ZnO. According to Wang et al, the heterojunction diode can be modeled in various bias ranges by a series of diode and resistance [313]. The ideality factor of the device is the sum total of ideality factors of the individual junction and may lead to ideality factor much greater than two.

From the experimentally determined band gap of each layer and using the reported values of electron affinities, energy band structure of CuO-ZnO pn heterojunction can be constructed using Anderson model neglecting the effects of dipole and interfacial states. The obtained band gap of ZnO is about 3.32 eV. The Reported energy difference ($\Delta\epsilon_n$ = E_c - E_F) between the conduction band edge and Fermi level E_{Fn} is of 0.05eV for ZnO [262]. Reported value of electron affinity

χ_{e-ZnO} is 4.35 eV [263]. Band gap of CuO obtained in the present study is 1.5 eV. The energy difference $\Delta\epsilon_p$ between the valence band and the Fermi level E_{F-p}, and the electron affinity (χ_{p-CuO}) of CuO were reported to be 0.13 eV, and 4.07 eV, respectively [264, 265]. From these values the conduction and valence bands discontinuities ΔE_C and ΔE_V[(E_{g-ZnO} -E_{g-CuO})-ΔE_C] are estimated to be 0.28 eV, and 1.56 eV, respectively. Based on these values the constructed schematic band diagram of CuO/ZnO heterojunction obtained, is shown in figure 4.12. The energy band diagram of the synthesized CuO/ZnO pn diode provides a first order estimation of their heterojunction under thermal equilibrium condition.

The proposed energy-band diagram for the transparent p-CuO/i-ZnO/In-ZnO pin heterojunction at equilibrium is shown in figure 4.13. Intrinsic i-ZnO layer sandwiched between p-CuO and n-ZnO act as an electron blocking layer which stabilizes particular defects and affects Fermi-level of n-ZnO layer [266]. i-ZnO layer modulates the energy band between n-ZnO and p-CuO smoother [270]. A thin tunneling barrier across the pin junction is the result of large valence band off-set. As the three materials are brought into contact electrons in the n-ZnO are transferred to the p-CuO through the i-ZnO layer and holes are transferred in the opposite direction until the Fermi-level is aligned and a constant Fermi-level will be formed. Forward biasing may inject electrons from n-ZnO layer into p-CuO layer since the energy barrier for electrons is lower than that of holes at the heterojunction interface [266]. When the forward bias voltage is equal to the threshold voltage, the conduction band minimum of i-ZnO is greater than the interface state levels [270]. The electrons from the conduction band of n-ZnO may tunnel through the junction potential barrier into the empty in-

terface states and then transfer in to the valence band of p-CuO to execute a forward current [271].

4.4 Fabrication of thin film transistors

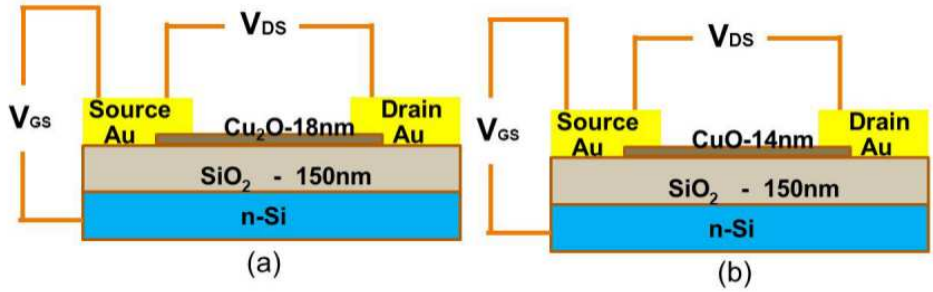

Figure 4.14: Schematic diagram of TFT with (a) Cu_2O and (b) CuO channel layers.

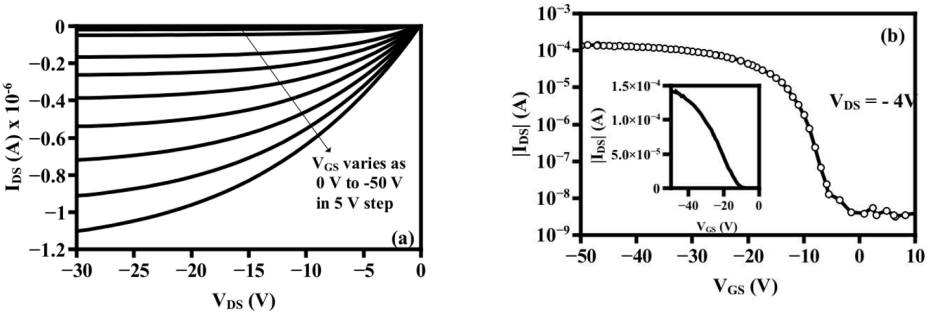

Figure 4.15: (a) Output characteristics V_{DS}- I_{DS} and (b) Transfer characteristics V_{GS} - I_{DS} of Cu_2O TFT. The field effect mobility was estimated from the slope of linear part of V_{GS}- I_{DS} curve (inset)

.

The bottom gate structures of TFT fabricated with Cu_2O and CuO channel layers is shown in the figure 4.14. A silicon substrate with

thermally oxidised 200 nm thick SiO_2 layer was used for TFT fabrication. Cu_2O and CuO (14 nm) channel layers were deposited by sputtering of copper target at 60 W for 2 minutes with Opp 0.39% and 7.39% respectively. The deposition time for the channel layer was controlled knowing the sputtering rate inorder to get the desired thickness. Sputtering rate was derived from the film thickness obtained from stylus profiler for thick films. The Au source and drain electrodes were deposited by thermal evaporation through shadow mask. The channel width and length were 2500 μm and 60 μm, respectively.

TFT was successfully fabricated with Cu_2O as channel layers. As deposited Cu_2O channel layer was annealed at 150 ^0C for 30 minutes. The drain current - drain voltage (I_{DS}-V_{DS}) characteristics of the transistor, given in figure 4.15a, shows typical enhancement mode operation of p-channel transistor. A negative gate voltage was required to induce the channel conduction, and the channel conductivity increased with increase of negative gate voltage. Figure 4.15b shows the transfer characteristics (I_{DS}- V_{GS}) of the fabricated transistors which give an on-off ratio of 10^4. The inset graph of figure 4.15b is the same drain current plot on a linear scale, the slope of which is used for field effect mobility calculation. The field effect mobility extracted from the linear region slope of I_D-V_{GS} plot was 1.31 $cm^2V^{-1}s^{-1}$. The threshold voltage V_T, estimated by extrapolating the straight line to the V_{GS} axis, was -10.35 V. The negative threshold voltage indicates the enhancement mode operation of the device. A maximum sub threshold voltage swing of 2.2 V/dec obtained from the transfer curve of the devices. Zou et al reported a mobility (4.3 $cm^2V^{-1}s^{-1}$) for Cu_2O TFT fabricated using PLD at 500 ^0C, which is the highest mobility for a Cu_2O TFT realised so far. Mobility reported for Cu_2O TFT fabricated

using room temperature sputtering is less than 1 $cm^2V^{-1}s^{-1}$ only. In the present study high mobility of 1.31 $cm^2V^{-1}s^{-1}$ were obtained for Cu_2O TFT fabricated using room temperature sputtering followed by annealing at relatively low temperature of 150 ^0C. The better TFT mobility may be due to the decrease in scattering of both ionized defects and the grain boundary for Cu_2O channel layer. As prepared

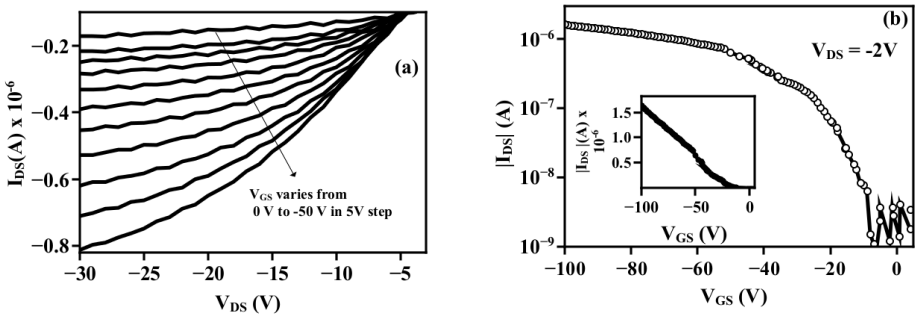

Figure 4.16: (a) Output characteristics V_{DS}- I_{DS} and (b) Transfer characteristics V_{GS} - I_{DS} of Cu_2O TFT. The field effect mobility was estimated from the slope of linear part of V_{GS}- I_{DS} curve (inset)

.

CuO devices showed good transistor action without any kind of thermal treatment. The drain current - drain voltage (I_{DS}-V_{DS}) characteristics of the transistor is given in figure 4.16a. Non ideal behaviour of the output characteristics may be due to either the series resistance of the electrodes or due to the large leakage current [269]. Figure 4.16b shows the transfer characteristics (I_{DS}- V_{GS}) of the fabricated transistors which give an on-off ratio of 10^3. The inset graph of figure 4.16b is the same drain current plot on a linear scale from which the field effect mobility extracted from the slope of linear region was 1.43 $\times$ 10^{-2} $cm^2V^{-1}s^{-1}$. The threshold voltage V_T, estimated by extrap-

olating the straight line to the V_{GS} axis, was -19.08 V. A maximum sub threshold voltage swing of 4.8 V/dec obtained from the transfer curve of the devices.

4.4.1 Fabrication of p-channel transparent CuO thin film transistor

Transparent electronics is an advancing science and technology field aimed on manufacturing invisible electronic circuits. Transparent electronics came in to a reality only after the development of p-type wide band gap oxide thin films. Transparent thin film transistors(TTFTs) are attracting more attention since it is a key device in realising transparent displays. Even though some people have reported copper based oxide TFTs as mentioned in the literature, up to the date there is no report on p-channel copper oxide TTFTs. In this section room temperature deposited transparent CuO thin film transistor on glass substrate is discussed.

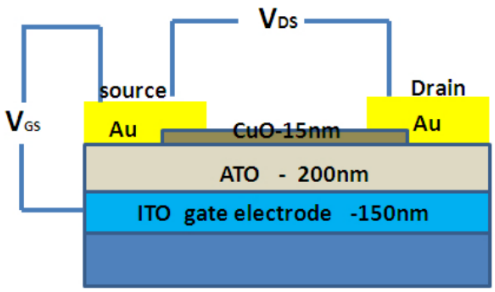

Figure 4.17: Schematic diagram of transparent TFT using p-type CuO as channel layer.

The bottom gate structures of transparent TFT fabricated with p-

channel CuO is shown in the figure 4.17. A glass substrate deposited with 200nm thick layer of sputtered ITO and a 220nm thick layer of aluminium-titanium oxide (ATO), supplied by Planar Systems Inc., was used for TFT fabrication. ITO electrode is a highly transparent n-type conductor (sheet resistance $20\Omega/cm^2$) which acts as the TFT gate. ATO is an engineered insulator consisting of a superlattice of alternating layers of Al_2O_3 and TiO_2, which serves as gate insulator. A 15 nm thick CuO channel layer was deposited by RF sputtering using a 2 inch diameter metallic copper(99.99% pure) target at 60 W. Depositions were carried out at room temperature for two minutes, in a controlled atmosphere of oxygen (8 sccm) and argon (50 sccm) to favor the formation of CuO phase. Base pressure of the chamber was 7×10^{-6}mbar. Target substrate distance was kept at 10 cm for all depositions. Oxygen flow percentage [Opp = $(\frac{Po_2}{Po_2+P_{Ar}})\times$ 100] to the chamber during deposition of CuO channel layer was 13.7%. Thickness of the channel layer was controlled by controlling the deposition time knowing the sputtering rate. Sputtering rate was calculated by measuring the thickness of the film using stylus profiler and duration of sputtering. By knowing the deposition rate we could control the channel thickness by controlling the deposition time. The TFT cross sectional analysis was performed using Carl Zeiss Neon 40 FIB/SEM. From the cross sectional SEM (figure 4.18b), the individual layers of the device can be distinguished and the thickness of the CuO layer was found to be 12 nm which is good agreement with the thickness estimated from rate of deposition. The Au source and drain electrodes were deposited by thermal evaporation through shadow mask. The channel width and length were 2500 μm and 60 μm, respectively.

Transmission spectra of CuO channel layer (12 nm) and the device

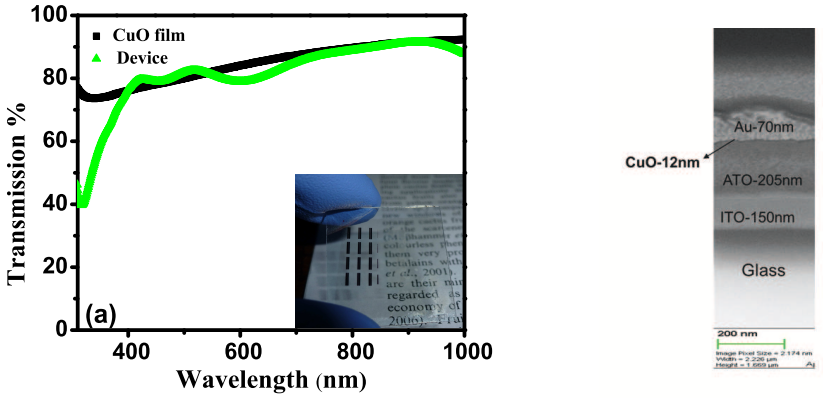

Figure 4.18: (a) Transmission spectra of CuO thin film (15nm) and the device. Inset figure is the photograph of the device (b) cross sectional SEM image of CuO TFT.

along with the photographs of transparent devices is also shown in the figure 4.18a. TFT shows average transmission greater than 70% in the visible region. The devices are completely transparent to visible light which is confirmed by the back ground images visible though the device structure.

As prepared CuO devices showed good transistor action without any kind of thermal treatment. The drain current - drain voltage (I_{DS}-V_{DS}) characteristics of the transistor, given in figure 4.19a, shows typical enhancement mode operation of p-channel transistor. A negative gate voltage was required to induce the channel conduction, and the channel conductivity increased with increase of negative gate voltage. Non ideal behaviour of the output characteristics may be due to either the series resistance of the electrodes or due to the large leakage current [269]. Figure 4.19b shows the transfer characteristics (I_{DS}- V_{GS}) of the fabricated transistors which give an on-off ratio of

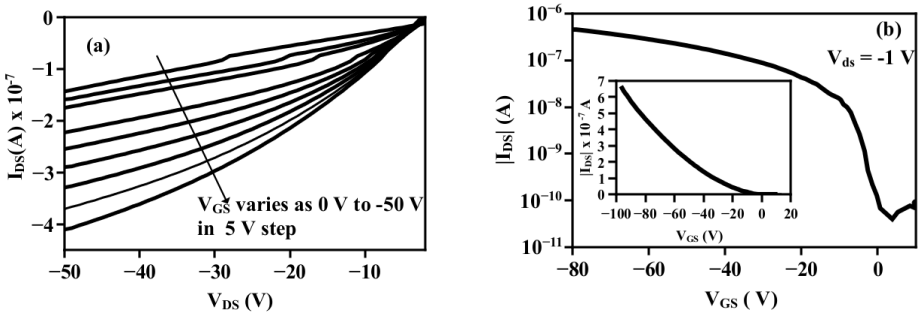

Figure 4.19: (a) Output Characteristics V_{DS}- I_{DS} (b) Transfer Characteristics V_{GS} - I_{DS}. The field effect mobility was estimated from the slope of linear part of V_{GS}- I_{DS} curve (inset)

.

10^4. The inset graph of figure 4.19b is the same drain current plot on a linear scale, the slope of which is used for field effect mobility calculation. The field effect mobility extracted from the linear region slope of I_D-V_{GS} plot was 1.4×10^{-2} $cm^2V^{-1}s^{-1}$. The threshold voltage V_T, estimated by extrapolating the straight line to the V_{GS} axis, was -15.08 V. The negative threshold voltage indicates the enhancement mode operation of the device. A maximum sub threshold voltage swing of 3.3 V/dec obtained from the transfer curve of the devices.

4.5 Conclusion

p-Type copper oxide thin films were deposited at room temperature by RF-magnetron sputtering at different oxygen partial pressure. Structural, optical and electrical properties of these films were studied as a function of oxygen partial pressure. Transparent flexible pn heterojunction fabricated in the structure PET/ITO/n-ZnO/p-CuO show

rectifying behaviour. Transparent p-type TFTs with CuO channel layer were fabricated at room temperature. From the XRD and XPS data, it was confirmed the Cu_2O and CuO phase. Band gap of the Cu_2O and CuO channel layer were 2.1 eV and 1.50 eV respectively which is relatively low as compared to n-type TCOs. Band gap of copper oxide films could be enhanced by doping with elements like boron, chromium etc, which effectively reduces the dimension of cross linking of Cu ions. The bottom gate structured p-channel CuO TFTs exhibited an on/off ratio of 10^4 and the field-effect mobility of 0.01 $cm^2\ V^{-1}s^{-1}$. TFT fabricated on Si substrate with Cu_2O channel layer exhibited an on/off ratio 10^4 and field effect mobility 1.31 $cm^2V^{-1}s^{-1}$ which was the highest mobility obtained so far for a copper oxide TFT fabricated using room temperature RF magnetron sputtering followed by post deposition annealing at relatively low temperature of 150 ^oC in air. Lithographically pattered source and drain may give better mobility for a TFT as compared to the shadow mask. The low temperature process along with the better electrical performance and transparency of the devices at this stage will contribute for the development of p-type oxide-based devices and allowing their use in flexible, low cost and transparent electronic circuits.

Chapter 5

Growth of p-type amorphous $Cu_{1-x}B_xO_{2-\delta}$ and $Cu_{1-x}Cr_xO_{2-\delta}$ thin films by RF mangetron co-sputtering and their application for thin film transistors

5.1 Introduction

Amorphous transparent conducting oxides are becoming the material of choice for optoelectronic applications in numerous devices such as photovoltaics, flat-panel displays, invisible security circuits and heat reflectors [45, 46, 188]. Doped versions of TCOs such as ZnO_{1-x}, ZnO

: In/Al/F/B/Ga, In_{1-x} Sn_xO_3 and SnO_2 : F, Cd_2: SnO_4 are all n-type materials, but there are a few reports on p-type TCOs. Sato et al [59], made the first report on p-type TCO films of NiO in 1993 with low transmission in visible range. The design of p-type TCOs needs modification of the energy band structure to reduce the Coulomb force exerted by the oxygen ions on holes. This realization motivated the discovery of a group of transparent p -type Cu delafossites such as $CuMO_2$ (M =Al,Ga, In [82, 98, 273] and $SrCu_2O_2$ [274]. Kawazoe et al [273] first reported p-type transparent conducting thin films of $CuAlO_2$ in 1997. Hosono et al [68] tended the possibility of combining the valence band features of Cu_2O with the larger band gaps of other binary oxides was an attracting method of developing p-type TCOs. Among the delafossite structure oxides, $CuCrO_2$ has a resistivity of the order of 1 Ωcm, and upon doping with 5% Mg the resistivity can be lowered to 0.045 Ωcm, which is the lowest resistivity in the delafossite systems [93]. A study by Snure and Tiwari has identified delafossite $CuBO_2$ as a new p-type TCO [275]. Thin films of $CuBO_2$ display an appreciable room temperature electrical conductivity of 1.65 S cm^{-1}, and a direct optical band gap of 4.5 eV. Hence $CuBO_2$ is considered a potential system in delafossite group. Santra et al [276] in 2012, reported a new cost effective sol-gel technique to synthesize $CuBO_2$ nanopowders and examined the structural properties by x-ray powder diffraction studies.

Tiago etal [309] applied a global structural prediction algorithms to get the ground-state structure of $CuBO_2$. Structural predction have proved that the true ground state $CuBO_2$ is certainly not the delafossite structure and it is a low symmetry monoclinic structure, composed of alternating planar Cu layers with fourfold coordination and

BO_2 networks in which B has threefold coordination. The proposed monoclinic structure of $CuBO_2$ is shown in the figure 5.1. Further for application in flexible displays it is desirable to get room temperature deposited transparent semiconducting thin films [101, 195–198].

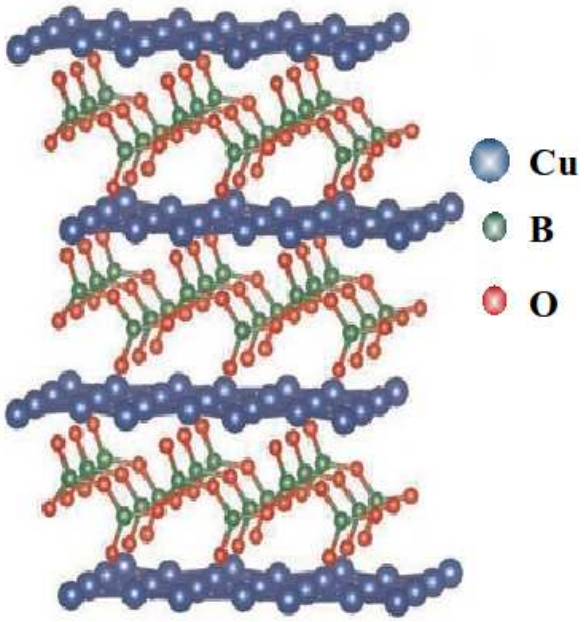

Figure 5.1: Monoclinic crystal structure of $CuBO_2$ proposed by Tiago etal [309].

Conduction mechanism in dellafosste structure is already explained in the chapter one. The role of the M ion in delafossite TCOs on the mobility of holes is widely discussed topic [93]. The lower hole mobilities in p-type delafossites as compared to Cu_2O may be due to the lack of Cu-O-Cu linkages as seen in Cu_2O. In the delafossite structure

there are only Cu-O-M-O-Cu linkages. Higher conductivities observed for $CuCrO_2$ may be because of favorable mixing with the 3d states on the M cation in the Cu-O-M-O-Cu linkages which may reduce the barrier for polaron hopping over the O-M-O layers. Conductivity in delafossite TCOs is a complex issue, with both size and electronic structure of the M ion being significant. According to Scanlon [310] factors effecting the conductivity of delafossite are (1) the M ion not being too big and thus not limiting the hole hopping (2) the M ion having a favorable electronic structure, which can increase the mobility of holes and (3) the M ion not being too small and limiting the dopability of the material. $CuCrO_2$ is currently the leading material, having a favorable electronic structure, and an M ion big enough to let doping and small enough to not restrict hopping [310].

This chapter is divided into two sections. First section deals with the growth and characterisation of stable p-type copper boron oxide thin films at room temperature by RF magnetron co-sputtering and the fabrication of a pn heterojunction using p-type $Cu_{1-x}B_xO_{2-\delta}$ and n-type silicon . The second section deals with the development of p type $Cu_{1-x}Cr_xO_{2-\delta}$ thin films at room temperature by RF magnetron sputtering and fabrication of TFTs using $Cu_{1-x}Cr_xO_{2-\delta}$ as a channel layer.

5.2 Growth and characterisation of $Cu_{1-x}B_xO_{2-\delta}$ thin films

5.2.1 Experimental

p-Type transparent conducting $Cu_{1-x}B_xO_{2-\delta}$ thin films were successfully grown by RF magnetron co- sputtering at room temperature, using two metallic sputtering targets of Cu and B (99.999% pure, 2 inch dia). Depositions were carried out in a controlled atmosphere of oxygen and argon to favor the formation of $Cu_{1-x}B_xO_{2-\delta}$ phase. During sputtering RF power given to Cu target was fixed at 60 W and RF power to Boron target was varied from 50 to 150 W. Substrate was rotated at a speed of 200^o/s. After reaching the base vacuum of 10^{-6} mbar, argon and oxygen is fed to the chamber at a flow rate of 50 sccm and 4 sccm respectively keeping the total sputtering pressure constant at 2.5 $\times 10^{-2}$ mbar.

Glancing angle x-ray diffraction analysis of the films was performed with PANalytical XPert PRO system. The thicknesses of the thin films were measured by a stylus profiler (Dektak 6 M). Composition of the thin film was studied using XPS analysis [Kratos Analytical AMICUS spectrometer fitted with the Mg Kα /Al Kα dual anode x-ray source]. Surface morphology of the film was studied by Agilent 5500 series atomic force microscopy(AFM) in non contact mode. Optical transmittance measurements were performed with Jasco V-570, UV-vis-NIR spectrophotometer. Transport properties of the charge carriers were studied by Hall effect measurement in the van der Pauw geometry (Ecopia, HMS-3000).The current voltage characteristics of pn junction were performed at room temperature using an keithley

4200 Semiconductor analyser.

5.2.2 Result and discussion

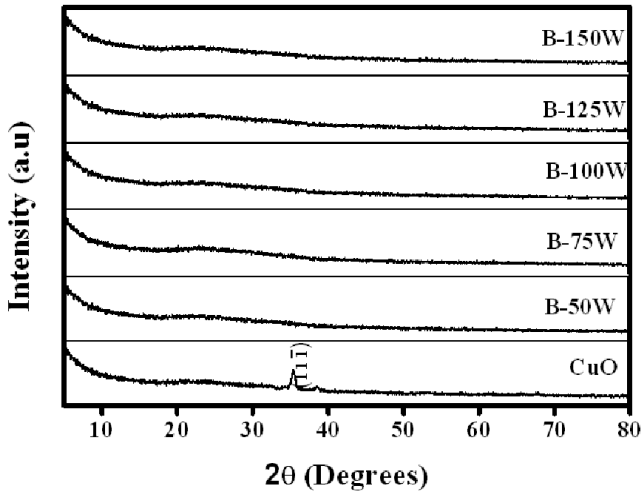

Figure 5.2: X-ray diffraction patterns of $Cu_{1-x}B_xO_{2-\delta}$ thin films prepared by co-sputtering technique. RF power to the boron target is varied keeping the RF power to the Cu target at 60 W.

Deposition conditions for the formation of Cu_2O and CuO thin films were investigated by varying the oxygen partial pressure [Opp = $(\frac{Po_2}{Po_2+P_{Ar}})\times 100$] in the chamber. Growth parameters for the formation of CuO thin film by rf sputtering of Cu are 60 W RF power and 7.4% O_{pp} as described in the chapter 4. All the diffraction peaks of the CuO thin film were in line with the reported ICDD (80-1916) data of CuO. Choosing the same growth parameters, boron content is gradually increased in the CuO films by increasing the RF power given to boron sputtering target keeping the RF power to Cu constant

at 60 W, resulting the $Cu_{1-x}B_xO_{2-\delta}$ thin films. Figure 5.2 shows the glancing angle x-ray diffraction (GXRD) patterns of room temperature deposited copper boron oxide thin films deposited for 30 minutes by varying the RF power (50 - 100 W). For the $CuBO_2$ delafossite films high temperature deposition of the film is required for the formation of crystalline phase. Since all the depositions are carried out at the room temperature amorphous $Cu_{1-x}B_xO_{2-\delta}$ films are obtained. The absence of individual peaks of CuO and B_2O_3 in co-sputtered film suggest that the film is $Cu_{1-x}B_xO_{2-\delta}$.

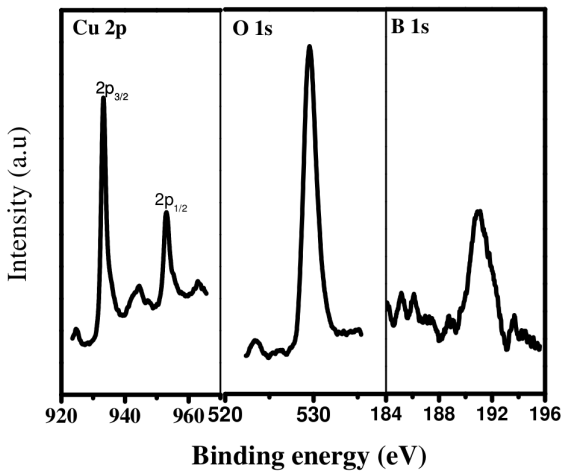

Figure 5.3: XPS core level spectra of $Cu_{1-x}B_xO_{2-\delta}$ thin films prepared at 100 W RF power to boron target.

Compositional analysis of $Cu_{1-x}B_xO_{2-\delta}$ films were carried out by XPS measurement. The boron content in the film was varied by changing the RF power applied to the boron target keeping a fixed RF power to Cu target. XPS core level spectra of $Cu_{1-x}B_xO_{2-\delta}$ thin films pre-

Table 5.1: Atomic percentages of Cu, B, and O of $Cu_{1-x}B_xO_{2-\delta}$ films from XPS

RF-power[Cu] (W)	RF-power [B] (W)	Atomic % (Cu)	Atomic % (B)	Atomic % (O)
60	75	34.84	0.17	64.64
60	100	34.41	9.13	56.46
60	150	32.51	12.48	55.05

pared at 100 W RF power for boron target is shown in the figure 5.3.

The XPS spectrum shows Cu $2p_{1/2}$ peak at 952.3 and Cu $2p_{3/2}$ peak at 933.2 eV. For Cu^{2+} and Cu^{1+} bonded to oxygen the binding energy peaks of $2p_{3/2}$ occur at 933.4 and 932.4 eV respectively. This suggests that Cu is in the 2^+ oxidation state in the $Cu_{1-x}B_xO_{2-\delta}$. Scans show the B 1s peak at 191.4 eV and, which matches with the B^{3+} 1s peak and for oxygen binding energy peak obtained at 529.5 eV. Atomic percentage of each element in various $Cu_{1-x}B_xO_{2-\delta}$ films deposited by varying the RF power of the Boron target is shown in the table 5.1. Composition of the $Cu_{1-x}B_xO_{2-\delta}$ film can be varied by tuning the RF power applied to the sputtering targets.

Surface morphology of the $Cu_{1-x}B_xO_{2-\delta}$ thin films were studied by AFM measurements. Figure 5.4 shows three dimensional AFM pictures of $Cu_{1-x}B_xO_{2-\delta}$ thin films deposited by varying the RF power to the boron target. As deposited films are smooth with rms roughness 1.29 nm, 1.38 nm, 1.05 nm ,0.87 nm, for the films deposited at 75 W, 100 W, 125 W and 150 W respectively.

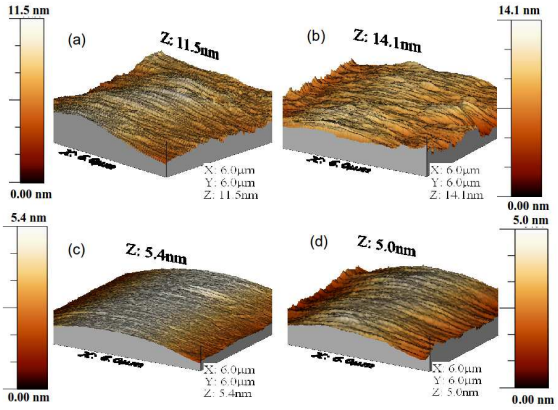

Figure 5.4: AFM images of $Cu_{1-x}B_xO_{2-\delta}$thin films deposited at RF power (a) 75 W (b) 100 W (c) 125 W and (d) 150 W to the boron target.

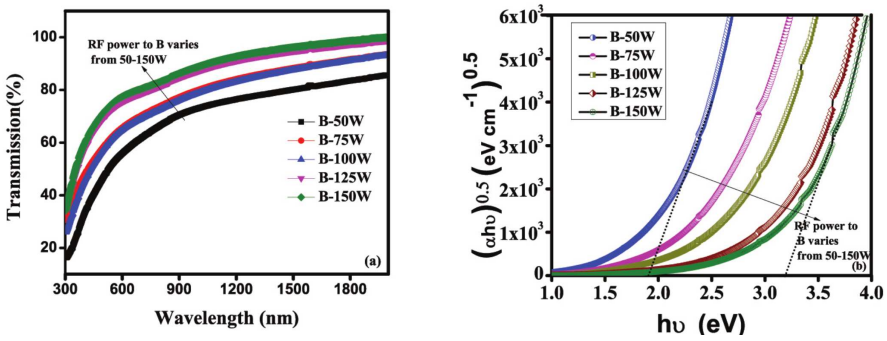

Figure 5.5: (a) Variation of Transmission spectra and (b) Variation of band gap (right side) of $Cu_{1-x}B_xO_{2-\delta}$ with the atomic percentage of boron

Optical transmittance of as deposited CuO films were very poor in the visible region. Optical transmittance was found to increase with atomic percentage of boron in $Cu_{1-x}B_xO_{2-\delta}$ films (5.5a). Band gap of $Cu_{1-x}B_xO_{2-\delta}$ films thin films were estimated from the tau plot of $(\alpha h\nu)^{0.5}$ versus $h\nu$. Band gap of as deposited $Cu_{1-x}B_xO_{2-\delta}$ thin films

(figure 5.5)b was found to vary from 1.6 eV to 3.2 eV with increase in boron content. Figure 5.6 represents variation of transmission % at wavelength 600 nm and variation of band gap of $Cu_{1-x}B_xO_{2-\delta}$ thin films with RF power given to the boron target. The low band gap in CuO is because of the three dimensional interactions between $3d^{10}$ electrons of the neighbouring Cu ions. The boron content in the $Cu_{1-x}B_xO_{2-\delta}$ thin film effectively reduces the dimensions of cross linking of Cu ions. Hence by increasing the boron content, the bang gap of $Cu_{1-x}B_xO_{2-\delta}$ thin films could be enhanced. The theoretical investigations predicts that the band gaps of $CuMO_2$ should increase with the decrease in the ionic radius of M. According to these predictions $Cu_{1-x}B_xO_{2-\delta}$ should have the larger band gap and hence better transmission characteristics [311, 312].

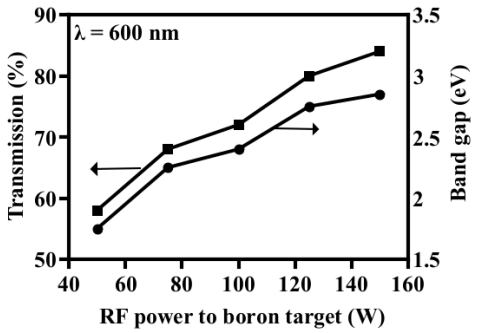

Figure 5.6: Variation of transmission % at wavelength 600 nm and band gap variation $Cu_{1-x}B_xO_{2-\delta}$ thin films with RF power given to the boron target.

In the present study as deposited $Cu_{1-x}B_xO_{2-\delta}$ films have shown positive Hall coefficient consistently. Carrier concentration and mobility values obtained for $Cu_{1-x}B_xO_{2-\delta}$ films from the Hall measurement for films deposited by varying the atomic percentage of boron is shown

in the figure 5.7a. Carrier concentration of the film was found to decrease with the increase in the percentage of boron. Hall mobility of $Cu_{1-x}B_xO_{2-\delta}$ films increases with the increase in the boron percentage.

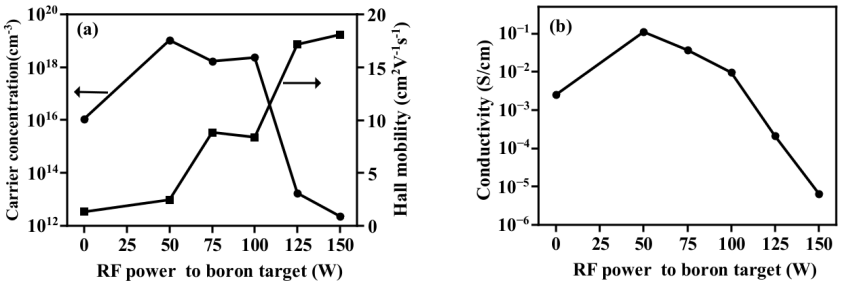

Figure 5.7: (a) Variation in the mobility and carrier concentration of $Cu_{1-x}B_xO_{2-\delta}$ films deposited at various RF power to boron sputtering target. (b) Variation of conductivity of $Cu_{1-x}B_xO_{2-\delta}$thin films with RF power to boron target.

Conductivity of films were measured by four probe technique in van der Pauw configuration. Variation in the conductivity of $Cu_{1-x}B_xO_{2-\delta}$ films as a function of boron percentage is shown in the figure 5.7b. Maximum conductivity of 0.11 S/cm was obtained for films deposited at 50 W RF power for B which is very low value as compared to conductivity reported by Snure et al [275]. p-Type conductivity arises in delafossite like materials is due to excess oxygen or metal deficit with in the crystalline site of the material [278]. In the present study during deposition oxygen partial pressure remain constant and RF power to boron was increased so as to increase the boron content in the film. Hence oxygen content in the films was decreased with the increase in boron content. A neutral oxygen vacancy can generate electrons to the system or compensate holes [236]. Oxygen deficiency occurred in

the film on increasing the boron content may be the possible reason for lowering the conductivity.

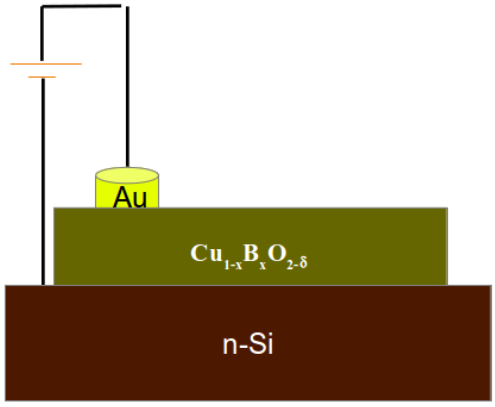

Figure 5.8: Schematic diagram of pn hetrojunction using n-type Si and p-type $Cu_{1-x}B_xO_{2-\delta}$.

A pn heterojunction was fabricated using n-Si and p-$Cu_{1-x}B_xO_{2-\delta}$ layer in a structure of n-Si/p-$Cu_{1-x}B_xO_{2-\delta}$ /Au (figure 5.8) . n-Type silicon substrate was used for the fabrication of the pn junction. The $Cu_{1-x}B_xO_{2-\delta}$ p-layer (150 nm) was deposited through shadow mask by the co-sputtering of Cu (60 W) and B(150 W) targets at oxygen partial presssure 7.4%, for 30 minutes with target to substrate distance 10 cm. Area of the pn junction was 0.07 cm^2. The I-V characteristics of the junction measured using keithley 4200-SCS, is shown in figure 5.9a. The I-V characteristics shows a typical rectifying behavior. The turn on voltage of 0.9 V is obtained for the junction. The maximum forward to reverse current ratio is 51 at 2 V. The figure inset shows the I-V characteristics of Au-$Cu_{1-x}B_xO_{2-\delta}$ contact which indicates

the ohmic nature. Hence figure 5.9a shows the J-V characteristics origintated from Si/$CuBO_x$ junction. The diode equation is $I = I_0 \exp(\frac{eV}{nkT}\text{-}1)$, where I_0 is the maximum reverse current, e is the electronic charge, V is the voltage for the current I, k is the Boltzmann constant, T is the temperature, and n is the ideality factor. For ideal diodes n varies between 1 and 2. From the plot lnI versus V (figure 5.9b), at very small voltages the ideality factor is 2.34 and at higher voltages it is 76. The high value of ideality factor can be attributed to poor interface and defects at the interface. According to Wang et al, the heterojunction diode can be modeled in different bias ranges by a series of diode and resistance [313]. The ideality factor of the device is the sum of ideality factors of the individual junction and may lead to ideality factor much greater than two [226–229, 314].

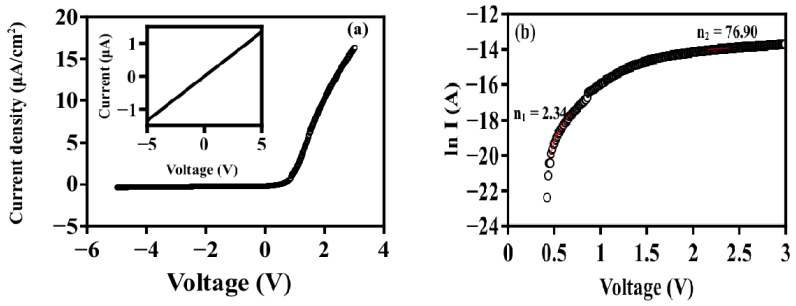

Figure 5.9: (a) I-V characteristics of n- Si/p-$Cu_{1-x}B_xO_{2-\delta}$ heterojunction and Au/$Cu_{1-x}B_xO_{2-\delta}$ contact (inset). (b) Plot between voltage and lnI.

5.2.3 Conclusion

Transparent p-type amorphous $Cu_{1-x}B_xO_{2-\delta}$ thin films were grown on the glass substrate by RF magnetron co- sputtering at room tem-

perature. Structural, optical and electrical properties of these films were studied as a function of boron content in the film. Amorphous structure of as deposited films were confirmed by GXRD. Compositional analysis was carried out by XPS measurement and surface morphology of synthesized samples was characterised by atomic force microscopy. Band gap of as deposited $Cu_{1-x}B_xO_{2-\delta}$ thin films varies from 1.8 eV to 3.2 eV as boron content increases in the film. Positive Hall coefficient obtained for all the film confirm the p-type conductivity in $Cu_{1-x}B_xO_{2-\delta}$. pn Heterojunction fabricated in the structure n-Si/p$Cu_{1-x}B_xO_{2-\delta}$/Au show rectifying behaviour. The $Cu_{1-x}B_xO_{2-\delta}$ films grown can be used as the channel layer for transparent thin film transistor and in various industrial applications such as a solar-electric energy conversion device and as chemical sensor element.

5.3 Growth of p-type transparent conducting $Cu_{1-x}Cr_xO_{2-\delta}$ thin films and fabrication of thin film transistors

$CuCrO_2$ has been potential candidate of recent interest as a further p-type TCO. It exhibits appreciable transparency in the visible region contrary to the fact that there must be dipole forbidden 3 d-3 d excitations focused on Cr in the visible region. Undoped $CuCrO_2$ is a high resistive p-type semiconductor. Replacing the trivalent Cr with divalent dopants (e.g. Mg, Ca, Ni) leads to a significant hike in conductivity [93, 277, 279–282]. This enhancement in conductivity has been connected to CuI /CuII [283, 284] and to CrIII/CrIV hole mechanisms [285]. The focus on $CuCrO_2$ as an optimum p-type transparent semi-

conducting oxide has directed to a large interest in developing thin films. Pulsed laser deposition (PLD) was the most popular growth technique [286–289]. RF magnetron sputtering, chemical vapour deposition and sol gel techniques also employed for the deposition $CuCrO_2$ thin films [93, 290–292]. Shin et al [293] have developed $CuCrO_2$ thin films by molecular beam epitaxy and electronic structure of the films were investigated. Li et al [286] reported the micro structural, electrical and optical properties of $CuCrO_2$ films prepared by PLD. They have fabricated the PLD target by solgel method and high substrate temperature (800 K) was employed to get crystalline phase of copper chromium oxide. The transparent pn junction of p-$CuCrO_2$/n-ZnO and $CuCrO_2$:Mg/ZnO have been fabricated by Chiu et al [294, 295]. Han et al [296] made a detailed study on structural, electronic band transition and optoelectronic properties of delafossite $CuGa_{1-x}Cr_xO_2$ solid solution films were grown by sol-gel method. Recently, $CuCrO_2$ are attracting wide interest as a promising semiconductor materials for a range of applications other than TCO applications. unusual magnetic properties and multiferroic properties $CuCrO_2$ were investigated [279, 297–302] $CuCrO_2$ has also been used as photocatalyst for hydrogen evolution, ozone sensing material, and as a thermo electric material [281, 285, 303–305]. Antibacterial properties of $CuCrO_2$ thin films were investigated by Te-Wei Chiu etal [306] for E. coli bacteria. Magneto resistance of highly crystalline $CuCrO_2$ thin films deposited by PLD technique was studied by Sullivan et al [307]. In the present study $Cu_{1-x}Cr_xO_{2-\delta}$ thin films grown by co- sputtering technique have been demonstrated for the first time as a channel layer for fabrication of thin film transistors.

5.3.1 Experimental

p-Type transparent conducting $Cu_{1-x}Cr_xO_{2-\delta}$ thin films were successfully grown by RF magnetron co-sputtering at room temperature, using two metallic sputtering targets of Cu and Cr (99.999% pure, 2 inch dia). Depositions were carried out in a controlled atmosphere of oxygen and RF power given to Cu target was fixed at 60 W and RF power given to Cr was varied from 100 to 250 W. Substrate was rotated at a speed of 200^o/s. After reaching the base vacuum of 10^{-6} mbar, argon and oxygen is fed to the chamber at a flow rate of 50 sccm and 4 sccm respectively keeping the total sputtering pressure constant at 2.5 $\times 10^{-2}$ mbar.

Glancing angle x-ray diffraction analysis of the films was performed with PANalytical XPert PRO system. The thicknesses of the thin films were measured by a stylus profiler (Dektak 6 M). Surface morphology of the film was studied by Agilent 5500 series atomic force microscopy (AFM) in non contact mode. Optical transmittance measurements were performed with Jasco V-570, UV-vis-NIR spectrophotometer. Transport properties of the charge carriers were studied by Hall effect measurement in the van der Pauw geometry (Ecopia, HMS-3000). The current voltage characteristics of pn junction were performed at room temperature using an keithley 4200 Semiconductor analyzer.

5.3.2 Results and discussion

Deposition conditions for the formation of Cu_2O and CuO thin films were investigated by varying the oxygen partial pressure [Opp $= (\frac{Po_2}{Po_2+P_{Ar}}) \times$ 100] in the chamber as discussed in chapter4. Choosing the same growth parameters for the formation of CuO phase (60 W RF power

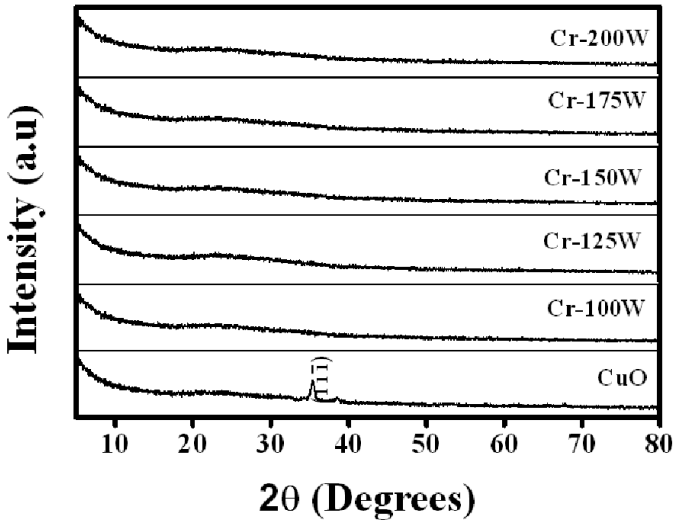

Figure 5.10: X-ray diffraction patterns of $Cu_{1-x}Cr_xO_{2-\delta}$ thin films prepared by varying the RF power to the chromium target. RF power to the Cu was fixed at 60 W for entire deposition.

and 7.4% Opp), chromium content is gradually increased in the CuO films by sputtering chromium at various RF power keeping the RF power to Cu constant at 60 W, resulting the $Cu_{1-x}Cr_xO_{2-\delta}$ thin films. Figure 5.10 shows the glancing angle x-ray diffraction (GXRD) patterns of room temperature deposited copper chromium oxide thin films deposited by varying the RF power (100 - 225 W) for 30 minutes. High temperature deposition of the film is required for the formation of $CuCrO_2$ delafossite structure. Since all the depositions were carried out at the room temperature amorphous $Cu_{1-x}Cr_xO_{2-\delta}$ films were obtained. The absence of individual peaks of CuO in co-sputtered film suggest that the film is $Cu_{1-x}Cr_xO_{2-\delta}$. Compositional analysis of $Cu_{1-x}Cr_xO_{2-\delta}$ films were carried by XPS measurement.The chromium

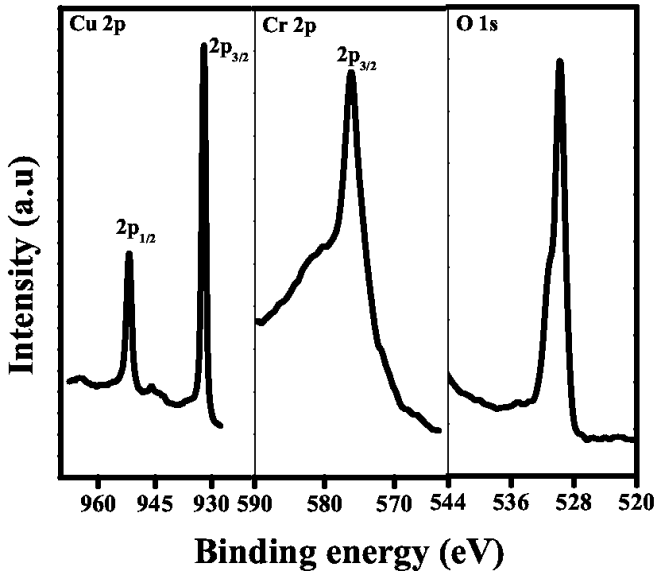

Figure 5.11: XPS core level spectra of $Cu_{1-x}Cr_xO_{2-\delta}$ thin films prepared at 100 W RF power to chromium target.

content in the film was varied by changing the RF power applied to the chromium target keeping a fixed RF power to Cu target. XPS core level spectra of $Cu_{1-x}Cr_xO_{2-\delta}$ thin films prepared at 100 W RF power for chromium target is shown in the figure 5.3. The XPS spectrum shows Cu $2p_{1/2}$ peak at 952.3 and Cu $2p_{3/2}$ peak at 932.2 eV. This suggests that Cu is in the 1^+ oxidation state in the $Cu_{1-x}Cr_xO_{2-\delta}$. The Cr $2p_{3/2}$ peaks shown in figure 5.11 is located at 576.44 eV which is in line with the literature reports for Cr^{3+} [308] and for oxygen binding energy peak obtained at 529.9 eV. Atomic percentage of each element in various $Cu_{1-x}Cr_xO_{2-\delta}$ films deposited by varying the RF power of the chromium target is shown in the table 5.2. Composition of the $Cu_{1-x}Cr_xO_{2-\delta}$ film can be varied by changing the RF power

Table 5.2: Atomic percentages of Cu, Cr, and O of $Cu_{1-x}Cr_xO_{2-\delta}$ films from XPS

RF-power[Cu] (W)	RF-power [Cr] (W)	Atomic % (Cu)	Atomic % (Cr)	Atomic % (O)
60	100	35.73	19.01	45.25
60	125	39.30	21.12	39.58
60	150	41.09	23.47	35.44

applied to the sputtering targets.

Surface morphology of the $Cu_{1-x}Cr_xO_{2-\delta}$ thin films were studied by AFM measurements. Figure 5.12 shows three dimensional AFM images of $Cu_{1-x}Cr_xO_{2-\delta}$ thin films deposited by varying the RF power to the chromium target. As deposited films are smooth with rms roughness 1.29 nm, 1.18 nm ,1.31 nm, 0.86nm, 0.56 nm, 1.36 nm for the films deposited at 100 W, 125 W, 150 W, 175 W, 200 W, 225 W respectively.

All the as deposited $Cu_{1-x}Cr_xO_{2-\delta}$ films have shown positive Hall coefficient consistently. Carrier concentration and mobility values obtained from the Hall measurement for films deposited by varying the atomic percentage of chromium is shown in the figure 5.13a. Carrier concentration and the mobility of the film was found to increase with the increase in the percentage of chromium and maximum values were obtained at 175 W chromium power. Further increase in the chromuim percentages cause a gradual decrease in both carrier concentration and mobility. Conductivity of films were measured by four probe technique in van der Pauw configuration. Variation in the conductivity of $Cu_{1-x}Cr_xO_{2-\delta}$ films as a function of chromium percentage is shown in

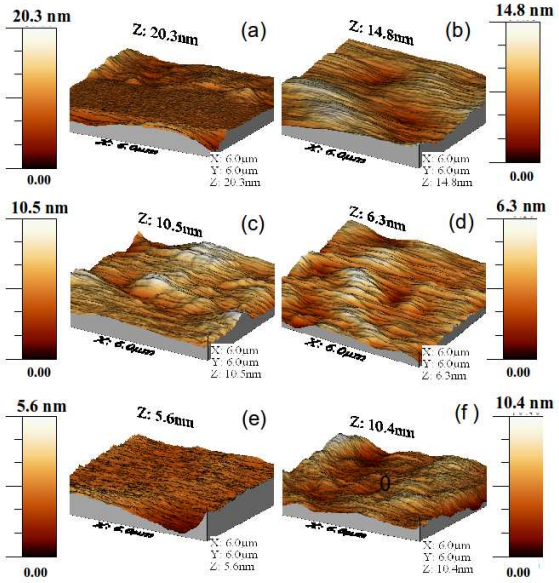

Figure 5.12: AFM images of $Cu_{1-x}Cr_xO_{2-\delta}$thin films deposited at RF power (a) 100 W (b) 125 W (c) 150 W and (d)175 W (e) 200 W (f) 225 W to the chromium target.

the figure 5.13b. Maximum conductivity of 0.71 S/cm was obtained for films deposited at 175 W RF power for chromium. In the present study during deposition oxygen partial pressure remain constant and RF power to chromium was increased so as to vary the chemical composition of the film. Hence oxygen content in the films was decreased with the increase in chromium content. Oxygen deficiency occurred in the film on increasing the chromium content may be the possible reason for lowering the carrier concentration and conductivity.

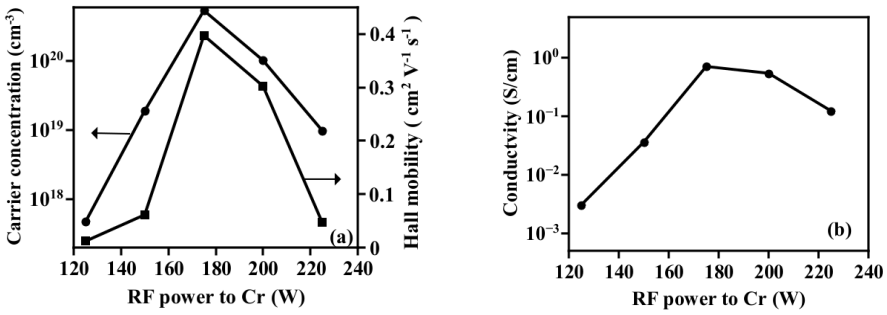

Figure 5.13: (a) Variation in the mobility and carrier concentration of $Cu_{1-x}Cr_xO_{2-\delta}$ films deposited at various RF power to chromium sputtering target. (b) Variation of conductivity of $Cu_{1-x}Cr_xO_{2-\delta}$thin films with RF power to chromium target.

Optical transmittance of as deposited CuO films were very poor in the visible region. Optical transmittance could be increased by adding small percentage chromium in to CuO film. Transmittance of $Cu_{1-x}Cr_xO_{2-\delta}$ thin films was found to decrease with the atomic percentage of chromium(figure 5.14a). Figure 5.14b shows the variation of percentage of transmission at wave length 600 nm for $Cu_{1-x}Cr_xO_{2-\delta}$ with RF power given to Cr sputtering target. Band gap of $Cu_{1-x}Cr_xO_{2-\delta}$ thin films were estimated from the tau plot of $(\alpha h\nu)^{0.5}$ versus $h\nu$. The plot of $(\alpha h\nu)^{0.5}$ vs energy $h\nu$ for $Cu_{1-x}Cr_xO_{2-\delta}$ thin films deposited at different RF power to Cr is shown in the figure figure 5.15a. Band gap variation of $Cu_{1-x}Cr_xO_{2-\delta}$ with RF power given to Cr is given in the figure 5.15b. Band gap of as deposited $Cu_{1-x}Cr_xO_{2-\delta}$ thin films calculated from the tau plot was varying from 2.8 eV to 2.1 eV as the chromium content increase. Increase in the chromium content led to the oxygen deficient and amorphous $Cu_{1-x}Cr_xO_{2-\delta}$ thin films. Tail states extended to the band gap due to the defects and non stoichiometry may be the possible reason for lowering the band gap with increase

in the chromium content in the $Cu_{1-x}Cr_xO_{2-\delta}$ thin films. Thin film deposition at higher oxygen partial as well as post deposition annealing can reduce the oxygen deficiency issue experienced in the present study and hence enhance the band gap greater than 3 eV.

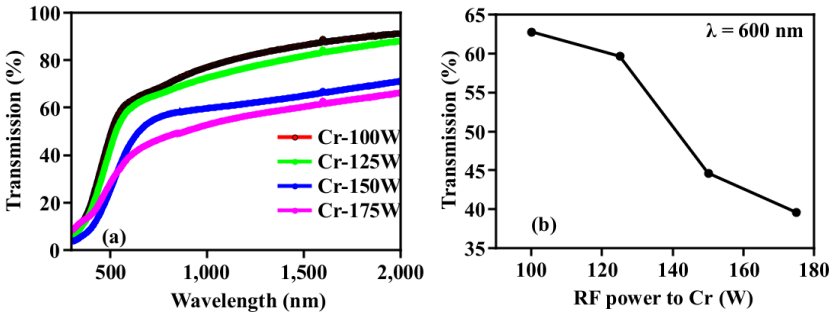

Figure 5.14: (a) Transmission spectra of $Cu_{1-x}Cr_xO_{2-\delta}$ with the atomic percentage of chromium and (b) Variation of transmission (%) at 600 nm with RF power given to Cr

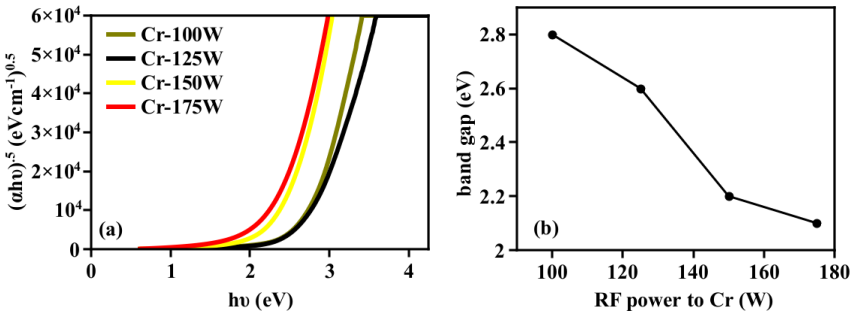

Figure 5.15: (a) The plot of $(\alpha h\nu)^{0.5}$ vs energy $h\nu$ for $Cu_{1-x}Cr_xO_{2-\delta}$ thin films (b) Variation of band gap of $Cu_{1-x}Cr_xO_{2-\delta}$ with the atomic percentage of chromium

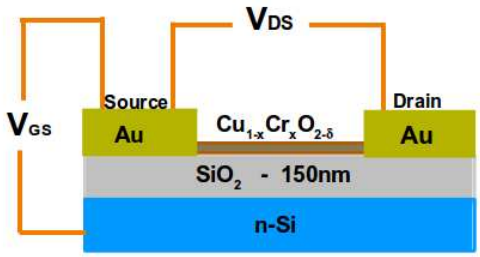

Figure 5.16: Schematic diagram of TFT using p-type $Cu_{1-x}Cr_xO_{2-\delta}$ as channel layer.

5.3.3 Fabrication of $Cu_{1-x}Cr_xO_{2-\delta}$ thin film transistors

The bottom gate structures of TFT fabricated in this study is shown in the figure 5.16. A silicon substrate deposited with 200 nm thick layer of SiO_2 was used for TFT fabrication. n-type silicon substrate acts as the TFT gate and SiO_2 layer act as gate insulator. $Cu_{1-x}Cr_xO_{2-\delta}$ thin films with three different composition were used as a the channel layer for TFT fabrication. Composition of the $Cu_{1-x}Cr_xO_{2-\delta}$ channel layer was varied by varying the RF power to the chromium target (100 W, 125 W, 150 W), keeping the power to copper target at 60 W during the co-sputtering. Depositions were carried out at room temperature, in a controlled atmosphere of oxygen and argon to favor the formation of $Cu_{1-x}Cr_xO_{2-\delta}$ phase. Base pressure of the chamber was 7 $\times 10^{-6}$mbar. Target to substrate distance was kept constant at 10 cm and deposition time was 5 minutes for all depositions. Argon flow rate to the chamber was 50 sccm for entire deposition while oxygen flow rate was 4 sccm . Oxygen flow percentage [Opp = $(\frac{Po_2}{Po_2+P_{Ar}})\times$ 100] to the chamber during deposition of channel layer was 7.40%.

By knowing the deposition rate channel thickness could be controlled by deposition time. Thickness estimated for the channel layers were 22 nm, 27 nm and 33 nm for $Cu_{1-x}Cr_xO_{2-\delta}$ films deposited at RF power 100 W, 125 W and 150 W given to the chromium target. After the deposition of channel layer substrates were annealed at 150 ^oC in air for 20 minutes. The source and drain electrodes were deposited by thermal evaporation of gold through shadow mask. The channel width and length were 2500 μm and 60 μm, respectively.

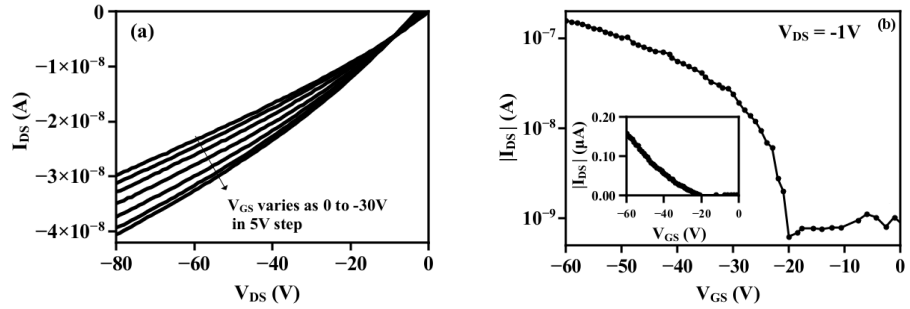

Figure 5.17: (a) Output characteristics V_{DS}- I_{DS} of $Cu_{1-x}Cr_xO_{2-\delta}$ TFT deposited with 100 W RF power to Cr sputtering target. (b) Transfer Characteristics V_{GS} - I_{DS}. The field effect mobility was estimated from the slope of linear part of V_{GS}- I_{DS} curve (inset).

Figures 5.17a, 5.18a, 5.19a shows the drain current - drain voltage (I_{DS}-V_{DS}) characteristics of the transistors in which channel layer was deposited by co-sputtering with 100 W, 125 W and 150 W RF power to chromium respectively and 60 W RF power to copper. A negative gate voltage was required for all transistors to induce the channel conduction which indicates the enhancement mode operation of p-channel transistor, and the channel conductivity increased with increase of negative gate voltage. Non ideal behaviour of the output

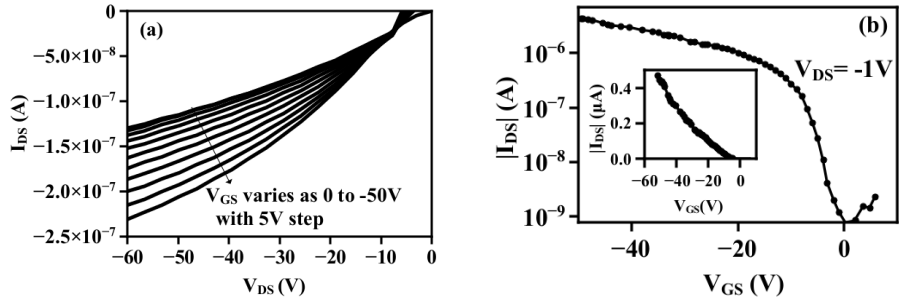

Figure 5.18: (a) Output Characteristics V_{DS}- I_{DS} of $Cu_{1-x}Cr_xO_{2-\delta}$ TFT deposited with 125 W RF power to Cr sputtering target. (b) Transfer Characteristics V_{GS} - I_{DS}. The field effect mobility was estimated from the slope of linear part of V_{GS}- I_{DS} curve (inset)

.

characteristics may be due to either the series resistance of the electrodes or due to the large leakage current [269]. Figure 5.17b shows the transfer characteristics (I_{DS}- V_{GS}) of TFT fabricated with a channel layer $Cu_{1-x}Cr_xO_{2-\delta}$ deposited at 100 W RF power given to Cr sputtering target. The field effect mobility extracted from the linear region slope of I_D-V_{GS} plot was 3.20 $\times$ 10^{-1} $cm^2V^{-1}s^{-1}$ and on-off ratio was 0.7 x 10^4. The threshold voltage V_T, estimated by extrapolating the straight line to the V_{GS} axis, was -9 V. The negative threshold voltage indicates the enhancement mode operation of the device. A maximum sub threshold voltage swing of 3.2 V/dec obtained from the transfer curve of the device. Figure 5.18b shows the transfer characteristics of TFT fabricated with a channel layer $Cu_{1-x}Cr_xO_{2-\delta}$ deposited at 125 W RF power given to Cr sputtering target(I_{DS}- V_{GS}). The device exhibited a field effect mobility 1.35 x 10^{-2} $cm^2V^{-1}s^{-1}$, on-off ratio of 1.5 x 10^2 and sub threshold swing 3.2 V/dec. Figure 5.19b shows the

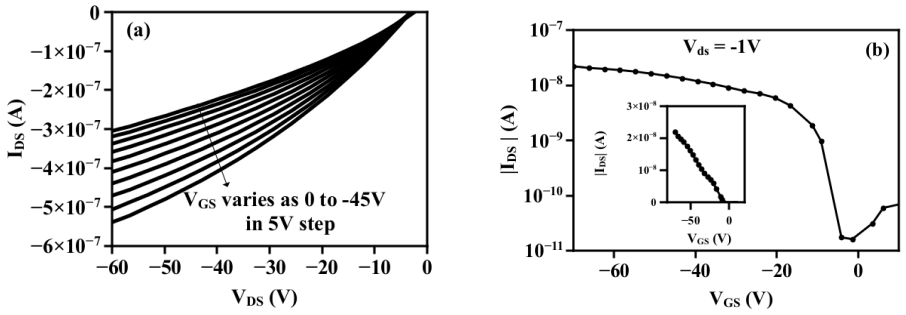

Figure 5.19: (a) Output Characteristics V_{DS}- I_{DS} $Cu_{1-x}Cr_xO_{2-\delta}$ TFT deposited with 150 W RF power to Cr sputtering target. (b) Transfer Characteristics V_{GS} - I_{DS} The field effect mobility was estimated from the slope of linear part of V_{GS}- I_{DS} curve (inset).

transfer characteristics (I_{DS}- V_{GS}) of TFT fabricated with a channel layer $Cu_{1-x}Cr_xO_{2-\delta}$ deposited at 150 W RF power given to Cr sputtering target. The device exhibited a field effect mobility 1.02 x 10^{-3} $cm^2V^{-1}s^{-1}$, on-off ratio of 0.7x10^3 and sub threshold swing 3.3 V/dec.

Table 5.3 gives the comparative study of device performance with the variation of composition of copper chromium oxide channel layer of the TFTs. Better mobility was obtained for the device fabricated with a channel layer deposited by co sputtering of Cu and Chromium target at RF power 60 W and 100 W respectively.

5.3.4 Comparison of transistor performance with the different channel layers(CuO, Cu_2O and $Cu_{1-x}Cr_xO_{2-\delta}$)

In the present study three different p-type thin films (CuO,Cu_2O and $Cu_{1-x}Cr_xO_{2-\delta}$) were developed for the fabrication of TFT. The comparsion of the transistor performance with different channel layers is summarised in the 5.4. From the most of the previous report it is

Table 5.3: Comparison of transistor performance with the composition of $Cu_{1-x}Cr_xO_{2-\delta}$ channel layer

RF-power [Cr](W)	Bandgap (eV)	Mobility ($cm^2V^{-1}s^{-1}$)	V_{th} (V)	on/off ratio)
100 W	2.8	0.32	-9.01V	0.7x10^4
125 W	2.6	0.013	-25V	1.5x10^2
150 W	2.4	0.001	-7.28V	0.7x10^3

Table 5.4: Comparison of transistor performance with the different channel layers

Channel layer	Transmission % of channel layer	Bandgap (eV)	Mobility ($cm^2V^{-1}s^{-1}$)	Threshold voltage (V)	on/off ratio)
CuO	79	1.6	1.4 x 10^{-2}	-15.8 V	0.7x10^4
Cu_2O	81	2.1	1.31	-10.35V	1.5x10^2
$Cu_{1-x}Cr_xO_{2-\delta}$	84	2.8	3.20 x 10^{-1}	-9.01V	0.7x10^3

observed that the copper oxide TFTs exhibit poor field effect mobility and transmission. CuO TFT fabricated in the work shwed a field effect mobility of 1.4 x 10^{-2} $cm^2V^{-1}s^{-1}$ and band gap of CuO channel layer was 1.6 eV. As far as the mobility of the TFT is concerned Cu_2O channel layer is the best candidate for the fabrication of TFT which could exhibit field effect mobility of 1.31 $cm^2V^{-1}s^{-1}$. Band gap of the Cu_2O channel layer was 2.2 eV which have to enhance for a transparent electronic devices. Even though the mobility of $Cu_{1-x}Cr_xO_{2-\delta}$) TFT was lower than that of Cu_2O TFT, Its band gap of the channel layer is 2.8 eV which is more suit for transparent electronics.

5.3.5 Conclusion

Transparent p-type amorphous $Cu_{1-x}Cr_xO_{2-\delta}$ thin films were grown on the glass substrate by RF magnetron co-sputtering at room temperature. Structural, optical and electrical properties of these films were studied as a function of chromium content in the film. Composition of $Cu_{1-x}Cr_xO_{2-\delta}$ thin films could be varied by tuning the RF power to Cr sputtering target. Band gap of as deposited $Cu_{1-x}Cr_xO_{2-\delta}$ thin films varies from 2.8 eV to 2.1 eV as chromium content increases in the film. Positive Hall coefficient obtained for all the film confirm the p-type conductivity in $Cu_{1-x}Cr_xO_{2-\delta}$. The Bottom gate structured TFTs fabricated using p-type $Cu_{1-x}Cr_xO_{2-\delta}$ operated in enhancement mode with an on/off ratio of 10^4 and field effect mobility 0.3 $cm^2V^{-1}s^{-1}$. This is the first report on p-channel $Cu_{1-x}Cr_xO_{2-\delta}$ TFTs which exhibit comparable transistor performance with better optical band gap than Cu_2O channel layer. The $Cu_{1-x}Cr_xO_{2-\delta}$ films grown can be used in various transparent optoelectronic device applications.

Chapter 6

Summary and Scope for further study

6.1 Summary of the present study

Transparent electronics is an emerging science and technology field concentrated on fabricating invisible electronic circuits and optoelectronic devices. Current conventional electronic circuits consist of silicon based semiconductor junctions and transistors.Now it is the time to replace device building block materials, semiconductors electronic contacts and dielectric layers with transparent so as to get transparent circuits. The first goal of such a challenge is to discover and develop transparent high performance electronic materials. the second goal is to their implementation of transistors and circuit structures.

Although the TCOs have a vast range of applications, very little work has been done on active device fabrication using TCOs. This is because most of the all these materials are of n-type in nature and

their use as oxide semiconductors is some what limited due to their monopolarity. In order to extend the use of TCOs to a range of additional applications such as transparent light emitting diodes, UV detectors, solar cells etc. it is important to synthesis p-type TCOs. The possibility of simultaneous transparency and conductivity is is rarer in p-type. The search for high mobility p-type wide-gap semiconductors to substitute these n-type materials has now been a major research thrust. The Tremendous achievement in n-type oxide semiconductors and its TFT application activated the research in p-type oxide based semiconductors that to be applied for TFTs. But to the date there is no report on p-type TFTs having the similar performance with that of n-type oxide TFTs. The low mobility of valance band derived carriers is the main limiting factor of p-channel oxide TFTs.

The focus of the study presented in the thesis is the growth and characterization n of p-type oxide semiconductors for the application of thin film transistors. RF magnetron sputtering techniques was employed for for thin film deposition. Detailed investigation on room temperature deposited p-type oxide thin films : SnO, CuO, Cu_2O, $Cu_{1-x}B_xO_{2-\delta}$, $Cu_{1-x}Cr_xO_{2-\delta}$ are included in this thesis. Co-sputtering technique was utilised for the growing multicomponent p-type oxide thin films. In the present study, two targets were sputtered simultaneously and power was individually controlled by two separate power sources for the depostion of $Cu_{1-x}B_xO_{\ 2-\delta}$, $Cu_{1-x}Cr_xO_{2-\delta}$ thin films. This aided to modulate the chemical composition of the deposited film over a wide range. The grown p-type thin films in the present work have been employed for the fabrication of pn heterojunction and TFTs. we have used both glass, silicon and flexible substrates for the device fabrications. Thermal evaporation technique was used

for the deposition of metal contact to the devices.

p-Type and n-type tin oxide thin films were grown by RF magnetron sputtering at different oxygen partial pressure. Type of the charge carrier of the tin oxide thin films could be varied by tuning the oxygen partial pressure. Room temperature deposited amorphous p-type tin oxide could be crystallised and enhanced the band gap by annealing . Wide band gap of annealed SnO thin films indicate that SnO can be used as better candidate for transparent electronic applications. Transparent pn heterojunction fabricated in the structure glass/ITO/n-ZnO/p-SnO is the first report on heterojunction using p-type SnO. The tin oxide films grown can be used as the channel layer for transparent thin film transistor and in various industrial applications such as a solar-electric energy conversion device and chemical sensor element.

p-Type copper oxide thin films were grown by RF magnetron sputtering at different oxygen partial pressure. Transparent flexible pn heterojunction fabricated in the structure PET/ITO/n-ZnO/p-CuO show rectifying behaviour. Transparent p-type TFTs with CuO channel layer were fabricated at room temperature. The bottom gate structured p-channel CuO TFTs exhibited an on/off ratio of 10^4 and the field-effect mobility of 0.01 $cm^2\ V^{-1}\ s^{-1}$. Cu_2O layer was also employed for the fabrication of TFT in which field effect mobility obtained was 1.34 $cm^2\ V^{-1}\ s^{-1}$ and on /off ratio 10^4. Mobility obtained here is the highest reported mobility for a p-channel Cu_2O TFTs fabricated by RF magnetron sputtering. Three dimensional interaction between $3d^{10}$ electrons of the neighbouring Cu atom reduces the bandgap of copper oxides. Hence doping the copper oxide with elements like Al, Cr, B may effectively reduces the dimension of cross linking of Cu ions

resulting in enhancement optical band gap

Transparent p-type amorphous $Cu_{1-x}B_xO_{2-\delta}$ thin films were grown on the glass substrate by RF magnetron co-sputtering of copper and boron at room temperature in an oxygen atmosphere. Band gap of as deposited $Cu_{1-x}B_xO_{2-\delta}$ thin films could be varied from 1.8 eV to 3.2 eV as boron content increases in the film. The wide band gap $Cu_{1-x}B_xO_{2-\delta}$ thin film is a potential candidate for active device applications. pn Hetero junction fabricated in the structure n-Si/p-$Cu_{1-x}B_xO_{2-\delta}$/Au show rectifying behaviour, which is the first report on heterojunction using p-type copper boron oxide thin films.

Transparent p-type amorphous $Cu_{1-x}Cr_xO_{2-\delta}$ thin films were grown on the glass substrate by RF magnetron co-sputtering at room temperature. The Bottom gate structured TFTs fabricated using p-type $Cu_{1-x}Cr_xO_{2-\delta}$ operated in enhancement mode with an on/off ratio of 10^4 and field effect mobility 0.3 cm^2 V^{-1} s^{-1}. This is the first report on p-channel $Cu_{1-x}Cr_xO_{2-\delta}$ TFTs.

6.2 Scope for further study

Difficulty in controlling the carrier concentration in p-type SnO was main hindrance for the successful functioning of p-channel SnO TFT. Growth parameter for p-channel SnO with lower carrier concentration have to be optimised for the further fabrication of successful TFTs.

Deposition conditions for copper chromium oxide and copper baron oxide has to be optimised to get crystalline films so as to enhance the optical band gap. Since the copper boron oxide is the potential candidate among wide band gap p-type semiconductors, a detailed investigation is required in the field of device fabrication using p-channel

copper boron oxide. Even though we have reported the first TFT using p-channel $Cu_{1-x}Cr_xO_{2-\delta}$, its field effect mobility is less than one. Further study is essential to increase the mobility of $Cu_{1-x}Cr_xO_{2-\delta}$ TFTs. All the p-type oxide thin films described in thesis were grown by room temperature depositions. Hence we could fabricate a pn junction on flexible substrates. But attempts to fabricate TFTs on plastic substrates were not quite successful because of high leakage current through the gate insulator. Hence the proper optimisation of insulator deposition conditions are essential to deposit insulators on plastic substrates which can leads to transparent flexible electronics. Localised states induced by defects or impurities are distributed in the band gap of inorganic amorphous semiconductors. The study of their density and nature is currently attracting much attention in order to understand trap-limited charge transport in amorphous oxide thin-films. Density of states of channel layer can be measured by studying the temperature dependent transistor Characteristics.

Appendix

Appnedix A

A Symbols used in the thesis

Table A1: Symbols used in the thesis

Symbol	Description
a	Primitive cell size
α	Absorption coefficient, inverse localisation length
B	Conduction band width, Magnetic flux density
C_i	Insulator Capacitance
d	Sample thichness
D_{it}	Density of tail states
χ_S	Electron affinity of the semiconductor
e	Elementary electronic charge
E	Energy, Electric field
E_0	Optical gap (Tauc gap)
E_A	Valence band tail edge
E_B	Conduction band tail edge
E_C	Conduction band mobility edge
E_d	Defect state energy
E_F	Fermi energy
E_t	Threshold energy
E_V	Valence band mobility edge
E_U	Urbach energy
ε_0	Permittivity of free space
g_d	Drain conductance
g_m	Drain transconductance

Table A1: ....continued

Symbol	Description
h	Plank's constant
H	Hamiltonian
I	Current
$\overrightarrow{k}$	Wave vector
k	Magnitude of wave vector
Δk	Uncertainty in wave vector magnitude
k_B	Boltzmann's constant
k_{BZ}	Maximum crystal momentum in first Brillouin zone
k_1	Extinction coefficient
l	Mean free path length
L	Channel length, Grain size
λ	Screening length
m	Rest mass of electron
m_e^*	Electron effective mass
M	Mass of nucleus
μ	Conduction electron mobility, Chemical potential
μ_{eff}	Effective mobility
μ_{fe}	Field effect mobility
μ_H	Hall mobility
μ_n	Electron mobility (conductivity measurements)
μ_p	Hole mobility (conductivity measurements)
μ_{sat}	Saturation mobility
n	Electron density, Refractive index
$N(E)$	Electronic density of states
N_F	Electron density at Fermi level

Table A1: ....continued

Symbol	**Description**
$N_v(\nu)$	Vibrational density of states
ν	Photon frequency
ν_{ph}	Phonon frequency
r	Scattering factor
R	Reflectance, Magnitude of position vector
R_H	Hall coefficient
p	Hole density
P	Momentum operator, Probability function
P_{O_2}	Oxygen partial pressure
q	Electronic charge
ϕ_M	Metal work function
ϕ_S	Semiconductor work function
ψ_{Sb}	Band bending at back interface
ψ_{Sf}	Band bending at front interface
S	Subthreshold voltage swing, Sputtering yield
σ	DC electrical conductivity
t	Thin film thickness
T	Absolute temperature, Transmittance
τ	Relaxation time, Collision time
U	Electron correlation energy
U_s	Surface binding energy of atoms
v	Velocity
V	Sample volume
V_a	Applied voltage
V_{GS}	Gate-Source voltage

Table A1: ....continued

Symbol	**Description**
V_H	Hall voltage
V_{DS}	Drain-Source voltage
V_P	Pinch-off voltage
V_{sat}	Saturation drain voltage
V_T	Threshold voltage
W	Channel width

Appendix B

B Abbreviations used in the thesis

Table B1: Abbreviations used in the thesis

Abbreviation	**Expansion**
3D	Three Dimension
a-Si:H	Hydrogenated Amorphous Silicon
AFM	Atomic Force Microscope
AMLCD	Active Matrix Liquid Crystal Display
AOS	Amorphous oxide semiconductor
ATO	Aluminium Titanium Oxide
B	Boron
BCC	Body centered Cubic
BM	Balanced Magnetron
CBM	Conduction Band Minimum
CVD	Chemical Vapour Deposition
CRT	Cathode Ray Tube
Cr	Chromium
Cu	copper
Cu_2O	Cuprite
CuO	tenorite
$Cu_{1-x}B_xO_{2-\delta}$	Copper boron oxide
$Cu_{1-x}Cr_xO_{2-\delta}$	Copper chromium oxide
DC	Direct Current
DOS	Density of States
eV	Electron volt

Table B1: ....continued

Abbreviation	**Expansion**
FCC	Face Centered Cubic
GXRD	Glancing Angle X-ray Diffraction
HMC	Heavy Metal Cation
IC	Integrated Circuit
ITO	Indium Tin Oxide
JFET	Junction Filed Effect Transistor
LCD	Liquid Crystal Display
LVDT	Linear Variable Differential Transformer
MOSFET	Metal Oxide Semiconductor Filed Effect Transistor
OLED	Organic Light Emitting Diode
Opp	Oxygen Partial Pressure
OTFT	Organic Thin Film Transistor
PE	Photoelectron
PECVD	Plasma Enhanced Chemical Vapour Deposition
PEN	Poly Ethylene Naphthalate
PET	Poly Ethylene Terephthalate
PLD	Pulsed Laser Deposition
PVD	Physical Vapour Deposition
RF	Radio Frequency
rpm	Rotations Per Minute
RT	Room Temperature
sccm	Standard Cubic Centimeter per minute
SPM	Scanning Probe Microscope
Sn	Tin
SnO	Stannous oxide

Table B1: ....continued

Abbreviation	**Expansion**
SnO_2	Stannic oxide
TAOS	Transparent Amorphous Oxide Semiconductor
TFT	Thin Film Transistor
TSO	Transparent Semiconducting Oxide
TTFT	Transparent Thin Film Transistor
UBM	Unbalanced Magnetron
UV	Ultraviolet
VBM	Valence Band Maximum
XPS	X-ray Photoelectron Spectroscopy
XRD	X-ray Diffraction

Bibliography

[1] K. L. Chopra, S. Major and D. K. Pandya, Thin Solid Films, 102 (1983) 1-46.

[2] A. L. Dawar and J. C. Joshi, J. Mater. Sci., 19 (1984) 1.

[3] H. L. Hartnagel, A. L. Dawar, A. K. Jain and C. Jagadish, Semiconducting Transparent Thin Films, Institute of Physics Publishing, London (1995).

[4] D. S. Ginley and C. Bright (Editors), MRS Bull., 25 (2000).

[5] E. Fortunato, D. Ginley, H. Hosono and D. C. Paine, MRS Bull., 32 (2007) 242.

[6] G. J. Exarhos and X.-D. Zhou, Thin Solid Films, 515 (2007) 7025-7052.

[7] D. J. Griffits, Introduction to Electrodynamics, 3rd Edn, Prentice - Hall of India Pvt. Ltd, New Delhi (2002).

[8] I. Hamberg and C.G. Granqvist, J. Appl. Phys., 60 (1986) 123.

[9] J. Hu and R. G. Gordon, J Appl. Phys. 71 (1992) 880.

[10] I. Hamberg, A. Hjortsberg, and C. G. Granqvist, Appl. Phys. Lett. 40 (1982) 362.

[11] T. J. Coutts, D. L. Young and L. Xiaonan, MRS Bull. 8 (2000) 58.

[12] J. E. Medvedeva, Europhys. Lett., 78 (2007) 4.

[13] T. Minami, MRS Bull., 25 (2000) 38.

[14] T. B. Reed, Free Energy of Formation of Binary Compounds, MIT Press, Cambridge, MA (1971).

[15] J. H. W. de Wit, G. van Unen and M. Lahey, J. Phys. Chem. Solids, 38 (1977) 819.

[16] F. A. Kroger, The Chemistry of Imperfect Crystals, North-Holland, Amsterdam (1974).

[17] S. Lany and A. Zunger, Phys. Rev. Lett., 98 (2007) 501.

[18] D. B. Fraser and H. D. Cook, J. Electrochem. Soc., 119 (1972) 1368.

[19] G. Haacke, Appl. Phys., 47 (1976) 4086.

[20] P. A. Iles and S. I. Soclof, I. E. E. Photovoltaic Specialists Conference (1976) 978.

[21] R. A. Street, Hydrogenated Amorphous Silicon, Cambridge University Press (1991).

[22] J. Singh and K. Shimakawa, Advances in Amorphous Semiconductors, Taylor and Francis Group, London (2003).

[23] N. F. Mott and E. A. Davis, Electronic processes in non-crystalline materials, Clarendon Press, Oxford (1979).

[24] M. H Cohen, H. Fritzsche and S. R Ovshinsky, Phys. Rev. Lett., 22 (1969) 1065.

[25] H. Fritzsche, Electrical and structural properties of amorphous semiconductors, Academic Press, London (1973) 55.

[26] H. Fritzsche, Amorphous and liquid semiconductors. J. Tauc, Plenum Press, New York (1974) 221.

[27] E. A Davis and N. F. Mott, Phil. Mag., 22 (1970) 903.

[28] N. F. Mott, Phil. Mag., 26 (1972) 505.

[29] N. F. Mott Contemp. Phys., 26 (1985) 203.

[30] T. Kasuya, J. Phys. Soc. Jpn., 13 (1958) 1096.

[31] A. Miller and E. Abrahams. Phys. Rev., 120 (1960) 745.

[32] N. F. Mott, Philo. Mag. 19 (1969) 835.

[33] E. A. Davis, J. Appl. Phys., 32 (1993) 178.

[34] D. L. Wood and J. Tauc, Phys. Rev. B, 5 (1972) 3144.

[35] G. D. Cody, B. G. Brooks, and B. Abels, Sol. Energy Mat., 8 (1982) 231.

[36] H. Fritzsche, Sol. Energy Mat., 3 (1980) 447.

[37] F. Demichellis, E. M. Mezzetti, A. Tagliaferro, E. Tresso, P. Rava, and N. M. Ravindra. J. Appl. Phys., 59 (1986) 611.

[38] E. A. Fagen and H. J. Fritzsche. J. Non-Cryst. Solids, 4 (1970) 480.

[39] G. D. Cody in : J. I. Pankove (ed.), Hydrogenated Amorphous Silicon. Academic Press, New York (1984).

[40] K. Badekar, Ann. Phys. (Leipzig) 22 (1907) 749.

[41] G. Rupperecht, Z. Phys. 139 (1954) 504.

[42] C. M. Lampert, Sol. Energy Mater, 6 (1981) 1.

[43] R. G. Gordon, MRS Bull., (August 2000) 52.

[44] B. G. Lewis, D.C. Paine, MRS Bull., (2000) 22.

[45] C. G. Granqvist, A. Azens, A. Hjelm, L. Kullman, G.A. Niklasson, D. Ronnow, M.S. Mattson, M. Veszelei, G. Vaivars, Sol. Energy 63 (1998) 199.

[46] D. R. Kammler, D. D. Edwards, B. J. Ingram, T. O. Mason, G. B. Palmer, A. Ambrosini, K. R. Poeppelmeier, in: V. K. Kapur, R.D. McConnel, D. Carlson, G.P. Ceasan, A. Rohatgi (Eds.), Electrochem. Soc. Proc, Pennington NJ, 99-11 (1999) 68.

[47] S. H. Lee, K. H. Hwang, S. K. Joo, in: K.C. Ho, D.A. McArthur (Eds.), Electrochromic Materials, Second International Symposium, Electrochem. Soc. Proc, Pennington NJ, 94-2 (1994) 290.

[48] P. S. Lugg, S. Bommarito, J. Bailey, K. Budd, P. Cullen, K. Chen, L. C. Hardy, M. Nachbor, in: Solid State Ionic Devices, Electrochem. Soc. Proc., Pennington NJ, 99-13 (1999) 284.

[49] Y. Nakato, K. I. Kai, K. Kawabe, Sol. Energy Mater. Sol. Cells, 37 (1995) 323.

[50] T. T. Emons, J. Li, L. F. Nazar, J. Am. Chem. Soc., 124 (2002) 8517.

[51] M. G. Hutchins, G. D. McMeeking, Biosensor Patent No. 90, 27, 607.2 (1990).

[52] Y. He, J. Kanicki, Appl. Phys. Lett. 76 (2000) 661.

[53] J. F. Wager, Science 300 (2003) 1245.

[54] C. M. Lampert, Sol. Energy Mater, 21 (1990) 191.

[55] R. L. Cornia, J. B. Fenn, H. Memarian, R. Ringer, Proc. of 41st Annual Technical Conference, Boston, SVC (1998) 452.

[56] D. R. Cairns, R. P. Witte, D. K. Sparacin, S. M. Sachsman, D. C. Paine, G. P. Crawford, R. Newton, Appl. Phys.Lett., 76 (2000) 1425.

[57] C. H. Seager, D. C. McIntyre, W. L. Warren, B. A. Tuttle, Appl. Phys. Lett., 68 (1996) 2660.

[58] M. W. J. Prince, K. O. Gross-Holtz, G. Muller, J. B. Cillessen, J. B. Giesbers, R. P. Weening, R. M. Wolf, Appl. Phys. Lett., 68 (1996) 3650.

[59] H. Sato, T. Minami, S. Takata, T. Yamada, Thin Solid Films 236 (1993) 27.

[60] H. Kawazoe, M. Yasukawa, H. Hyodo, M. Kurita, H. Yanagi, H. Hosono, Nature 389 (1997) 939.

[61] H. Ohta, K. Kawamura, N. Sarukura, M. Orita, M. Hirano, and H. Hosono, Appl. Phys. Lett. 77 (2000) 475 .

[62] A. Facchetti and T. J. Marks. Transparent electronics from synthesis to applications.Wiley (2010) 31-57.

[63] A. Zunger, Appl. Phys. Lett., 83 (2003) 57-59 .

[64] S. B. Zhang and J. E. Northrup, Phys. Rev. Lett., 67,(1991) 2339-2342 .

[65] W. Walukiewicz, Physica B, 302 (2001) 123-134 .

[66] S. B. Zhang, S.-H. Wei, A. Zunger, J.Appl.Phys.,83 (1997) 3192-3196.

[67] S. Fraga, S. Karwowski, K. M. S. Saxena, Handbook of Atomic Data, Elsevier, Amsterdam, 1976.

[68] H. Kawazoe, H. Yanagi, K. Ueda, H. Hosono, MRS Bull. (August 2000) 28.

[69] D. DeVault, J. Chem. Educ. 21 (1944) 526.

[70] J. C. Bailar Jr., H. J. Emeleus, Sir N. Ronald, A.F. Trotman-Dickenson (Eds.), Comprehensive Inorganic Chemistry, Pergamon, New York, NY (1973).

[71] Y. K. Leung, A. K. Khan, J. F. Kos, F. P. Koffyberg, Proceedings of National Conference on Solar Energy, Montreal, Solar Energy Society of Canada (1981) 124.

[72] J. P. Dahl, A. C. Switendick, J. Phys. Chem. Solids, 27 (1966) 931.

[73] M. Hayashi, K. Katsuki, J. Phys. Soc. Jpn., 5 (1950) 380.

[74] L. Kleinman, K. Mednick, Phys. Rev. B, 21 (1980) 1549.

[75] H. Yanagi, S. Inoue, K. Ueda, H. Kawazoe, H. Hosono, N. Hamada, J. Appl. Phys., 88 (2000) 4159.

[76] M. Marquardt, N. Ashmore, and D. Cann, Thin Solid Films, 496 (2006) 146-156.

[77] W. Staehlin, H. R. Oswald, Z. Anorgan. Allg. Chem., 373 (1970) 69-72 .

[78] H. Yanagi, S. Inoue, K. Ueda, H. Kawazoe, H. Hiroshi, H. Hosono, N. Hamada, J. Appl. Phys., 88 (2000) 4159-4163.

[79] B. J. Ingram, T. O. Mason, R. Asahi, K. T. Park, A. J. Freeman, Phys. Rev. B, 64 ((2001) 114.

[80] J. Robertson, P.W. Peacock, M. D. Towler, R. Needs, 411 (2002) 96-100.

[81] F.A. Benko, F.P. Koffyberg, J. Phys. Chem. Solids, 45 (1984) 57

[82] K. Ueda, T. Hase, H. Yanagi, H. Kawazoe, H. Hosono, H. Ohta, M. Orita, M. Hirano, J. Appl. Phys., 89 (2001) 1790.

[83] H. Yanagi, T. Hase, S. Ibuki, K. Ueda, H. Hosono, Appl. Phys. Lett., 78 (2001) 1583.

[84] H. Yanagi, K. Ueda, H. Ohta, M. Orita, M. Hirano, H. Hosono, Solid State Commun., 121 (2001) 15.

[85] J. Tate, M. K. Jayaraj, A. D. Draeseke, T. Ulbrich, A. W. Sleight, K. A. Vanaja, R. Nagarajan, J. F. Wager, R. L. Hoffman, Thin Solid Films 411 (2002) 119.

[86] T. Ishiguro, A. Kitazawa, N. Mizutani, M. Kato, J. Solid State Chem., 40 (1981) 170.

[87] C. T. Prewitt, R. D. Shannon, D. B. Rogers, Inorg. Chem., 10 (1971) 719.

[88] B. V. Kohler, M. Jansen, Z. Anorg. Allg. Chem., 543 (1986) 73.

[89] M. Shimode, M. Sasaki, K. Mukaida, J. Solid State Chem., 151 (2000) 16.

[90] J. Robertson, P. W. Peacock, M. D. Towler, R. Needs, Thin Solid Films, 411 (2002) 96.

[91] B. J. Ingram, T. O. Mason, R. Asahi, K. T. Park, A. J. Freeman, Phys. Rev. B, 64 (2001) 155114.

[92] N. Duan, A. W. Sleight, M. K. Jayaraj, J. Tate, Appl. Phys. Lett., 77 (2000) 1325.

[93] R. Nagarajan, A. D. Draeseke, A. W. Sleight, J. Tate, J. Appl. Phys., 89 (2001) 8022.

[94] M. K. Jayaraj, A. D. Draeseke, J. Tate, A. W. Sleight, Thin Solid Films 397 (2001) 244.

[95] L. F. Mattheiss, Phys. Rev. B., 48 (1993) 18300.

[96] O. Crottaz, F. Kubel, H. Schmid, J. Solid State Chem., 122 (1996) 247.

[97] R. Nagarajan, S. Uma, M. K. Jayaraj, J. Tate, A. W. Sleight, Solid State Sci., 4 (2002) 787.

[98] H. Yangi, T. Hase, S. Ibuki, K. Ueda, and H. Hosono, Appl. Phys. Lett., 78 (2001) 1583.

[99] X. Nie, S. H. Wei, and S. B. Zhang, Phys. Rev. Lett. 88 (2002) 066405.

[100] J. Pellicer-Porres, A. Segura, A. S. Gilliland, A. Munoz, P. Rodriguez-Hernandez, D. Kim, M. S. Lee, and T. Y. Kim, Appl. Phys. Lett. 88 (2006) 181904.

[101] Y. Ogo, H. Hiramatsu, K. Nomura, H. Yanagi, T. Kamiya, M. Hirano, and H. Hosono, Appl. Phys. Lett., 93 (2008) 032113.

[102] J. Ni, X. Zhao, X. Zheng, J. Zhao, and B. Liu, Acta Mater., 57 1 (2009) 278-85.

[103] C. W. Ou, Dhananjay, Z. Y. Ho, Y. C. Chuang, S. S. Cheng, M. C. Wu, K. C. Ho, and C. W. Chu, Appl. Phys. Lett., 92 (2008) 122113.

[104] Z. D. Guan, Z. T. Zhang, and J. S. Jiao,Tsinghua University Press, Beijing (1992).

[105] Z. M. Jarzebski, Oxide Semiconductors, p. 150, Pergamon, Oxford (1973).

[106] M. D. Irwin, D. B. Buchholz, A.W. Hains, R. P. H. Chang and T. J. Marks, PNAS, 105 (2008) 2783-2787.

[107] A. Tsukazaki, A. Ohtomo, T. Onuma, M. Ohtani, T. Makino, M. Sumiya, K. Ohtani, S. F. Chichibu, S. Fuke, Y. Segawa, H.

Ohno, H. Koinuma and M. Kawasaki, Nature Mater., 4 (2005) 42-46.

[108] J. J. Lander, J. Phys. Chem. Solids 15 (1960) 324.

[109] Y. Sato and S. Sato, Thin Solid Films 281 (1996) 445.

[110] K. Minegishi, Y. Koiwai, Y. Kikuchi, K. Yano, M. Kasuga and A. Shimizu, Jpn. J. Appl. Phys., 36 (1997) L1453.

[111] X. L. Guo, H. Tabata and T. Kawai, J. Cryst. Growth 233 (2001) 135.

[112] J. Wang, G. Du, B. Zhao, X. Yang, Y. Zhang, Y. Ma, D. Liu, Y. Chang, H. Wang, H. Yang and S. Yang, J. Cryst. Growth, 255 (2003) 293.

[113] D. C. Look, D. C. Reynolds, C. W. Litton, R. L. Jones, D. B. Eason and G. Cantwell, Appl. Phys. Lett., 81 (2002) 1830.

[114] A.B.M.A. Ashrafi, I. Suemune, H. Kumano and S. Tanaka, Jpn. J. Appl. Phys. 41 (2002) L1281.

[115] T. Yamamoto and H. K. Yoshida, Jpn. J. Appl. Phys. 38 (1999) L166.

[116] M. Joseph, H. Tabata and T. Kawai, Jpn. J. Appl. Phys. 38 (1999) L2505.

[117] K. Tamura, T. Makino, A. Tsukazaki, M. Sumiya, S. Fuke, T. Furumochi, M. Lippmaa, C. H. Chia, Y. Segawa, H. Koinuma and M. Kawasaki, Solid State Commun., 127 (2003) 265.

[118] K. Nakahara, H. Takasu, P. Fons, A. Yamada, K. Iwata, K. Matsubara, R. Hunger and S. Niki, Appl. Phys. Lett., 79 (2001) 4139.

[119] A. Tsukazaki, H. Saito, K. Tamura, M. Ohtani, H. Koinuma, M. Sumiya, S. Fuke, T. Fukumura and M. Kawasaki, Appl. Phys. Lett. 81 (2002) 235.

[120] B. J. Ingram, M. I. Bertoni, K. R. Poeppelmeier and T. O. Mason, Thin Solid Films, 486 (2005) 86-93.

[121] J. E. Lilienfield , U.S. Patent (1930) 1745175.

[122] J. E. Lilienfield , U.S. Patent (1932) 1877140.

[123] J. E. Lilienfi eld , U.S. Patent (1933) 1900018.

[124] O. Heil, U. K. Patent 439457 (1935).

[125] P. K. Weimer, Proceedings of the Institute of Radio Engineers, 50 (1962) 1462. (1979) 47 .

[126] P. K. Weimer, presented at IRE-AICE Device Res. Conf., Stanford, CA (1961).

[127] H. A. Klasens and H. Koelmans, Solid-State Electron, 7 (1964) 701.

[128] A. C. Tickle, Thin-Film Transistors - A New Approach to Microelectronics, Wiley, New York (1969).

[129] G. F. Boesen and J. E. Jacobs, Proceedings of the Institute of Electrical and Electronics Engineers, 56 (1968) 2094 .

[130] A. Aoki and H. Sasakura, Jpn. J. Appl. Phys., 9 (1970) 582 .

[131] W. E. Spear and P. G. Le Comber: Solid State Commun. 17 (1975) 1193.

[132] P. G. Le Comber, W. E. Spear, and A. Ghaith: Electron. Lett. 15 (1979) 179.

[133] A. J. Snell, K. D. Mackenzie, W. E Spear, P. G. Le Comber and A. J. Hughes: Appl. Phys., 24 (1981) 357.

[134] M. W. J. Prins, K. O. GrosseHolz, G. Muller, J. F. M. Cillessen, J. B. Giesbers, R. P. Weening and R. M. Wolf , Appl. Phys. Lett., 68 (1996) 3650.

[135] R. L. Hoffman, B. J. Norris and J. F. Wager, Appl. Phys. Lett., 82 (2003) 733.

[136] P. F. Carcia, R. S. McLean, M. H. Reilly and G. Nunes, Appl. Phys. Lett., 82 (2003) 1117.

[137] E. M. C. Fortunato, P. M. C. Barquinha, A. Pimentel, A. M. F. Goncalves, A. J. S. Marques, L. M. N. Pereira and R. F. P. Martins, Adv. Mater., 17 (2005) 590.

[138] S. Masuda, K. Kitamura, Y. Okumura, S. Miyatake, H. Tabata and T. Kawai, J. Appl. Phys., 93 (2003) 1624 .

[139] J. Nishii, F. M. Hossain, S. Takagi, T. Aita, K. Saikusa, Y. Ohmaki, I. Ohkubo, S. Kishimoto, A. Ohtomo, T. Fukumura, F. Matsukura, Y. Ohno, H. Koinuma, H. Ohno and M. Kawasaki, Jpn. J. Appl. Phys., 42 (2003) L347 .

[140] E. Fortunato, P. Barquinha, A. Pimentel, A. Goncalves, A. Marques, R. Martins and L. Pereira, Appl. Phys. Lett., 85 (2004) 2541.

[141] E. Fortunato, P. Barquinha, A. Pimentel, A. Goncalves, A. Marques, L. Pereira and R. Martins, presented at NATO Advanced Research Work shop on Zinc Oxide as a Material for Micro- and Optoelectronic Applications, St Petersburg, RUSSIA, Jun 23-25 (2004).

[142] B. J. Norris, J. Anderson, J. F. Wager and D. A. Keszler, J. Appl. Phys. D, 36 (2003) L105.

[143] R. E. Presley, C. L. Munsee, C. H. Park, D. Hong, J. F. Wager and D. A. Keszler, J. Phys. D-Appl. Phys., 37 (2004) 2810. 200 (1996) 165 .

[144] E. Fortunato, P. Barquinha, A. Pimentel, A. Goncalves, A. Marques, L. Pereira and R. Martins, Adv. Mater., 17 (2005) 590 .

[145] D. Zhang, C. Li, S. Han, X. Liu, T. Tang, W. Jin and C. Zhou, Appl. Phys. Lett., 82 (2003) 112.

[146] Y. W. Heo, L. C. Tien, Y. Kwon, D. P. Norton, S. J. Pearton, B. S. Kang and F. Ren, Appl. Phys. Lett., 85 (2004) 2274.

[147] Z. Fan, D. Wang, P. C. Chang, W. Y. Tseng and J. G. Lu, Appl. Phys. Lett., 85 (2004) 5923.

[148] K. Nomura, H. Ohta, K. Ueda, T. Kamiya, M. Hirano and H. Hosono, Science, 300 (2003) 1269.

[149] H. Hosono, N. Kikuchi, N. Ueda and H. Kawazoe, J. Non-Cryst. Solids, 200 (1996) 165.

[150] N. L. Dehuff, E. S. Kettenring, D. Hong, H. Q. Chiang, J. F. Wager, R. L. Hoffman, C. H. Park and D. A. Keszler, J. Appl. Phys., 97 (2005).

[151] P. Barquinha, A. Pimentel, A. Marques, L. Pereira, R. Martins and E. Fortunato, J. Non-Cryst. Solids, 352 (2006) 1749.

[152] B. Yaglioglu, H. Y. Yeom, R. Beresford and D. C. Paine, Appl. Phys. Lett., 89 (2006) 062103.

[153] D. C. Paine, B. Yaglioglu, Z. Beiley and S. Lee, Thin Solid Films, 516 (2008) 5894.

[154] P. Barquinha, L. Pereira, G. Goncalves, R. Martins and E. Fortunato, J.Electrochem. Soc., 156 (2009) H161.

[155] A. Suresh, P. Wellenius, A. Dhawan and J. Muth, Appl. Phys. Lett., 90 (2007) 123512.

[156] J. S. Park, J. K. Jeong, Y. G. Mo, H. D. Kim and S. I. Kim, Appl. Phys. Lett., 90 (2007) 2106.

[157] D. Kang, I. Song, C. Kim, Y. Park, T. D. Kang, H. S. Lee, J. W. Park, S. H. Baek, S. H. Choi and H. Lee, Appl. Phys. Lett., 91 (2007) 091910.

[158] H. Hosono, K. Nomura, Y. Ogo, T. Uruga and T. Kamiya, J Non-Cryst Solids, 354 (2008) 2796.

[159] T. Iwasaki, N. Itagaki, T. Den, H. Kumomi, K. Nomura, T. Kamiy and H. Hosono, Appl. Phys. Lett., 90 (2007) 2114.

[160] C. D. Dimitrakopoulos and P. R. L. Malenfant, Adv. Mater, 14 (2002) 99.

[161] A. Facchetti, M. H. Yoon and T. J. Marks, Adv. Mater., 17 (2005) 1705.

[162] H. Sirringhaus, Adv. Mater., 17 (2005)2411.

[163] H. Klauk, Chem. Soc. Rev., 39 (2010) 2643.

[164] J. M. Shaw and P. F. Seidler, IBM J. Res. Development, 45 (2001) 3.

[165] S. R. Forrest and M. E. Thompson, Chem. Rev., 107 (2007) 923.

[166] M. R. Wasielewski and S. R. Marder, Adv. Mater., 23 (2011) 268.

[167] R. Schmidt, J. H. Oh, Y. S. Sun, M. Deppisch, A. M. Krause, K. Radacki, H. Braunschweig, M. Konemann, P. Erk, Z. A. Bao and F. Wurthner, J. Am. Chem. Soc., 131 (2009) 6215.

[168] H. Usta, A. Facchetti and T. J. Marks, J. Am. Chem. Soc., 130 (2008) 8580.

[169] S. Handa, E. Miyazaki, K. Takimiya and Y. Kunugi, J. Am. Chem. Soc., 129 (2007) 11684.

[170] R. E. Presley, D. Hong, H. Q. Chiang, C. M. Hung, R. L. Hoffman and J. F. Wager, Solid State Electron., 50 (2006) 500.

[171] K. Wasa, M. Kitabatake, and H. Adachi. Thin Film Materials Tech- nology. Springer-Verlag GmbH and Co. KG, Germany (2004).

[172] L. I. Maissel and R. Glang (Eds), Handbook of Thin Film Technology. McGraw-Hill, New York, (1970).

[173] M. Ohring. Materials Science of Thin Films, Deposition and Structure. Academic Press, New York (2001).

[174] G. S. Anderson, W. N. Mayer, G. K. Wehner, J. Appl. Phys., 33 (1962) 2291.

[175] P. D. Davidse, L. I. Maissel, J. Appl. Phys., 37 (1966) 754.

[176] K. Wasa and S. Hayakawa, Rev. Sci. Instrum., 40 (1969) 693.

[177] L. Holland, Vacuum Deposition Thin films, John Wiley and Sons Inc., New York (1956).

[178] Veeco Dektak 6M stylus profiller, Manual (2004).

[179] P. Dutta. Current Science, 78 (2000) 1478.

[180] T. Nagase, T. Ooie, Y. Nakatsuka, K. Shinozaki and N. Mizutani, Jpn. J. Appl. Phys 39 (2000) L713.

[181] K. Iwata, P. Fons, S. Niki, A. Yamada, K. Matsubara, K. Nakahara and H. Takasu, Phys. Stat. Sol. A, 180 (2000) 287.

[182] D. K. Schroder, Semiconductor material and device characterization, A Wiley-intersciernce publication (1998).

[183] A. Tanaka, S. Onari and T. Arai, Phys. Rev. B, 47 (1993) 1237.

[184] A. Tanaka, S. Onari and T. Arai, Phys. Rev. B, 45 (1992) 6587.

[185] M. Rajalakshmi, T. Sakunthala and A. K. Arora, J. Phys.: Condens. Matter., 9 (1997) 9745.

[186] H. Klauk, Chem. Soc. Rev., 39 (2010) 2643.

[187] C. R. Kagan and P. Andry, Thin Film Transistors. Marcel Dekker, New York (2003).

[188] T. Eguchi, S. Ochikoshi and T. Nanao, Jpn. Kokai Tokkyo Koho, 9 (1986). and K. R. Poeppelmeier, edited by V.K. Kapur, R .D. McConnel, D. Carlson, G. P. Ceasar and A. Rohatgi, The Electrochemical Society Pennington,NJ Proc. (1999) 99.

[189] E. Fortunato, R. Martins and P. Barquinha, Adv. Mater, 24 (2012) 2945.

[190] J. Pannetier, G. Denes, Acta Crystallogr., Sect. B: Struct. Crystallogr. Cryst. Chem., 36 (1980) 2763.

[191] G. W. Watson J. Chem. Phys., 114 (2001) 758.

[192] J. Terra, D. Guenzburger, Phys. Rev. B, 44 (1991) 8584.

[193] M. Meyer, G. Onida, M. Palummo and L. Reining, Phys. Rev. B, 64 (2001) 045119.

[194] J. Galy, G. Meunier and S. Andersson, J. Solid State Chem. 13 (1975) 142.

[195] T. Kamiya and H. Hosono, NPG Asia Mater., 2 (2010) 15.

[196] I. Lefebvre, M. A. Szymanski, J. Olivier-Fourcade and J. C. Jumas, Phys. Rev. B, 58 (1998) 1896.

[197] A. Togo, F. Oba, and I. Tanaka Phys. Rev. B, 74 (2006) 195128.

[198] P. Barquinha, R. Martinos, L. pereira and E. Fortunato, Wiley (2012) 72.

[199] S. Hwang, Y. Y. Kim, J. H. Lee, D. K. Seo, J.Y. Lee, and H. K. Cho J. Am. Ceram. Soc. (2011) 1.

[200] A. K. Sinha, P. K. Manna, M. Pradhan, C. Mondal, S. M. Yusuf and T. Pal Royal. Soc.Chem. Adv., 4 (2014) 208.

[201] T. Seiyama, A. Kato, K. Fujiishi, and M. Nagatani, Anal. Chem., 34, (1962) 1502.

[202] W. Gopel and K. D. Schierbaum, Sens. Actuators B, 26 (1995) 1

[203] N. Yamazoe, Sens. Actuators B, 5 (1991) 7.

[204] L. Hozer, translation editor D. Holland, PWN-Polish Scientific Publishers, Warsaw (1994).

[205] C. O. Park and S. A. Akbar, J. Mater. Sci., 38 (2003) 4611.

[206] K. Galatsis, L. Cukrov, W. Wlodarski, P. McCormick, K. Kalantar-zadeh, E. Comini and G. Sberveglieri, Sensors and Actuators B, 93 (2003) 562.

[207] C. W. Ou, Z. Y. Ho, Y. C. Chuang, S. S. Cheng, M. C. Wu, K. C. Ho, C. W. Chu, Appl. Phys. Lett., 92 (2008) 2113.

[208] Dhananjay, C. W. Chu, C. W. Ou, M. C. Wu, Z. Y. Ho, K. C. Ho, S. W. Lee, Appl. Phys. Lett., 92,(2008) 2103.

[209] H. N. Lee, H. J. Kim, C. K. Kim, Jpn. J. Appl. Phys., 49 (2010) 0202.

[210] H. Yabuta, N. Kaji, R. Hayashi, H. Kumomi, K. Nomura, T. Kamiya, M. Hirano and H. Hosono, Appl. Phys. Lett., 97 (2010) 72111.

[211] L. Y. Liang, Z. M. Liu, H. T. Cao, Z. Yu, Y. Y. Shi, A. H. Chen, H. Z. Zhang, Y. Q. Fang and X. L. Sun, J. Electrochem. Soc., 157 (2010) H598.

[212] E. Fortunato, R. Barros, P. Barquinha, V. Figueiredo, S. H. K. Park, C. S. Hwang and R. Martins, Appl. Phys. Lett., 97 (2010) 2105. M. Hirano and H. Hosono, Appl. Phys. Lett., 97 (2010) 2111.

[213] E. Fortunato and R. Martins, Phys. Status Solidi - Rapid Res. Lett., 5 (2011) 336.

[214] K. Nomura, T. Kamiya and H. Hosono, Adv. Mater., 23, (2011) 3431.

[215] R. Martins, V. Figueiredo, R. Barros, P. Barquinha, G. Gonalves, L. Pereira, I. Ferreira, E. Fortunato, Proc. SPIE 8263, Oxide-based Materials and Devices III (2012) 826315.

[216] A. Jesus. F. Caraveo, P.K. Nayak, A. Hala. A. Jawhari, B. Danilo. Granato, U. Schwingenschlogl and H. N. Alshareef, ACSNano 7 (2013) 5160.

[217] Y. Caglar, S. Ilican, M. Caglar, F. Yakuphanoglu, J. Wu, K. Gao et al. J. Alloys. Compd, 481 (2009) 885.

[218] J.Sengupta, R. K. Sahoo, K. K. Bardhan and C. D. Mukherjee, material letters, 65 (2011) 2572.

[219] J. Szuber, G. Czempika, R. Larcipreteb, D Kozieja and B. Adamowicza Thin Solid Films, 391 (2001) 198.

[220] M. Kwokaa, L. Ottavianob, M. Passacantandob, S. Santuccib, G. Czempika and J. Szubera Thin Solid Films, 490 (2005) 36.

[221] J. Themlin, M. Chtaib, L. Henrard, P. Lambin,J. Darville and J-M. Gilles, Phys. Rev. B, 46 (1992) 2460.

[222] J. Geurts, S. Rau, W. Richter and F. J. Schmitte, Thin Solid Films, 121 (1984) 217.

[223] J. F. Scott, J. Chem. Phys., 53 (1970) 852.

[224] R. Swanepoel, J. Phys. E, 16 (1983) 1214.

[225] C. X. Wang, G. W. Yang, H. W. Liu, Y. H. Han, J. F Luo, C. X. Gao and G. T, Zou Appl. Phys. Lett., 84 (2004) 2427.

[226] K. A. Vanaja, U. M. Bhatta, R. S. Ajimsha, S. Jayalekshmi and M. K. Jayaraj, Bull. Mater. Sci., 31 (2008) 753.

[227] R. S. Ajimsha, M. K. Jayaraj and L. M. Kukreja, Journal of Electronic Materials, 37 (2008) 770.

[228] R. S. Ajimsha, K. A. Vanaja, M. K. Jayaraj, P. Misra, V. K. Dixit and L. M. Kukreja, Thin Solid Films 515 (2007) 7352.

[229] R. L. Hoffman, J. F. Wager, M. K. Jayaraj and J.Tate, J. Appl. Phys. 90 (2001) 5763.

[230] E. H. Kennard and E. O. Dieterich, Physical Review, 9 (1917).

[231] E. Fortunato and R. Martins, Phys. Stat. Solid., 5 (2011) 336.

[232] E. Fortunato, P. Barquinha, L. Pereira and R. Martins, Transparent Electronics: From Materials to Devices. Hoboken, NJ, USA: Wiley (2012).

[233] J. Li, G. Vizkelethy, P. Revesz, J. W. Mayer, and K. N. Tu J. Appl. Phys., 69 (1991) 1020.

[234] Y. Ohya, S. Ito, T. Ban and Y. Takahashi, Key Engineering Materials, 113 (2000) 181.

[235] Lanke, UD and Vedawyas, M Nuclear Instruments and Methods in Physics Research B, 155 (1999) 97-101.

[236] M. Nolan and S. D. Elliott, Phys. Chemistry, 8 (2006) 5350.

[237] H. Raebiger, S. Lany, and A. Zunger, Phys. Rev. B, (2007) 76.

[238] M. A. Rafea, N. Roushdy, J. Phys. D-Appl. Phys., 42 (2009) 6.

[239] M. Izaki, M. Nagai, K. Maeda, F. B. Mohamad, K. Motomura, J. Sasano, T. Shinagawa, and S. Watase, J. Electrochem. Soc., 158 (2011) D578.

[240] L. Armelao, D. Barreca, M. Bertapelle, G. Bottaro, C. Sada, and E. Tondello, Thin Solid Films, 442 (2003) 4852.

[241] V. F. Drobny and D. L. Pulfrey, Thin Solid Films, 61 (1979) 89.

[242] A. Chen, H. Long, X. Li, Y. Li, G. Yang, and P. Lu, Vacuum, 83 (2009) 927.

[243] D. Barreca, E. Comini, A. Gasparotto, C. Maccato, C. Sada, G. Sberveglieri, and E. Tondello, Sens. Actuators B, 141 (2009) 270.

[244] G. Beensh-Marchwicka, L. Krol-Stepniewska, and M. Slaby, Thin Solid Films, 88 (1982) 33 .

[245] W. Klein, H. Schmitt, and M. Boffgen, Thin Solid Films, 191 (1990) 247.

[246] J. W. Han and M. Meyyappan Appl. Phys. Lett., 98 (2011) 192102.

[247] K. Matsuzaki, K. Nomura, H. Yanagi, T. Kamiya, M. Hirano, and H. Hosono, Appl. Phys. Lett., 93 (2008) 202107 .

[248] S. Y. Sung, S. Y. Kim, K. M. Jo, J. H. Lee and J. J. Kim, Appl. Phys. Lett., 97 (2010) 222109 .

[249] X. Zou, G. Fang, L. Yuan, M. Li, W. Guan, and X. Zhao, IEEE Electron Device Lett., 31 (2010) 827.

[250] E. Fortunato, V. Figueiredo, P. Barquinha, E. Elamurugu, R. Barros, G. Gonalves, S.-H. K. Park, C. S. Hwang, and R. Martins, Appl. Phys. Lett., 96 (2010) 192102.

[251] X. Zou, G. Fang, J. Wan, X. He, H. Wang, N. Liu, H. Long, and X. Zhao, IEEE Trans. Electron Dev., 58 (2011) 2003.

[252] Z. Q. Yao, S. L. Liu, L. Zhang, B. He, A. Kumar, X. Jiang, W. J. Zhang and G. Shao Appl. Phys. Lett., 101 (2012) 042114.

[253] D. W. Nam, I. T. Cho, J. H. Lee, E. S. Cho, J. Sohn, S. H. Song and H. I. Kwon J. Vac. Sci. Technol. B, 30 (2012).

[254] S. Y. Kim, C. H. Ahn, J. H. Lee, Y. H. Kwon, S. Hwang, J. Y. Lee and H. K. Cho. ACS Appl. Mater. Interfaces, 5 (2013) 2417.

[255] J. Sohn, S. H. Song, D. W. Nam, I. T. Cho, E. S. Cho, J. H. Lee and H. I. Kwon, Semicond. Sci. Technol., 28 (2013) 015005.

[256] P. Pattanasattayavong, S. Thomas, G. Adamopoulos, M. A. McLachlan and T. D. Anthopoulos, Appl. Phys. Lett., 102 (2013) 163505.

[257] C. Y. Jeong, J. Sohn, S. Hun Song, I. T. Cho, J. H. Lee,E. S. Cho, and H. I. Kwon, Appl. Phys. Lett., 102 (2013) 082103.

[258] K. C. Sanal and M. K. Jayaraj, Room temperature deposited transparent p-channel CuO thin film transistors (Accepted in Appl. Surf. Sci., January, 2014).

[259] K. C. Sanal and M. K. Jayaraj, Fabrication of room temperature deposited p-channel copper oxide thin film transistors (under review).

[260] S. Berg, T. Nyberg, H.-O. Blom, and C. Nender, Handbook of Thin Film Process Technology, Institute of Physics Publishing, Bristol, UK (1998).

[261] T. Nyberg, S. Berg, U. Helmersson, and K. Hartig, Appl. Phys. Lett., 86 (2005) 164106.

[262] P.S. Nayar, J. Appl. Phys., 53,(1982) 1069.

[263] Z. Guo, D.X. Zhao, Y.C. Liu, D.Z. Shen, J. Y. Zhang, and B. H. Li, Appl. Phys. Lett., 93 (2008) 163501.

[264] F. P. Koffyberg and F.A. Benko, J. Appl. Phys., 53 (1982) 1173.

[265] M.T.S. Nair, L. Guerrero, O.L. Arenas, and P.K. Nair, Appl. Surf. Sci., 150 (1999) 143.

[266] H. Long, G. J. Fan, H. H. Huang, X. M. Mo, W. Xia, B. Z. Dong, X. Q. Meng, X. Z. Zhao, Appl. Phys. Lett., 95 (2009) 013509.

[267] J. Ghijsen, L. H. Tjeng, J. van Elp, and H. Eskes, Phys. Rev. B, 38 (1988) 11322.

[268] V. Figueiredo, E. Elangovan, G. Goncalves, P. Barquinha, L. Pereira, N. Franco, E. Alves, R. Martins, E. Fortunato Appli. Surf Scie. 254 (2008) 3949.

[269] J. F. Wager, Journal of the SID 18/10 (2010) 749.

[270] D. K. Zhang, Y. C. Liu, Y. L. Liu and H. Yang, Physica B, 351 (2004) 178.

[271] P. Lv, W. Zheng, L. Lin, F. Peng, Z. Huang,F. Lai Physica B ,406 (2011) 1253.

[272] A. Parretta, M. K. Jayaraj, A. Di. Nocera, S. Loreti, L. Quercia, A. Agati
physica status solidi, 155 (2006) 399.

[273] H. Kawazoe, M. Yasukawa, H. Hyodo, M. Kurita, H. Yanagi, and H. Hosono, Nature (London) 389 (1997) 939.

[274] A. Kudo, H. Yanagi, K. Ueda, H. Hosono, and H. Kawazoe, Appl. Phys. Lett., 73 (1998) 220.

[275] M. Snure, A. Tiwari, Appl. Phys. Lett., 91 (2007) 092123.

[276] S. Santra, N. S. Das, K. K. Chattopadhyay, Proc. SPIE, (2012) 85491W.

[277] T. Okuda, T. Onoe, Y. Beppu, N. Terada, T. Doi, S. Miyasaka and Y. Tokura, J. Magn. Magn. Mater., 310 (2007) 890.

[278] A.N. Banerjee and K. k. Chattopadhyay, Progress in crystal growth and characterisation of materials, 50 (2006) 52.

[279] S. Luo, K. F. Wang, S. Z. Li, X. W. Dong, Z. B. Yan, H. L. Cai and J. Liu, Appl. Phys. Lett., 94 (2009) 172504.

[280] S. Luo, L. Li, K. F. Wang, S. Z. Li, X. W. Dong, Z. B. Yan and J. Liu, Thin Solid Films, 518 (2010) 50.

[281] K. Hayashi, K. Sato, T. Nozaki and T. Kajitani, Jpn. J. Appl. Phys., 47 (2008) 59.

[282] R. Bywalez, S. Gotzendorfer and P. Lobmann, J. Mater. Chem., 20 (2010) 6562.

[283] T. Okuda, N. Jufuku, S. Hidaka and T.N., Phys. Rev. B, 72 (2005) 144403.

[284] T. Okuda, Y. Beppu, T. Onoe, N. Terada and S. Miyasaka, Phys Rev. B, 77 (2005) 134423.

[285] Y. Ono, K. Satoh, T. Nozaki and T. Kajitani, Jpn. J. Appl. Phys., 46 (2007) 1071.

[286] D. Li, X. D. Fang, Z. H. Deng, S. Zhou, R. H. Tao, W. W. Dong, T. Wang, Y. P. Zhao, G. Meng, and X. B. Zhu, J. Phys. D-Appl. Phys. 40 (2007) 4910.

[287] P. W. Sadik, M. Ivill, V. Craciun, and D. P. Norton, Thin Solid Films, 517 (2009) 3211.

[288] S. Y. Kim, S. Y. Sung, K. M. Jo, J. H. Lee, J. J. Kim, S. J. Pearton, D. P. Norton, and Y. W. Heo, J. Crystal Growth, 326 (2011) 9.

[289] D. Li, X. D. Fang, A. W. Zhao, Z. H. Deng, W. W. Dong, and R. H. Tao, Vacuum, 84 (2010) 851.

[290] S. Mahapatra and S. A. Shivashankar, Chem. Vap. Deposition, 9 (2003) 238.

[291] Y. F. Wang, Y. J. Gu, T. Wang, and W. Z. Shi, J. Alloys Compd., 509 (2011) 5897.

[292] Y. F. Wang, Y. J. Gu, T. Wang, and W. Z. Shi, J. Sol-Gel Sci. Technol., 59 (2011) 222.

[293] D. Shin, J. S. Foord, R. G. Egdell and A.Walsh, J. Appl. Phys., 112 (2012) 113718.

[294] T. W. Chiu, K. Tonooka and N. Kikuchi, Thin Solid Films, 516 (2008) 5941.

[295] T. W. Chiu, K. Tonooka and N. Kikuchi, Vacuum, 83 (2009) 614.

[296] M. Han, K. Jiang, J. Zhang, W. Yu, Y. Li, Z. Hu and J. Chu, J. Mater. Chem., 22 (2012) 18463.

[297] K. Kimura, H. Nakamura, S. Kimura, M. Hagiwara and T. Kumura, Phys. Rev. Lett., 103 (2009) 107201.

[298] M. Soda, K. Kimura, T. Kimura, M. Matsuura and H. K., J. Phys. Soc. Jpn., 78 (2009) 124703.

[299] K. Kimura, T. Otani, H. Nakamura, Y. Wakabayashi and T. Kimura, J. Phys. Soc. Jpn., 78 (2009) 113710.

[300] O. S. Yamaguchi, H. S. Kimura, M. Hagiwara, K. Kimura, T. Kimura, T. Okuda and K. Kindo, Phys. Rev. B, 81 (2010) 033104.

[301] H. Yamaguchi, S. Otomo, S. Kimura, M. Hagiwara, K. Kimura, T. Kimura and K. Kindo, J. Low Temp. Phys., 159 (2010) 130.

[302] T. Okuda, Y. Beppu, Y. Fujii, T. Kishimoto, K. Uto, T. Onoe, N. Jufuku, S. Hidaka, N. Terada and S. Miyasaka, J. Phys. Conf. Ser., 150 (2009) 042157.

[303] R. Rao, A. Dandekar, R. T. K. Baker and M. A. Vannice, J. Catal., 171 (1997) 406.

[304] S. Zhou, X. Fang, Z. Deng, D. Li, W. Dong, R. Tao, G. Meng and T. Wang, Sens. Actuators, B, 143 (2009) 119.

[305] Z. Deng, X. Fang, D. Li, S. Zhou, R. Tao, W. Dong, T. Wang, G. Meng and X. Zhu, J. Alloys Compd., 484 (2009) 619.

[306] T. W. Chiu, Y. C. Yang, A. C. Yeh, Y. P. Wang and Y. W. Feng Vacuum, 87 (2013) 174.

[307] M. O. Sullivan, P. Stamenov, J. Alaria, M. Venkatesan and J .M. D. Coey, IOP publishing, J. Phys: Conference Series, 200 (2010) 052021.

[308] C. D. Wagner, W. M. Riggs, L. E. Davis, J. F. Moulder, G.E. Muilenberg (Eds.), Handbook of X-Ray Photoelectron Spectroscopy, first ed., Perkin-Elmer Corporation (Physical Electronics), Eden Prairie, Minnesota (1979).

[309] T. F. T. Cerqueira, R. S. Perez, F. Trani, M. Amsler, S. Goedecker, M. A.L. Marques, S. Botti, MRS Communications, 3 (2013) 157.

[310] D. Scanlon, A. Walsh, and G. W. Watson, Thin Solid Films, 15 (2009) 4568.

[311] X. Nie, S. H. Wei, and S. B. Zhang, Phys. Rev. Lett. 88 (2002) 066405.

[312] J. Pellicer-Porres, A. Segura, A. S. Gilliland, A. Munoz, P. Rodriguez- Hernandez, D. Kim, M. S. Lee, and T. Y. Kim, Appl. Phys. Lett., 88 (2006) 181904.

[313] C. X. Wang, G. W. Yang, H. W. Liu, Y. H. Han, J. F Luo, C. X. Gao and G. T. Zou, Appl. Phys. Lett., 84 (2004) 2427.

[314] K. C. Sanal and M. K. Jayaraj, Mater. Sci. Eng. B, 13352 (2013) 1.